

DOPING OF ORGANIC SEMICONDUCTORS: EFFECTS OF CROSSLINKING AND DOPANT SUBSTITUENTS

A Dissertation
Presented to
The Academic Faculty

by

Farzaneh Saeedifard

In Partial Fulfillment
of the Requirements for the Degree
Doctor of Philosophy in Chemistry in the
School of Chemistry and Biochemistry

Georgia Institute of Technology
December 2021

COPYRIGHT © 2021 BY FARZANEH SAEEDIFARD

DOPING OF ORGANIC SEMICONDUCTORS: EFFECTS OF CROSSLINKING AND DOPANT SUBSTITUENTS

Approved by:

Dr. Seth Marder, Advisor
School of Chemistry and Biochemistry
Georgia Institute of Technology

Dr. Stefan France
School of Chemistry and Biochemistry
Georgia Institute of Technology

Dr. M. G. Finn
School of Chemistry and Biochemistry
Georgia Institute of Technology

Dr. Shannon Yee
School of Mechanical Engineering
Georgia Institute of Technology

Dr. John R. Reynolds
School of Chemistry and Biochemistry
Georgia Institute of Technology

Date Approved: [October 19, 2021]

ACKNOWLEDGEMENTS

I would like to express my deepest gratitude to my advisor Professor Seth Marder, for his supervision, constant encouragements, and financial support throughout my Ph.D. studies.

I would like to sincerely thank Dr. Stephen Barlow, to whom I am deeply indebted. This thesis would have not been the same without his constructive comments and guidance. His immense knowledge, passion, and patience encourage me to become a better scientist. My thanks also extend to key members of our research group, including Dr. Timothy Parker, Dr. Raghunath Dasari, Dr. Yadong Zhang, and Dr. Junxiang Zhang.

I would like to thank Dr. John Reynolds, Dr. M.G Finn, Dr. Stephan France, and Dr. Shannon Yee for serving on my thesis committee, reviewing this thesis, and providing feedback.

This thesis is the product of multiple fruitful collaborations and I wish to thank the collaborators who have helped me along the way including the Koch group (Humboldt-Universität zu Berlin), the Jurchescu group (Wake Forest University), the Pei group (Peking University), the Kahn group (Princeton University), and the Toney group (Colorado/Stanford University).

I would like to extend my appreciation to Dr. Leslie Gelbaum, Dr. Johannes Leisen, Dr. Robert Braga, Dr. Denise Bale, and Jenny Eaton for their continuous technical support.

Finally, I would like to acknowledge the constant encouragement, support, and love of my family, throughout this journey.

To my family.

TABLE OF CONTENTS

ACKNOWLEDGEMENTS	iii
LIST OF TABLES	viii
LIST OF FIGURES	ixx
LIST OF SYMBOLS AND ABBREVIATIONS	xiii
SUMMARY	xv
CHAPTER 1: Introduction	1
1.1 Organic Electronics	1
1.2 Terminology and Definitions (Conductivity, Mobility, and Charge Injection Efficiency)	3
1.3 Mechanism of Molecular Doping of Organic Semiconductors	8
1.4 Classes of Dopants	12
1.4.1 p-Dopants	12
1.4.2 n-Dopants	13
1.5 Why Is Diffusion of Dopants in Solid State Important?	16
1.5.1 Literature review on diffusion of dopants in OSCs	18
1.5.2 Different strategies reported in the literature to suppress the diffusion of dopants in solid state	20
1.6 Thesis Structure and Overview	25
CHAPTER 2: Immobilization via electrostatic interactions: an approach to decrease the diffusion rate of n-type dopants	27
2.1 Introduction	28
2.2 Synthesis of Tetrakis-DMBI-H	30
2.2.1 Mechanistic studies of tetrakis-DMBI-H and PCBM	31
2.3 Synthesis of tetrakis-O-DMBI-H	33
2.3.1 Kinetic studies of tetrakis-O-DMBI-H	34
2.3.2 Film retention and electrical conductivity studies on tetrakis-O-DMBI-H-doped PCBM	36
2.4 Film Retention and Electrical Conductivity Studies on Polymer Doped with Tetrakis-O-DMBI-H	38
2.4.1 Film retention and electrical conductivity studies on TBDOPV-T-doped tetrakis-O-DMBI-H	39
2.4.2 Ultraviolet photoelectron spectroscopy (UPS)	41
2.5 Diffusion Studies on Tetrakis-O-DMBI-H-doped TBDOPV-T Films	42
2.5.1 Grazing-incidence wide-angle X-ray scattering (GIWAXS)	44
2.6 Summary and Conclusion	47
2.7 Experimental Details	48
2.7.1 Synthesis	48
2.7.2 Characterizations: general procedures and experimental details	51

CHAPTER 3: Immobilization via chemical bond formation: an approach to restrict the diffusion rate of n-type dopants	54
3.1 Introduction	55
3.2 Design and Synthesis of the Thermo-crosslinkable DMBI-H	57
3.2.1 Synthesis of the cation	57
3.2.2 Thermal stability experiments of 2-(4-(bicyclo[4.2.0]octa-1,3,5-trien-7-yloxy)phenyl)-1,3-dimethyl-1H-3l4-benzo[d]imidazole (compound 3.4)	58
3.3 Synthesis of Low-temperature Thermo-crosslinkable DMBI-H	61
3.4 Synthesis and Characterization of the Thermo-crosslinkable BBCBPCB	62
3.4.1 Differential scanning calorimetry (DSC)	62
3.4.2 UV-vis spectra analysis	63
3.5 Doping Products	65
3.5.1 Characterization of the reaction product(s) by MALDI-TOF-MS	65
3.5.2 Characterization of the reaction product by electron paramagnetic resonance (EPR)	67
3.6 Synthesis of BBCB-N-DMBI-H as a Stronger Hydride Donor Derivative	68
3.6.1 Characterization of the doping products by EPR and MALDI-TOF-MS	69
3.7 Diffusion Studies on BBCB-NDMBI-H-doped BBCBPCB Films	71
3.8 Summary and Conclusion	73
3.9 Experimental Details	74
3.9.1 Synthesis	74
3.9.2 Selected ¹ HNMR and ¹³ CNMR spectra	82
3.9.3 Characterizations: general procedures and experimental details	89
CHAPTER 4: investigation of the effect of a polar side chain on the doping behavior of A DMBI-H derivative	90
4.1 Introduction	91
4.2 Synthesis of Dopants	93
4.2.1 Characterization of doped N2200 using MeO-DMBI-H or TEG-DMBI-H using UV-vis-NIR	95
4.2.2 Characterization of doped N2200 using MeO-DMBI-H or TEG-DMBI-H using electrical conductivity measurements.	96
4.2.3 Characterization of doped N2200 using MeO-DMBI-H or TEG-DMBI-H using charge density and mobility measurements	98
4.2.4 Temperature dependence of the electrical conductivity of doped N2200 using MeO-DMBI-H or TEG-DMBI-H	102
4.3 Grazing-incidence Wide-angle X-ray Scattering (GIWAXS)	104
4.4 Summary and Conclusion	109
4.5 Experimental Details	110
4.5.1 Synthesis	110
4.5.2 Characterizations: general procedures and experimental details	114
CHAPTER 5: Effects of crosslinking and dopant substituents: conclusions, future work and contributions	117
5.1 Overview	117
5.2 Future Work	120
5.3 Broader Impact of the Work Discussed in This Thesis	122

LIST OF TABLES

Table 4-1 conductivity values for doped N2200 polymer using MeO-DMBI-H and TEG-DMBI-H.....	97
Table 4-2 Doping efficiency values for doped N2200 polymer using MeO-DMBI-H and TEG-DMBI-H.....	100
Table 4-3 Field-effect mobility measurements on N2200 doped using MeO-DMBI-H or TEG-DMBI-H.....	102

LIST OF FIGURES

Figure 1.1 General diagram to demonstrate a simplistic picture involved in the doping of organic semiconductors. The actual process in many of the systems is more complicated than the one described above.	6
Figure 1.2 Energy diagrams of a) undoped OSC (ETM) and b) doped OSC depicting the lower electron injection barrier (ΔE_{inj}) on n-doping. The left side shows the situation when the electrode is not in contact with the organic semiconductor while the right side shows when the electrode is in contact with the organic semiconductor, and the Fermi level energies align. The dash line is the E_F of the semiconductor.	7
Figure 1.3 General diagram for the trap-filling and increase of free charge carriers upon n-doping.	8
Figure 1.4 Individual mechanisms occurring during molecular p-doping with organic semiconductors. a) In ion pair (IPA) formation, an electron is transferred from the HOMO of a host molecule to the LUMO of the dopant, to form a mobile hole charge carrier. b) Formation of a ground-state charge transfer complex (CPX) due to overlap of the frontier orbitals of host and dopant. Here, a new set of states is created for the complex.	9
Figure 1.5 Structures of the organic compounds and semiconductors that are discussed in this chapter.	10
Figure 1.6 Structures of the organic compounds and semiconductors that are discussed in this chapter.	11
Figure 1.7 Chemical structure of polymeric dopant and proposed doping interaction between sulfonic acid groups of dopant and thiophene units of P3HT.	21
Figure 1.8 Schematic image of OFET in which TCNQ was used as dopant-blockade molecule. The red regions in the middle of transistors are the TCNQ-incorporated regions. The yellow regions are the doped-polymer regions by using F ₄ -TCNQ dopant molecules and the dark blue is the undoped polymer region.	22
Figure 2.1 Synthesis of tetrakis-DMBI-H.	31
Figure 2.2 MALDI-TOF-MS spectra for the black precipitate from the reaction between tetrakis-DMBI-H and PCBM. Exact mass of PCBM is 910 m/z. The signal at 910 m/z in negative mode of MALDI is consistent with the presence of PCBM ⁻ in the reaction mixture.	32
Figure 2.3 Structures of different tetra-aldehydes with low solubility in CH ₂ Cl ₂ or MeOH.	33
Figure 2.4 Synthesis of tetrakis-O-DMBI-H as a more reactive multiple-hydride donor.	34

Figure 2.5 ESI spectrum obtained from the reaction product of tetrakis-O-DMBI-H and PCBM (4.0 equivalents).....	35
Figure 2.6 The initial product of nucleophilic attack and proton loss is likely the alcohol form (left), but this may well isomerize to the amide form.	36
Figure 2.7 a) UV-vis-NIR studies on doped PCBM before and after solvent treatment b) electrical conductivity of tetrakis-O-DMBI-H -doped PCBM (10 mol%) films before and after solvent treatment, c) and d) AFM images on tetrakis-O-DMBI-H -doped PCBM at 10 and 20 mol %.	37
Figure 2.8 Chemical structure on N2200 and TBDOPV-T polymers and UV-vis absorption spectra of pristine N2200 and tetrakis-O-DMBI-H-doped N2200.	39
Figure 2.9 a) Optical absorption spectra of undoped and tetrakis-O-DMBI-H -doped TBDOPV-T films before and after immersing into o-DCB for 5 min. b) Electrical conductivity of tetrakis-O-DMBI-H -doped TBDOPV-T films before and after dipping in o-DCB.	40
Figure 2.10 UPS a) secondary electron cut off (SECO) and b) valence band spectra with respect to the Fermi level EF of pristine (gray) and tetrakis-O-DMBI-H-doped TBDOPV-T (blue) films. The numbers next to the SECO spectra give the work function of the measured samples. Note that in (b) the main VB onset in the doped film is seen at higher binding energy than in the pristine material, but that there is also a new feature at low binding energy (indicated by dotted box).	42
Figure 2.11 Optical absorption spectra of (a) tetrakis-O-DMBI-H-doped TBDOPV, and sequentially deposited N2200 on tetrakis-O-DMBI-H-doped TBDOPV films before and after heating, (b) N2200 and sequentially tetrakis-O-DMBI-H-doped N2200.....	43
Figure 2.12 a) GIWAXS patterns of pristine TBDOPV-T and doped TBDOPV-T with different mol ratios of tetrakis-O-DMBI-H. b) 1D-GIWAXS linecuts of TBDOPV-T at different dopant ratios (in-plane direction), c) 1D-GIWAXS linecuts of TBDOPV-T at different dopant ratios (out-of-plane direction), d) lamellar distances, and e) relative degrees of crystallinity (rDoC).	46
Figure 3.1 Ring opening of benzocyclobutene to form the cross-linked product.....	56
Figure 3.2 Synthetic route for the synthesis of BCB-DMBI cation.....	58
Figure 3.3 MALDI-TOF-MS spectrum from the reaction products of compound 3.2 and 3.3.....	59
Figure 3.4 Assignments of possible chemical structures to the signals observed in MALDI-TOF-MS spectrum.	60
Figure 3.5 Synthesis of DMBI-H contains BBCB thermo-crosslinkable functional group, 3.7.....	61

Figure 3.6 Synthesis of related fullerene with a BBCB thermal crosslinker, BBCBPCB.	62
Figure 3.7 a) DSC thermogram of cross-linking reaction of BBCBPCB moieties and b) UV-vis absorption spectra of BBCBPCB annealed at different temperatures.	63
Figure 3.8 Schematic representation of oligomeric fullerene formation ((PCBCB) _n , n = 2) via thermal cross-linking of BBCBPCB.	64
Figure 3.9 MALDI-TOF-MS spectra for the black precipitate formed from the reaction between BBCB-DMBI-H and BBCBPCB. Peak at 1405 m/z represents the mass of the heterodimer.	65
Figure 3.10 UV-vis experiment performed to measure the film retention of BBCB-DMBI-H and BBCBPCB to o-DCB.	66
Figure 3.11 a) EPR spectra of BBCB-DMBI-H doped BBCBPCB and b) calculated g-values.	68
Figure 3.12 Synthesis route for BBCB-N-DMBI-H.	69
Figure 3.13 Comparison of normalized EPR spectra of BBCB-DMBI-H (red) and BBCB-N-DMBI-H doped BBCBPCB (gray).	70
Figure 3.14 MALDI-TOF-MS spectra from the reaction between BBCBPCB and BBCB-N-DMBI-H. The signal at m/z 586 represents the mass of BBCB-N-DMBI-H after loss of a hydride, the signal at 1671 represents the mass of BBCB-N-DMBI-H:BBCBPCB dimer.	71
Figure 3.15 Investigation of diffusion rate of thermo-crosslinkable BBCB-N-DMBI-H/BBCB-N-DMBI cation into 2CN-NDI as a strong electron acceptor.	72
Figure 3.16 Optical absorption of solution processed doped film of BBCB-N-DMBI-H doped 2CN-NDI (20 mol%).	73
Figure 4.1 Structures of some of the compounds in chapter 5.	91
Figure 4.2 Structures of the dopants discussed in Chapter 5.	93
Figure 4.3 Synthesis routes for MeO-DMBI-H and TEG-DMBI-H.	94
Figure 4.4 The UV-vis-NIR absorption spectra of pristine and doped N2200 with 30 and 70 mol% of MeO-DMBI-H and TEG-DMBI-H.	95
Figure 4.5 a) The architecture of the devices used for conductivity measurements and (b) The electrical conductivities for N2200 doped MeO-DMBI-H and TEG-DMBI-H at different mol ratios of the dopants.	97

Figure 4.6 a) The architecture of the devices used for charge-carrier density measurements and b) The charge-carrier densities for N2200 doped with MeO-DMBI-H and with TEG-DMBI-H at different molar ratios of the dopants.	99
Figure 4.7 The plots of electrical conductivities of a) MeO-DMBI-H doped N2200, b) TEG-DMBI-H doped N2200 as a function of the inverse temperature, c) the plot of activation energy as a function of dopant mol ratios for Me-ODMBI-H and d) TEG-DMBI-H.....	104
Figure 4.8 2D-GIWAXS patterns of pristine N2200 and doped N2200 with different mol ratios (0, 1, 5, 10, 20 mol%) of a) TEG-DMBI-H and b) MeO-DMBI-H.....	105
Figure 4.9 1D-GIWAXS linecuts of MeO-DMBI-H doped-N2200 at different dopant ratios, in-plane (IP) and out-of-plane (OOP) for lamellar distances.....	106
Figure 4.10 1D-GIWAXS linecuts of TEG-DMBI-H doped-N2200 at different dopant ratios, in-plane (IP) and out-of-plane (OOP) for lamellar distances.....	107
Figure 4.11 Relative degree of crystallinity (rDOC) from the integrated (lamella) pole figure.	108

LIST OF SYMBOLS AND ABBREVIATIONS

BBCB	Butoxybenzocyclobutene
DoC	Degree of crystallinity
DSC	Differential scanning calorimetry
E	Energy
E_F	Fermi level energy
E_v	Energy of valance band
K_B	Boltzmann's constant
ϵ_r	Relative permittivity of the dielectric
AFM	Atomic force microscopy
CPX	Charge transfer complex
EA	Electron affinity
ETM	Electron-transport material
ESI	Electrospray ionization
GIWAX	Grazing-Incidence Wide-Angle X-ray Scattering
HOMO	Highest occupied molecular orbital
IE	Ionization energy
IPA	Ion pair
LUMO	Lowest unoccupied molecular orbital
MALDI	Matrix assisted laser desorption ionization
NIR	Near-infrared
NMR	Nuclear magnetic resonance spectroscopy
o-DCB	Ortho-dichlorobenzene
OFET	Organic field-effect transistor

OLED	Organic light-emitting diode
OPV	Organic photovoltaics
PSCs	Perovskite solar cells
SECO	Secondary electron cut-off
UPS	Ultraviolet photoelectron spectroscopy
VB	Valence band
WF	Work function
XPS	X-ray photoelectron spectroscopy

SUMMARY

Doping is the process of addition of dopants to host semiconductors to improve their conductivity and charge transport behavior. Organic solids are held together by weak van der Waals interactions between the molecules and Coulombic attractions between the charged species. Because of these weaker interactions in organic materials, the molecules themselves have higher mobilities within the host material, and therefore, have a higher tendency to move. In most of the devices, the diffusion of the dopants in device stacks is detrimental and therefore, minimizing dopant diffusion within device interlayers is a very important topic to be consider. Considering the widespread usage of DMBI-H derivatives for doping of organic semiconductors, this work will focus on two aspects of doping; investigation of different approaches to address the diffusion of DMBI-H derivatives and studying the effect of dopant substituents on charge transport behavior.

The first and second chapters of this thesis, will focus on crosslinking as new approaches for minimizing the dopant diffusion in the solid state. Chapter 2 will discuss electrostatic crosslinking in which the restriction of dopant ion movement by forming multiple electrostatic sites between the multiply charged ions and ionized host segments. Chapter 3 will discuss chemical crosslinking and chemical bond formation to decrease the diffusion of dopant and the corresponding dopant ions. Chapter 4 will focus on a study in which the effect of a polar side chain on DMBI-H for doping of a donor-acceptor polymer. The final chapter summarizes the findings of the thesis, puts them in a broader perspective, and suggests future directions.

CHAPTER 1:

INTRODUCTION

1.1 Organic Electronics

Semiconductors play an important role in our daily lives as they are the materials used in the main components of modern electronics. Although most electronic devices like smartphones, photovoltaic cells, or light-emitting diodes (LEDs) in displays are still mainly composed of inorganic semiconductors (ISCs) such as silicon, the field of organic semiconductors (OSCs) has gained significant attention in the past decades, leading to the development of devices based on organic semiconductors.

The discovery and development of electrically conductive polymers, pioneering work of Heeger, MacDiarmid, and Shirakawa, has led to the development of organic electronic devices such as organic light-emitting diodes (OLEDs), organic field-effect transistors (OFETs), and organic photovoltaic cells (OPVCs). Today, OLED technology has already become a fast-growing commercialized technology and is mainly employed in TV or smartphone displays.¹ On the other hand, OFETs, have not yet reached the performance required for daily-use devices. However, current research shows promising progress in this field, and OFETs are expected to soon enter the market, for example, in the form of printed electronics such as radiofrequency identification (RFID) chips in intelligent labels.²⁻⁴ In the case of OPVCs, the research field has recently undergone dramatic changes with the development of the organic-inorganic metal halide perovskite solar cells (PSCs). While the attention has shifted from organic semiconductors to perovskites as active materials, organic hole transport layers (HTL) and electron transport layers (ETL) still being employed to facilitate efficient charge extraction in PSCs.⁵ With this new generation of

solar cells, power conversion efficiencies of over 25.6% have been achieved.⁶ Moreover, thermoelectric devices are widely used in energy conversion and local temperature control. Compared with thermoelectric metal alloys, polymer-based materials offer low toxicity, and solution processibility.⁷⁻¹⁰

The mechanical flexibility of OSCs makes them attractive for mobile and wearable applications.^{11, 12} Furthermore, the electronic and optical properties of OSCs can be easily tuned by their synthetic flexibility in a manner that has been well described in the literature.¹³ These properties make OSCs suitable for mass production in a wide range of applications. On the other hand, OSCs also show some disadvantages compared to ISCs. Many OSC-based devices currently still exhibit lower efficiencies and shorter lifetimes than their inorganic counterparts. The main disadvantage of OSCs is their very low charge carrier mobility due to low orbital overlap between the weakly interacting molecules. In addition, for some applications there can be a low density of charge carriers even when doped, which in turn, leads to low conductivities.

In organic devices, electrical doping can be used as a strategy to increase electrical conductivity and to lower energetic barriers to charge carrier injection or extraction at interfaces. In doping, impurities are purposely introduced into the semiconductor matrix by an external species (dopants), which either donate an electron (n-dopant) or accept an electron (p-dopant) from the host materials. The choice of dopant for an organic semiconductor is critical to ensure the dopant can have the desired influence on conductivity or on charge injection; without unwanted disruption of the semiconductor packing, without formation of by-products that interfere with the intended operation of the

device, while remaining confined in the desired region of the device under operating conditions.

In this chapter, after a short summary of the fundamentals of doping and introducing different classes of dopants, some of the current issues related to doping of OSCs will be discussed, following by solutions to address the issues.

1.2 Terminology and Definitions (Conductivity, Mobility, and Charge Injection Efficiency)

Electronic materials can be categorized into three categories based on their electrical conductivity (σ) – insulator, semiconductor, or conductor. Generally speaking, the conductivity at room temperature of insulators is less than $10^{-8} \text{ S cm}^{-1}$, conductivity of semiconductors lies within 10^{-8} to 10^2 S cm^{-1} , and conductors have conductivities greater than 10^2 S cm^{-1} . Ohm's law states the relationship between the current I (amperes, A) that passes through the semiconductor and the applied voltage V (volts, V) as follows:

$$V = IR \quad (1.1)$$

where R is the electrical resistance of the semiconductor, in unit of ohm (Ω). R is determined by the specific specimen geometry, while the resistivity, ρ , is independent of geometry and is a material-dependent factor. The resistivity is defined as:

$$\rho = R \frac{A}{l} \quad (1.2)$$

where l is the distance between the two points at which the voltage is measured, and A is the cross-sectional area which is perpendicular to the current direction. The unit for ρ is

ohm-centimeter ($\Omega\text{-cm}$). The electrical conductivity, σ , is also used to specify the electrical properties of organic semiconductors and is the reciprocal of the resistivity.

$$\sigma = \frac{1}{\rho} \quad (1.3)$$

The unit of σ is Siemens per centimeter (S cm^{-1}) where σ is defined as the ease with which a semiconductor is able to conduct an electric current.

Another important characteristic of an electronic material is the mobility (μ), which is the drift velocity per unit electric field, as shown in equation (1.4):

$$\mu = \frac{v}{E} \quad (1.4)$$

where μ is the mobility ($\text{cm}^2 \text{V}^{-1} \text{s}^{-1}$), E is the applied electric field, and v is the drift velocity (cm s^{-1}).

The relation between the electrical conductivity and the mobility is shown in equation (1.5).

In organic semiconductors, the charge carriers are either electrons (introduced by addition of electrons to the lowest unoccupied molecular orbitals) or holes (through removal of electrons from the highest occupied molecular orbitals).

$$\sigma = n\mu q \quad (1.5)$$

where n is the density of charge carriers (cm^{-3}), q is the elementary charge (C) and μ is the mobility ($\text{cm}^2 \text{V}^{-1} \text{s}^{-1}$).

Other than the conductivity and the mobility, the efficiency of charge injection/extraction from the electrodes to the material needs to be considered. A close match of the ionization

energy or the electron affinity of a material with the Fermi level energy (E_F) of the electrodes is important.^{14, 15} The ionization energy is defined as the energy required to remove an electron from an organic semiconductor to a level at which the electron is at rest. This is the distance from the surface that is beyond the influence of any significant electrostatic interactions with the surface (vacuum level (E_{vac})). The electron affinity is the energy released when an electron is added from the vacuum level to the semiconductor.¹⁶

The Fermi level energy for a semiconductor is the energy level for which the Fermi-Dirac distribution function has a value of 0.5. Another term that will be used in this thesis is the work function, which is the difference between E_{vac} and E_F or the energy required to remove an electron from the Fermi level energy to the vacuum level for a solid.¹⁷ The difference in the ionization energy and the electron affinity is referred to as the transport gap.

The ability of controlled doping can allow precise control of charge transport. Doped organic films can be processed either by co-evaporation¹⁸ of host and dopant in vacuum, or by adding a defined amount of dopant into a solution of the host material and processing the film by spin-coating, or by exposing the film or crystal to a solution or vapor of the dopant, so-called sequential doping.^{19, 20}

p-Dopants are materials with high electron affinities such that an electron can be transferred from the organic semiconductor to the p-dopant, thus adding holes in the organic semiconductor. In the other case, n-dopants are materials with relatively low ionization energy such that they can transfer electrons to the organic semiconductor (see Figure 1.1).



Figure 1.1 General diagram to demonstrate a simplistic picture involved in the doping of organic semiconductors. The actual process in many of the systems is more complicated than the one described above.

For both p- or n-doping, the conductivity of the organic semiconductor would increase due to addition of charge carriers. Apart from the conductivity, charge injection/extraction efficiency is also important, which to a large extent, depends on the position of the Fermi level energy (E_F) of the electrodes and the ionization energy and the electron affinity of a semiconductor. Ideally the work function (W_F) of an electron-injecting electrode in an OLED, should approach electron affinity (EA) of the organic semiconductor and ionization energy (IE) for a hole injecting electrode. On n-doping (p-doping), due to addition (removal) of electrons, the Fermi level energy of the semiconductor is shifted towards the empty states (filled states) as shown in Figure 1.2, which results in a decrease in the electron injection barrier in the case of n-doping, thereby facilitating an easier charge injection. Hence, electrical doping can significantly improve the performance of organic electronic devices as it leads to a reduction in the Ohmic losses by increasing the conductivity of the material and increasing the charge injection/extraction efficiency.²¹

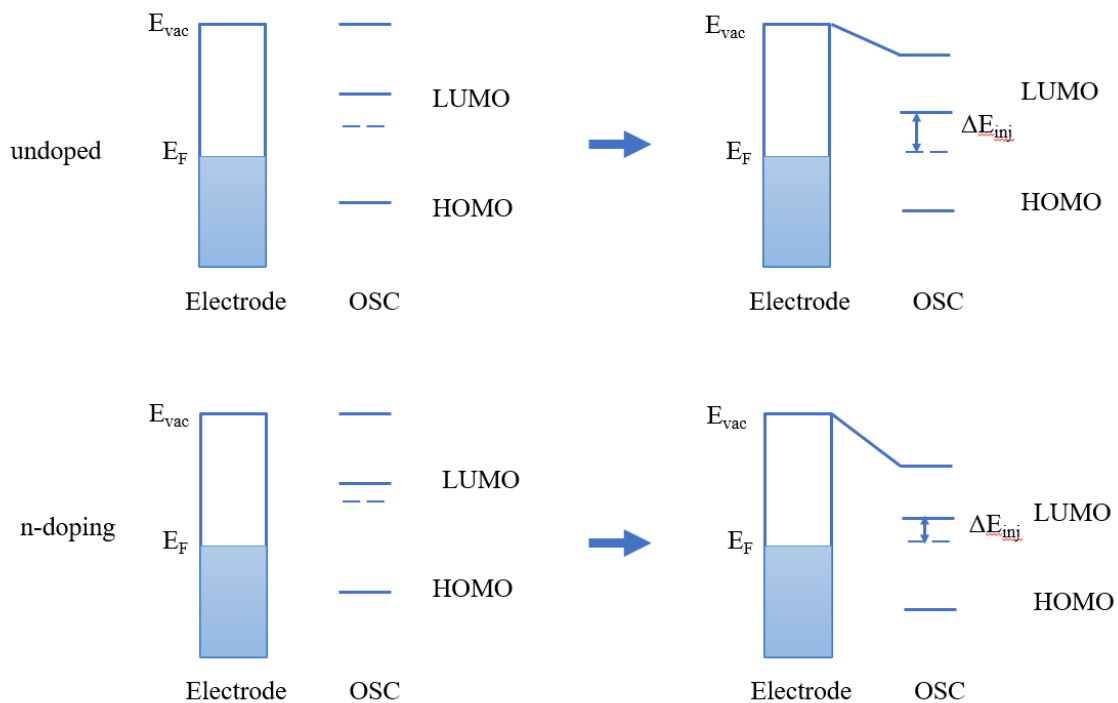


Figure 1.2 Energy diagrams of a) undoped OSC (ETM) and b) doped OSC depicting the lower electron injection barrier (ΔE_{inj}) on n-doping. The left side shows the situation when the electrode is not in contact with the organic semiconductor while the right side shows when the electrode is in contact with the organic semiconductor, and the Fermi level energies align. The dash line is the E_F of the semiconductor.

It is also worth mentioning that, in most organic semiconductors, the charge transport takes place by hopping and the presence of impurities and defects in organic semiconductors lead to the formation of trap states. These trap states are lying deeper in the gap than the effective transport states, which will hinder the charge transport and leads to low charge mobility. Upon doping, these deep traps are filled and the energy distribution of occupied states are raised, thus increasing the charge carrier density in an energetically disordered hopping system will increase the mobility,²² Figure 1.3.

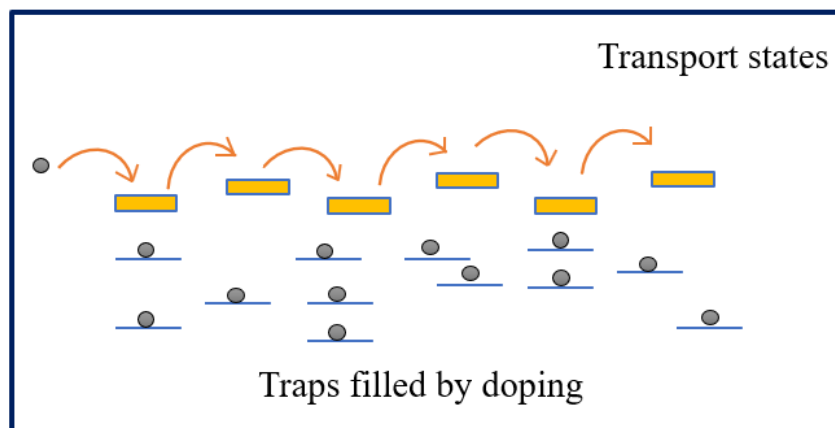


Figure 1.3 General diagram for the trap-filling and increase of free charge carriers upon n-doping.

1.3 Mechanism of Molecular Doping of Organic Semiconductors

For molecular doping of organic semiconductors, there are two suggested mechanisms that describe the interaction between dopant and host: 1) ion pair (IPA) formation and 2) ground state charge transfer complex (CPX) formation. Both of these mechanisms can be spectroscopically proved by the observation of diagnostic absorption features of the molecular ions.^{23, 24} The following description is based on p-type doping but all mechanisms could occur for n-type doping.

In the case of IPA formation (Figure 1.4 (a)), an electron is transferred from the energetically higher lying HOMO level of the host to the LUMO level of the dopant resulting in the formation of an ion pair, the host cation and dopant anion. For this process to happen, EA of the dopant should be higher than IE of the host. For IPA formation, it is generally assumed that the electron on the dopant is static, while the hole in the HOMO of

the matrix molecule is mobile, contributing to an increase in mobile charge carriers and, therefore, an increase in conductivity.

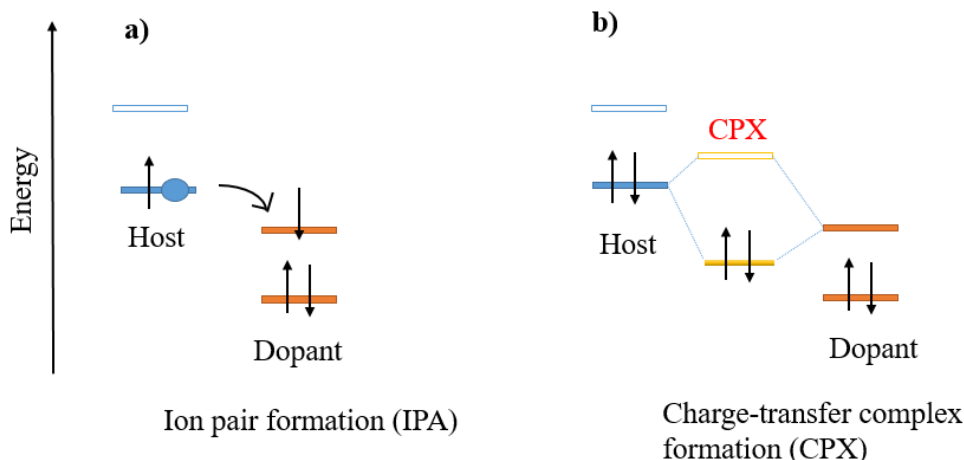


Figure 1.4 Individual mechanisms occurring during molecular p-doping with organic semiconductors. a) In ion pair (IPA) formation, an electron is transferred from the HOMO of a host molecule to the LUMO of the dopant, to form a mobile hole charge carrier. b) Formation of a ground-state charge transfer complex (CPX) due to overlap of the frontier orbitals of host and dopant. Here, a new set of states is created for the complex.

In the case of CPX formation (Figure 1.4 (b)), the frontier molecular orbitals of the dopant and the host molecule interact and hybridize in a supramolecular complex forming a set of new HOMO/LUMO states. However, since the newly created empty level of the complex lies above and the filled level below the HOMO of the host, the CPX complex requires an additional energy to be ionized and allow the creation of a mobile hole in the host matrix. As a result, CPX formation results in low doping efficiency, therefore, not favorable for applications.²⁵ Since CPX formation requires a strong overlap of the frontier orbitals of both host and dopant, a strategy to avoid CPX formation is to use bulky host or dopant molecules with side-groups, which lead to steric hindrances effectively prohibiting an overlap of the frontier orbitals.²⁶

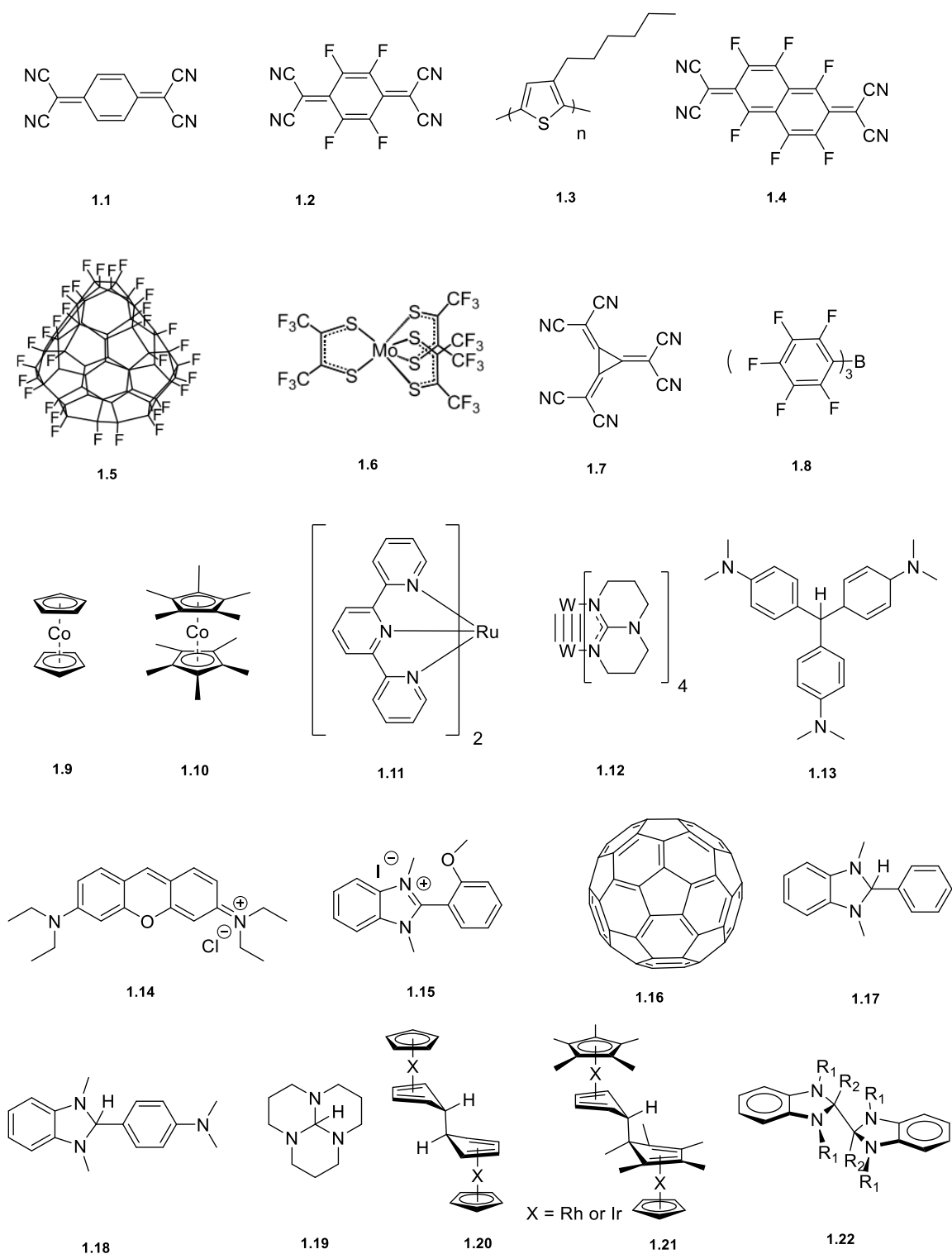


Figure 1.5 Structures of the organic compounds and semiconductors that are discussed in this chapter.

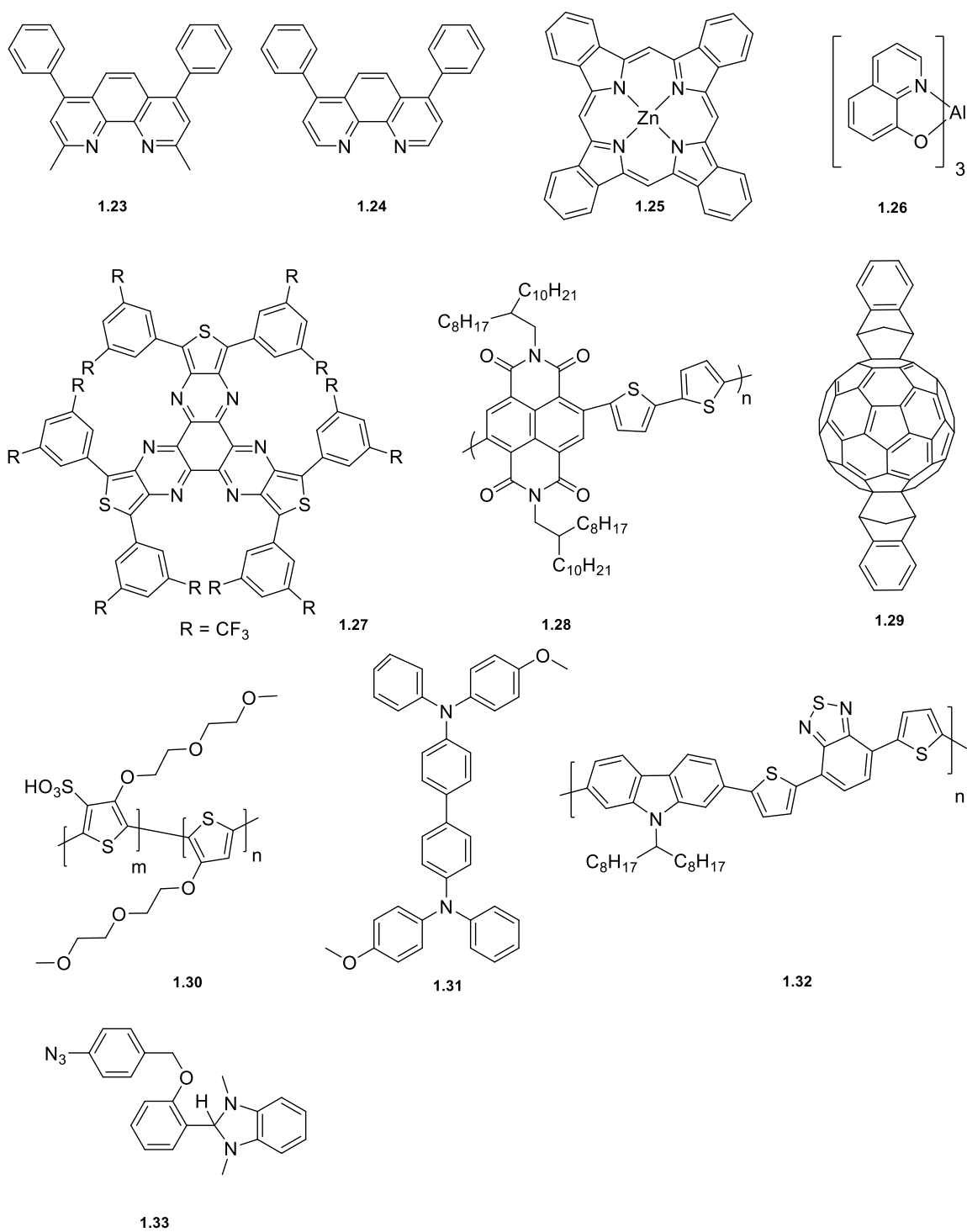


Figure 1.6 Structures of the organic compounds and semiconductors that are discussed in this chapter.

1.4 Classes of Dopants

This section will briefly summarize and compare the major classes of p- and n-dopants.

1.4.1 *p-Dopants*

Elemental species like iodine (I₂), Bromine (Br₂), and chlorine (Cl₂) have been recognized as p-dopants for organic semiconductors. For example, iodine has been used for doping of pentacene, phthalocyanines, and polythiophenes.²⁷ Beside high diffusibility tendency of these diatomic dopants, they can be also difficult to handle due to their volatility and in some cases corrosivity and toxicity.^{27, 28}

The molecular p-dopant TCNQ **1.1** (tetracyanoquinodimethane) with EA of 4.2 eV has been developed and studied in detail due to its ability to form charge-transfer salts with small-donor molecules.^{29, 30} However, due to a relatively low EA,³¹ TCNQ is not able to dope many application-relevant organic semiconductors. For the same purpose, molecular dopants with higher EAs have been designed. These dopants are electron-poor structures with electron-withdrawing functional groups such as -CF₃, -COCF₃, -CN, -F.

The fully fluorinated version of TCNQ is F₄TCNQ, **1.2** (2,3,5,6-tetrafluoro-7,7,8,8-tetracyanoquinodimethane), which has a EA of 5.2 eV and is able to dope a wide range of organic semiconductors.^{23, 32, 33} However, F₄TCNQ was shown to be highly volatile, **1.3**, and can also diffuse in polymers such as P3HT when an electric field is applied.^{34, 35} Larger dopants such as F₆TCNNQ (**1.4**, EA = 5.6 eV)³⁶ and larger fluorinated organic molecules based on fullerenes (e.g., C₆₀F₃₆, **1.5**)^{37, 38} have been developed. Due to their higher molecular weight, these dopants have a higher sublimation temperature and can reliably be

evaporated, nevertheless F₆TCNNQ has poor solubility in common solvents. Metal-organic dopant molybdenum tris[1,2-bis(trifluoromethyl)ethane-1,2-dithiolene] Mo(tfd)₃, 1.6, EA = 5.6 eV)³⁹, hexacyano-trimethylene-cyclopropane (CN6-CP, **1.7**, EA = 5.9 eV)⁴⁰,⁴¹ and trimethyl 2,2',2''-(cyclopropane-1,2,3-triylidene)-tris(cyanoacetate) (TMCN₃-CP)⁴², an analog of CN6-CP in which three of the six nitrile groups are replaced with methyl esters, are all another potent molecular p-dopants that have been used for p-doping of semiconductors.

Other used p-dopants for organic semiconductors are Lewis acids (e.g., FeCl₃)⁴³ with higher solubility than molecular p-dopants that allow processing from higher concentration stock solutions. Recently, the strong Lewis acid tris(pentafluorophenyl)borane ([B(C₆F₆)₃], **1.8**)⁴⁴ has been used and shown to be able to effectively p-dope P3HT, resulted in three times higher conductivities than F₄TCNQ doped P3HT, which was related to the improved film quality.

1.4.2 *n-Dopants*

Strong molecular n-type dopants are scarce. A low ionization energy is required for effective electron transfer to most organic semiconductors that makes it challenging to design a dopant with air stability and that is also highly reducing. An ideal n-dopant needs to have the following characteristics: 1) the ability to dope a wide range of electron transport materials; 2) the ability to transfer electrons into host materials with no side reactions; 3) formation of a stable doping product that does not diffuse or does not act as an electrostatic trap for charge carriers; and 4) air-stability. The ability of a dopant to be able to dope a wide range of hosts and have a reasonable air stability cannot be

simultaneously achieved, and the work on improving dopant air stability generally has involved coupling of doping to other chemical processes.

The first class of n-dopants is the alkali and alkaline earth metals, e.g., Li, Na, K, and Cs, which have all been widely used as n-dopants for various applications. For example, poly(p-phenylene) polymer films have shown more than ten orders-of-magnitude higher conductivity upon exposure to potassium.⁴⁵ However, the drawbacks of electrical doping using alkali metals are their high reactive nature and high diffusivity.⁴⁶⁻⁴⁸

Low ionization energy donors are another class of n-dopants that are intrinsically sensitive to oxidation. For example, cobalt bis(cyclopentadienyl) $\text{Co}(\text{Cp})_2$, **1.9**, has a solid-state ionization energy of 4.07 eV that can increase the conductivity of tris(thieno)hexaazatriphenyl derivative by three orders-of-magnitude.⁴⁹ Introduction of methyl groups on the Cp ring, **1.10**, increases the reducing strength, resulting in a lower ionization energy of 3.30 eV. $\text{Ru}(\text{terpy})_2$, **1.11**, also was reported to have an ionization energy similar to $\text{Co}(\text{Cp}^*)_2$ that was strong enough to dope materials used in OLEDs.^{50, 51} The donor with perhaps the lowest ionization energy for a molecular dopant is $\text{W}_2(\text{hpp})_4$ (**1.12**) which has a solid-state ionization energy of only 2.40 eV.⁵² However, n-dopants with such low ionization energies are sensitive to oxidation, especially in the case of $\text{W}_2(\text{hpp})_4$, and care must be taken in handling these materials.

To obtain sufficiently reducing and relatively air-stable n-dopants, several classes of n-dopants have been developed in which electron transfer reactions are coupled with other chemical reactions. One such a class is the cationic organic salts, such as pyronin B chloride, **1.14** and 1,3-dimethyl-benzimidazoliums such as 2-(2-methoxyphenyl)-1,3-

dimethyl-1*H*-benzoimidazol-3-ium iodide (MeO-DMBI-I, **1.15**). They can be deposited through co-evaporation with a host that leads to the formation of the reducing species upon heating.^{53, 54} The conductivity of doped C₆₀ films with MeO-DMBI-I could reach 5.5 S cm⁻¹, >100 times higher than undoped films. Unfortunately, the doping mechanism of these salt dopants is not well understood. The formation of neutral radicals or hydride-reduced intermediates upon deposition has been suggested without direct evidence.⁴³

DMBI-Hs (1,3-dialkyl-2,3-dihydro-1*H*-benzoimidazole, **1.17**) derivatives are another class of n-dopants that have attracted significant attention due to their air stability and straightforward synthesis.⁵⁵ The most widely used is 1,3-dimethyl-2-(4-(dimethylamino)phenyl)-2,3-dihydro-1*H*-benzoimidazole, N-DMBI-H, **1.18**, and high electrical conductivities have been obtained with some semiconductors.⁵⁶⁻⁶¹ For several classes of organic semiconductors, the mechanism has been shown to involve a hydride transfer from the dopant to OSCs as will be discussed in detail in Chapter 2.,^{62, 63} Triaminomethane derivatives (TAM, **1.19**) are another group of hydride donor dopants that have been recently introduced by the Pei group. TAM exhibited extremely high stability and hydride donating properties due to its thermally activated doping mechanism. As depicted with both experimental and computational studies, TAM is a kinetically weaker but thermodynamically stronger hydride nucleophile compared with N-DMBI-H. As a result, TAM exhibits higher activation energies than N-DMBI in n-doping reactions. Moreover, TAM shows excellent counter ion-semiconductor miscibility, high doping efficiency, and uniformity.⁶⁴ However, the small size of TAM ions could potentially increase their diffusion within a doped device possible.

Dimers of organic radicals are another class of n-dopants. The concept originates from the idea that an air-sensitive dopant radical can be stabilized by forming a weak C-C bond. Air-stability and the ability to dope weak electron acceptors are the main advantages of dimeric dopants. Moreover, the cation size is tunable to enable some control over ion diffusivity, deposition rates. There are examples of nineteen-electron transition metals (sandwich compounds) that tend to dimerize and form eighteen-electron configurations, including rhodocenes, iridocenes (**1.20** and **1.21**), and some mixed cyclopentadienyl/arene sandwich compounds of iron and ruthenium.^{65, 66} This work was extended to dimers of organic radicals of DMBI compounds (DMBI)₂, **1.22**.⁶⁷ Compared to DMBI-H derivatives, (DMBI)₂ analogs led to faster formation of the host anions and a more reliable and predictable doping reaction between the hosts with similar electron affinities. Several organometallic and (DMBI)₂ dimers have effective ionization energies close to that of decamethyl cobaltocene, which in contrast, can be handled in the air as solids.^{68, 69}

1.5 Why Is Diffusion of Dopants in Solid State Important?

The diffusion of dopants or dopant ions in organic semiconductors is a very important topic to be considered. Organic solids are held together by weak van der Waals interactions between the molecules and Coulombic attractions between the charged species. Because of these weaker interactions in organic materials, the molecules themselves have higher mobilities within the host material, and therefore, have a higher tendency to move. Depending on the applications, the diffusion or drift (migration under applied field) of the dopant could be beneficial or detrimental for device performance.

For example, for organic thermoelectric devices used in energy conversion and local temperature control, millimeter (mm)-thickness doped semiconductor structures are needed for optimal thermoelectric performance. While co-deposition of the dopant and organic semiconductor is a convenient and one-step process for thermoelectric materials, sequential doping offers higher thermoelectric properties. This is because the sequential doping allows optimization of the solid-state nanostructure of the organic semiconductor prior to doping. Unfortunately, sequential doping of (mm)-thick, solid semiconductor structures is not trivial because of the limited diffusion rate of dopant molecules in semiconductors. The Müller group has addressed this issue by assisting the transport of the dopant using foams that readily permit sequential doping of thick semiconductor structures. They demonstrate that by thermally induced phase separation combined with salt leaching, centimeter (cm)-thick P3HT foams with a microporous internal structure could be obtained that would uptake F₄TCNQ dopant molecules more quickly and more efficiently than bulk P3HT.⁷⁰

Although improving the diffusion rate is beneficial for thermoelectric devices and even for thin layer devices that are doped using a sequential doping method, the diffusion of dopant molecules within and between layers of a device can greatly hinder the performance by causing unwanted interactions with other materials. Unfortunately, there have been very few studies directly investigating this process. In the following section, it will be briefly discussed the cases in which possible diffusion of the dopants were studied, followed by the approaches that have been taken to address and suppress the diffusion of dopants in solid-state.

1.5.1 Literature review on diffusion of dopants in OSCs

As mentioned earlier, the alkali and alkaline earth metals have been widely used as n-dopants for various applications. However, considering their small size, alkali metal ions are highly prone to diffuse. For example, Parthasarthy has studied electrical doping of 2,9-dimethyl-4,7-diphenyl-1,10-phenanthroline, **1.23** (BCP), with lithium metal, and the diffusion profile of lithium metal into the organic material was investigated.⁴⁶ In the architecture, ITO/organic layer (10-640 nm)/ Li (0.5–1 nm)/Al, secondary ion mass spectrometry indicated lithium diffusion up to 80 nm into the organic material. In another study, Forrest et al. have observed the diffusion of lithium up to 17.5 nm into 4,7-diphenyl-1,10-phenanthroline film layer, **1.24** (BPhen), leading to short operational lifetimes for multilayer OLEDs in which these films were used as electron injection layers.⁷¹

The issue of the diffusion of the dopant ions is not restricted to alkali metals, and small molecular dopants are also prone to diffusion. Kahn's group investigated the diffusion of F₄TCNQ in zinc phthalocyanine, **1.25**, by depositing zinc phthalocyanine on top of **1.2** a cold gold substrate. Monitoring the intensity of the F(1s) ionization in the XPS with time, they observed a dramatic increase in the peak intensity of the F(1s) as the substrate was warmed up to the room temperature; The small dopant molecules F₄-TCNQ appear to diffuse throughout the host near the surface of **1.25**.³²

In a separate study, the Srivastava group has identified the fluorescent quenching of tris(8-hydroxyquinolino) aluminum (AlQ₃, **1.26**), caused by the diffusion of F₄-TCNQ from an adjacent layer using photoluminescence (PL) spectroscopy. The effect of the concentration of the F₄-TCNQ was investigated by varying the thickness of the dopant (F₄-TCNQ). PL

intensity has been reduced by increasing the F₄-TCNQ, and quenching efficiency was evaluated as the function of the distance between the dopant and the active layer. Diffusion lengths were evaluated to be higher with increasing the thicknesses of F₄-TCNQ.⁷²

In other cases, the dopant lacks diffusion in the host matrix; however, the dopant might diffuse under the applied electric field. For example, the Lovrincic group investigated the impact of an electric field operating conditions on thin films of the polymer P3HT, doped with Mo(tfd-CO₂Me)₃ dopant by obtaining the I-V curve.³⁴

In principle, for doped semiconductors, upon a certain field strength, the dopant ions (depends on the charge) start to drift toward the electrode, in the opposite direction to the charge-carrier current. Consequently, a region of dedoped semiconductor is generated, which exhibits a much larger resistivity compared to the doped semiconductor. Hence, the voltage drop no longer occurs linearly over the whole channel but mostly over the dedoped region and at the dedoped electrode contact. The width of the dedoped region is influenced by the strength and duration of the applied field. Therefore, a hysteresis in the I–V curves was found for films of P3HT doped with Mo(tfd-CO₂Me)₃.

1.5.2 Different strategies reported in the literature to suppress the diffusion of dopants in solid state

A variety of strategies have been investigated to minimize the diffusion of n-type and p-type dopants in the solid-state.

Kahn group reported on the solution-based p-doping of P3HT with $\text{Mo}(\text{tfd-CO}_2\text{Me})_3$ using soft-contact lamination of ultra-thin (30 nm) p-doped P3HT layers. They demonstrated significant enhancement of hole injection into undoped P3HT, as well as efficient hole collection from solution-processed bulk-heterojunction solar cells composed of P3HT and either PCBM or P3HT:ICBA. Later on, they investigated the diffusion of $\text{Mo}(\text{tfd-CO}_2\text{Me})_3$ into pure P3HT and the P3HT:ICBA blend active layer.⁷³

They observed that p-dopant $\text{Mo}(\text{tfd-CO}_2\text{Me})_3$ diffuses extensively at room temperature in pure P3HT films. However, the diffusion rate is minimized by spatially-confined doping method, where the dopant diffusion pathway was filled using ICBA, **1.29**.⁷⁴ Spatial confinement of dopants is proved to be useful for the stability of organic devices.⁷⁵

Controlling the diffusion of dopants is critical in OFETs as well. In contact doping, that is the introduction of external dopant molecules near the contact region, has been used as an effective method for improving contact properties. In contact doping, a high level of dopant is required to enhance charge injection. However, a high dopant level leads to faster diffusion of dopant molecules within the host semiconductor. To address this issue, the Gomez group has demonstrated that contact doping in organic electronics is possible through ionic polymer dopants, which resist diffusion or migration due to their large size.⁷⁶

Figure 1.7 demonstrates the chemical structure of polymeric dopants based on

poly(sulfone) backbones and proposed doping interaction between sulfonic acid groups and thiophene units of P3HT. Spin-coating of 3.0 nm thin layer of dopant polymer on anode semiconductor interface of organic photovoltaics enables efficient hole extraction at the anode.

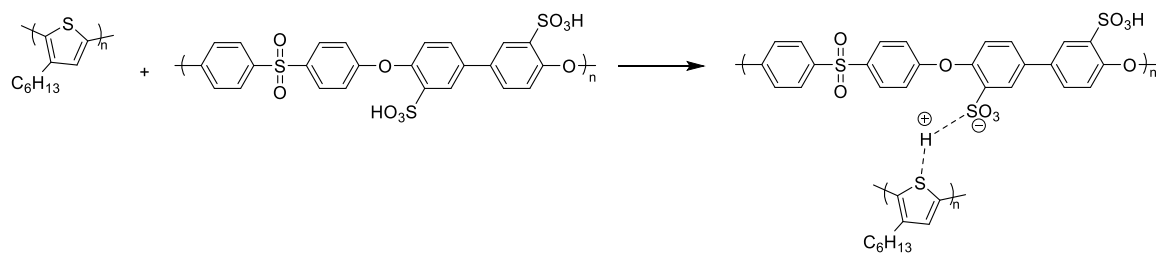


Figure 1.7 Chemical structure of polymeric dopant and the proposed doping interaction between sulfonic acid groups of dopant and thiophene units of P3HT.

The Kang group used TCNQ as a dopant-blockade molecule, spatially blocking the diffusion pathways of the dopants within the active channel region, to suppress the diffusion pathways of dopants in the active channel region of the OFET. Dopant-blockade molecules are required to be electrically inactive to locate themselves in the diffusion paths of the dopant. However, processing becomes more difficult using this method, as more processing steps is required for incorporation of the dopant-blockade molecule. Moreover, there are possible complications regarding charge transport or energy level alignment from the additional dopant blocking materials since they might act like charge traps, Figure 1.8.⁷⁷

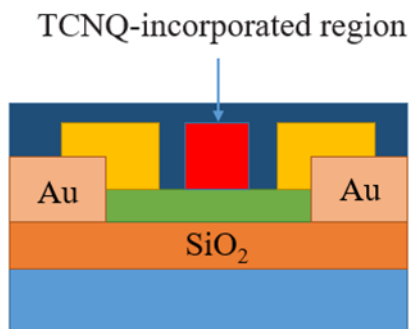


Figure 1.8 Schematic image of OFET in which TCNQ was used as dopant-blockade molecule. The red regions in the middle of transistors are the TCNQ-incorporated regions. The yellow regions are the doped-polymer regions by using F₄-TCNQ dopant molecules and the dark blue is the undoped polymer region.

Another strategy used to decrease the diffusion of dopants in solid-state is by introducing polar side chains onto polymers to increase dopant affinity. For example, by incorporation of polar side chains on P3HT analog, poly(thiophene-3-[2-(2-methoxy-ethoxy)ethoxy]-2,5-diyl) (SeP3MEETS-P3MEET, **1.30**), F₄TCNQ dopants were found to be retained in the polymer even with heating up to 150 °C, while very little F₄TCNQ remains in the P3HT layer. In this study S-P3MEET/P3HT bilayers were fabricated. First, the bilayer sample with dopant starting in S-P3MEET was investigated. P3HT film was spin-coated onto a F₄TCNQ doped S-P3MEET layer. UV-vis absorbance was recorded before and after thermal annealing. The absorbance spectra did not show any significant differences. Second the bilayer sample with dopant starting in P3HT was investigated. A S-P3MEET film was spin-coated onto the top of F₄TCNQ doped P3HT. Upon thermal annealing, UV-vis spectra showed reduced P3HT absorbance and appearance of a broad signal corresponded to P3HT polaron and after annealing to 180 °C, F₄TCNQ started to leave the P3HT layer. It is likely that the polar side chain of S-P3MEET causes the strong binding of the F₄TCNQ and restricts its diffusion. In contrast, the alkane side-chain of P3HT does

not have polar bonds to orient and consequently, is not able to contribute to binding F₄TCNQ.⁷⁸

Using larger molecular dopants is another strategy to minimize the diffusion of dopants. The Moule group had used perfluorinated fullerene, C₆₀F₃₆, dopant that has larger molecular size/geometry compared to F₄TCNQ dopant. Using the near-edge X-ray absorption spectroscopy, they monitored the diffusion of each dopant into the MeO-TPD layer. A bilayer of 30 nm MeO-TPD layer on the top of 30 nm of each dopant (MeO-TPD/F₄TCNQ or MeO-TPD/C₆₀F₃₆) were fabricated. The normalized carbon K-edge spectra of each bilayer structures before and after annealing were showed that unlike F₄TCNQ, two distinct layers of C₆₀F₃₆ remain intact up to 110 °C. By increasing the annealing temperature higher than 110 °C, slightly increase of C₆₀F₃₆ dopant content into MeO-TPD surface was observed. The differences in the diffusion rates of F₄TCNQ and C₆₀F₃₆ through MeO-TPD were attributed to the differences in molecular size. Given the smaller size and more planar structure of the F₄TCNQ, it can more easily migrate into MeO-TPD.³⁸

In another strategy, the Aizawa group has used phosphomolybdic acid (PMA) as a strong oxidizing agent to crosslink polycarbazoles via an oxidative coupling.⁷⁹ This reaction occurs rapidly under thermal annealing at a temperature of 110 °C within a few minutes to connect two carbazoles. However, following this approach, p-type doping was not observed. Later on, Aizawa in collaboration with Kippelen group has demonstrated simultaneous insolubilization and p-doping of a polymer, poly[*N*-*N*'-heptadecanyl-2,7-carbazolealt-5,5-(4',7'-di-2-thienyl-2',1',3'-benzothiadiazole)](PCDTBT, **1.32**).⁸⁰ This process occurs by post-processing immersion of polymer films into a solution PMA in nitromethane. To cross-link and p-dope PCDTBT films, films spin-coated from

chlorobenzene on quartz substrates, 30 nm-thick PCDTBT were submerged into nitromethane solution (0.5 M of PMA) for up to 60 min, and then rinsed with pure nitromethane. In this process, the PCDTBT films do not dissolve in nitromethane, but allow PMA molecules to diffuse and introduce free holes through the films. The resulted films became completely insoluble to common organic solvents. This method is a very effective and promising method for doping and insolubilization of p-type polymers such as P3HT. P3HT films immersed for 30 min in a 0.5 M solution of PMA in nitromethane also demonstrated increased electrical conductivity and reduced solubility in the processing solvent.⁸¹

Intermolecular cross-linking is another approach to prevent dopant diffusion within device interlayers. A covalent bond between the dopant and the host molecule would allow a stronger interaction between the two components. A premodification of the dopant with a photo-crosslinkable functional group (azide) was used to localize an n-type dopant DMBI-H, **1.33**.⁸² The azide is activated by deep-ultraviolet light (UV, 254 nm), inducing photolysis and generating reactive singlet nitrenes that selectively insert into aliphatic CH bonds.⁸³ The covalent attachment of the dopant to the PCBM as a host was demonstrated using electrospray ionization (ESI) and matrix-assisted laser desorption ionization (MALDI). To investigate the migration of dopants under applied voltage, the I–V curve of a **1.33** doped PCBM layer that was UV-treated (followed by a final annealing step) displays no or reduced hysteresis, which was an indication for a successful dopant immobilization after nitrene generation. Although the dopant was immobilized under crosslinking conditions, the dopant seems to be less stable in the solution.

1.6 Thesis Structure and Overview

This chapter was intended to inform the reader about the efforts that have been made by the scientific community in the area of organic electronics to identify and address the diffusion of dopants in OSCs. As it was already mentioned, there are limited studies to address the diffusion of dopants, especially for n-type doping. In the following chapters, the focus will be on different approaches to further investigate and address the diffusion of dopants.

Chapter 2 of the thesis will focus on the design and synthesis of a new derivative of DMBI-H in which 4 units of DMBI-Hs are connected via an sp^3 linker. We have investigated the effect of multiple electrostatic interactions of dopant cation with acceptors (small molecules, PCBM) and (polymers, N2200 and TBDOPV-T). The mechanistic studies have shown that the dopant is able to form a tetracation under thermal annealing with PCBM. Film retention studies revealed that insolubilized doped film could be obtained with both PCBM and TBDOPV-T polymer that could contribute to immobilization of the dopant in solid-state.

Chapter 3 will discuss incorporation of thermos-crosslinkable benzocyclobutane (BCB) group on both the hydride transfer dopants (DMBI-H) and electron acceptor fullerene. The focus of this chapter is immobilization of n-type dopant via covalent anchoring. To avoid the degradation of dopant under cross-linking condition, the low temperature BCB crosslinker with alkoxy side chain was chosen. Film retention studies show formation of insoluble doped film. The doped semiconductors were characterized using EPR and mass spectrometry.

Chapter 4 of the thesis will focus on doping of an n-type polymer (N2200) with two derivatives of DMBI-H and compare the electrical conductivity values and charge carrier densities.

Finally, Chapter 5 summarizes the results reported throughout this thesis. This chapter will inform the reader about the attempts made in this work to design and develop small molecules to minimize the diffusion of the dopants in device stacks. This chapter will comment on future directions of this research to find out new ways to minimize the diffusion of dopants in semiconductors and discuss briefly about the broader impact of the work.

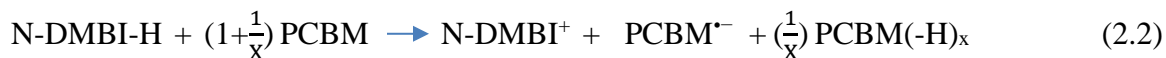
2.1 Introduction

As it was discussed in Chapter 1, DMBI-H derivatives have been extensively used for the n-doping of many organic semiconductors for various applications^{57-61, 84, 85}. A variety of DMBI-H derivatives have been synthesized to tune their reactivity with hosts,^{86, 87} to increase their air stability in the solution,⁸⁸ and to improve miscibility with the semiconductor.^{89, 90}

The mechanism of the reaction of the DMBI-H derivatives with different host semiconductors has been investigated by Marder group. There is a strong evidence that suggests the first step of mechanism of the solution reaction of DMBI-H and the fullerene derivative (PCBM) is a hydride transfer reaction. A comparison of reaction rates using N-DMBI-H and N-DMBI-D reveals a primary kinetic isotope effect (KIE), which is consistent with C–H bond cleavage being the rate-determining step.⁶²



The products of this reaction are PCBM-H[−] and N-DMBI⁺. PCBM-H[−] is thought to then undergo a rapid electron transfer to PCBM to form the desired radical PCBM^{•−} and PCBM-H[•]. Partially hydrogenated fullerene could also be detected, so that the overall reaction is thought to be as follows:



The reactivity of DMBI-H derivatives has also been investigated with imide- and amide-containing semiconductor molecules, for the more reactive of which the reaction is also found to proceed via an initial hydride transfer step,⁶³ similar to the reaction with PCBM.

Dopant ions are bound to the host via relatively weak van der Waals and Columbic interactions and because of these weak interactions, ions may be prone to migrate through diffusion or drift when the doped semiconductors with these ions are used in devices (e.g. OLEDs and OPVs). Although DMBI-H derivatives have been used for doping of numerous semiconductors, there are few studies addressing the immobilization in order to decrease their diffusion rate and migration in the devices.

As it was discussed in Chapter 1, the Müllen group had installed a photo-crosslinker azide functional group on a DMBI-H derivative.⁸² They studied the diffusion of dopant under applied field for the N₃-DMB-H doped PCBM and, indeed, cross-linking was found to help to minimize the diffusion of dopant under applied field. However, no data was reported showing the diffusion of dopant under thermal annealing as heat might be expected to trigger the diffusion of dopant molecule/ions in device stacks. Moreover, no evidence was reported regarding the film retention against solvents for the crosslinked system.

In this chapter, decreasing the diffusion of DMBI-H dopants is explored using a different approach. Taking advantage of electrostatic interactions between the dopant ions and ionized host segments, it was hypothesized that an oligomeric derivative of DMBI-H that is able to transfer multiple hydrides to host semiconductors, decreases the diffusivity of the dopant ions. Multiple Columbic interactions of the resultant multi-charged cations and the

radical anions of the acceptor molecules could possibly lead to the decreased mobility of the dopant ions.

The Columbic interactions could be beneficial in two different ways; decreasing the diffusion rate of cation into adjacent layers in a device and render the doped material insoluble, which could facilitate the solution-processed deposition of a subsequent layer without washing away the doped layer. To test the hypothesis, a tetrakis-DMBI-H in which 4 DMBI-H units are linked through a sp^3 carbon was synthesized. Subsequently, it was demonstrated that the dopant is able to transfer up to 4 hydrides to a host acceptor, and the details will be discussed in the following sections.

2.2 Synthesis of Tetrakis-DMBI-H

In general, the synthesis of DMBI-H derivatives is straightforward using the reaction of *N,N'*-dimethyl-1,2-phenylenediamine and the corresponding aldehyde in the presence of catalytic amount of acid.⁵⁵ For synthesis of a tetrakis-DMBI-H, a tetra-aldehyde derivative is needed and, therefore, compound **2.3** (Figure 2.1) was synthesized in two steps⁹¹ and subsequently underwent reaction with 4.0 equivalents of *N,N'*-dimethyl-1,2-phenylenediamine **2.4** in MeOH. The desired dopant **2.5** was recrystallized from MeOH.

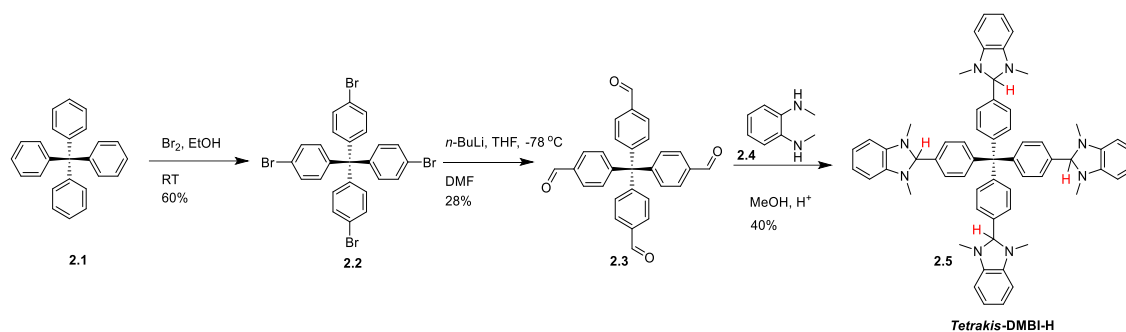


Figure 2.1 Synthesis of tetrakis-DMBI-H.

2.2.1 Mechanistic studies of tetrakis-DMBI-H and PCBM

In order to investigate whether tetrakis-DMBI-H is able to dope PCBM, tetrakis-DMBI-H and PCBM (1:4 equivalents (5 mg tetrakis-DMBI-H and 22 mg of PCBM in 1.0 mL of CB)) were mixed in chlorobenzene (CB) (under nitrogen atmosphere in glove box) and the reaction was monitored. After 3 days some black precipitate was observed in the reaction mixture. The black solid was insoluble in solvents such as THF, CH₃CN, CH₂Cl₂, and acetone, but soluble in DMF. As we have discussed, the products of the reaction of PCBM/DMBI-H are PCBM^{•-} and DMBI⁺. PCBM^{•-} absorbs in the NIR region with a peak at ~1000 nm.⁶² Unfortunately, we were not able to detect PCBM^{•-}, after dissolving the precipitate in DMF, using UV-vis-NIR. However, the composition of the black precipitate was investigated by mass spectrometry, which identified a peak consistent with PCBM mass at the negative-ion mode, consistent with the formation of PCBM^{•-}, Figure 2.2.

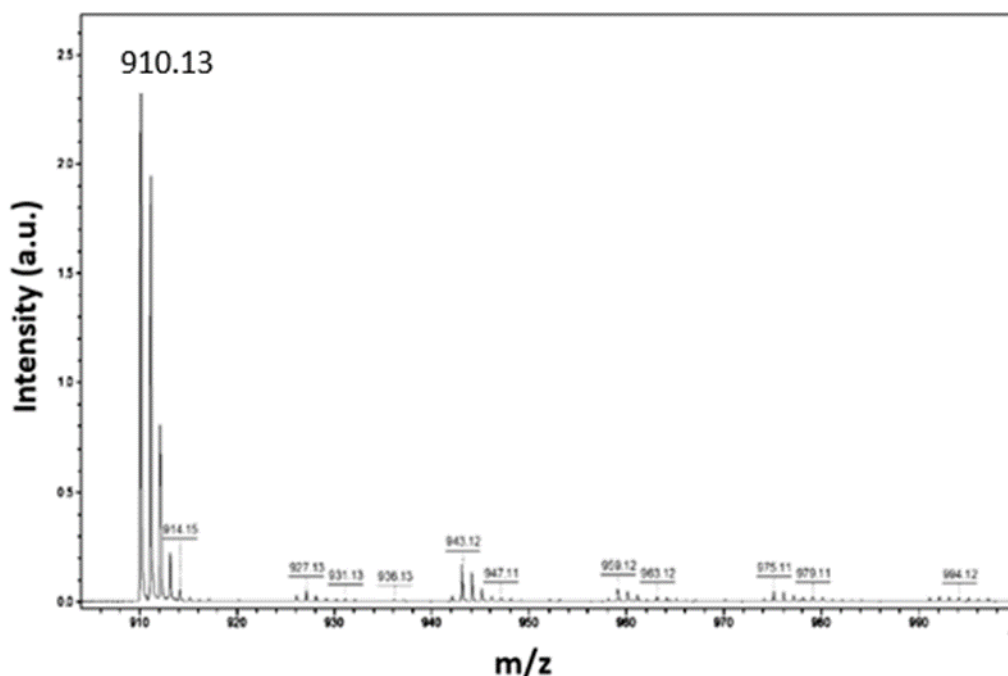


Figure 2.2 MALDI-TOF-MS spectra for the black precipitate from the reaction between tetrakis-DMBI-H and PCBM. Exact mass of PCBM is 910 m/z. The signal at 910 m/z in negative mode of MALDI is consistent with the presence of PCBM^{•-} in the reaction mixture.

Although tetrakis-DMBI-H is able to dope PCBM, the reaction was slow; it took 3d for appreciable precipitate to form. The presence of electron donating groups on the phenyl group of the DMBI-H such as oxygen has been shown to increase the hydride transfer rate since π -donor groups could help the stabilization of charge in the transition state leading to stabilization of the DMBI cations. This was demonstrated by a Hammett study that showed the rate for hydride transfer reaction increased when π -donor groups such as -OMe and -NMe₂ were incorporated into DMBI-H derivatives.⁶²

2.3 Synthesis of tetrakis-O-DMBI-H

The synthesis of DMBI-H derivatives is generally performed in MeOH as it can dissolve the aldehyde starting materials, while the DMBI-H derivatives are generally poorly soluble in MeOH, and thus can be obtained in high yield from the recrystallization from MeOH. CH₂Cl₂ can also be used as solvent since it dissolves both starting materials and the DMBI-H products. The DMBI-H product could then be precipitated by adding MeOH. Unfortunately, some tetra-aldehydes have low solubility in both CH₂Cl₂ and MeOH. Figure 2.3 represents three different tetra-aldehydes that were synthesized and found to have very low solubility in the aforementioned solvents.

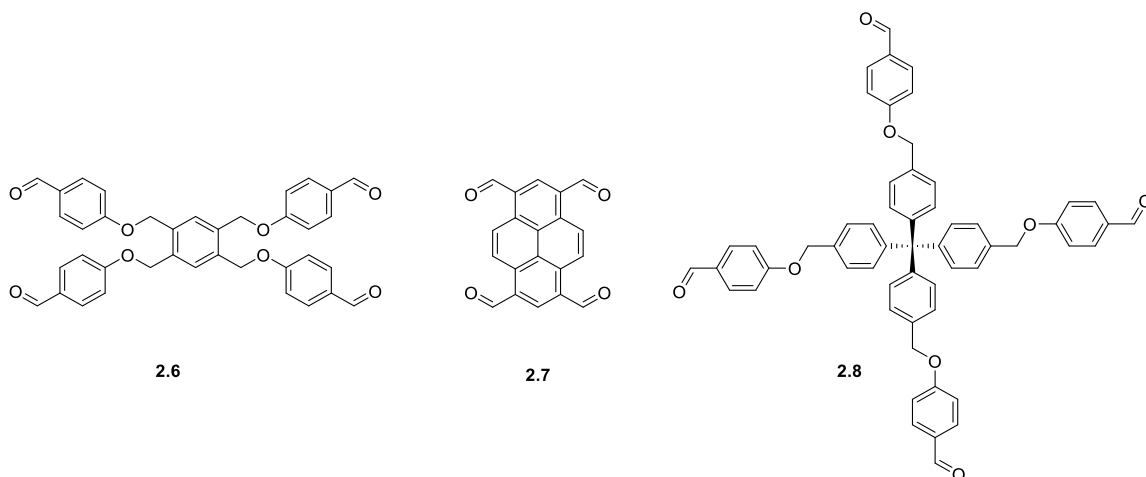


Figure 2.3 Structures of different tetra-aldehydes with low solubility in CH₂Cl₂ or MeOH.

Accordingly, the tetra-aldehyde **2.9** was synthesized and found to have good adequate solubility in CH₂Cl₂ to be used at the concentrations required for the next steps of the synthesis. This tetra-aldehyde also has a flexible structure that can be beneficial for the corresponding tetra-DMBI-H as it has better solubility in solvents including CH₂Cl₂. **2.9**

underwent the reaction with 4.0 equivalents of *N,N'*-dimethyl-1,2-phenylenediamine in CH_2Cl_2 and was purified by recrystallization from MeOH, Figure 2.4.

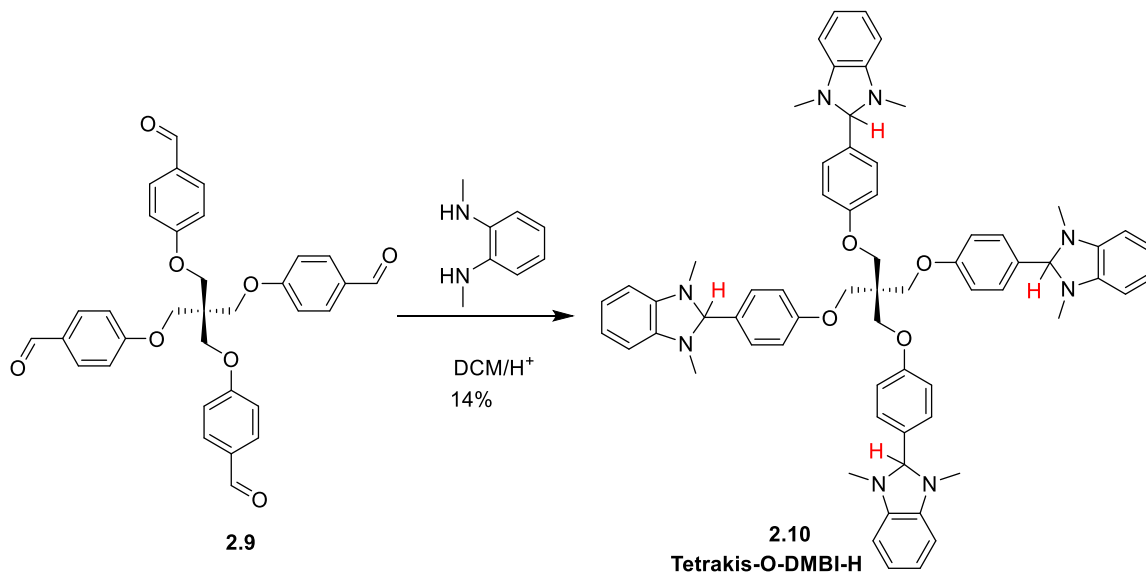


Figure 2.4 Synthesis of tetrakis-O-DMBI-H as a more reactive multiple-hydride donor.

2.3.1 Kinetic studies of tetrakis-O-DMBI-H

Kinetic studies of tetrakis-O-DMBI-H with PCBM showed that the rate of the reaction is higher than those when using tetrakis-DMBI-H; after mixing **2.10** with 4.0 equivalents of PCBM (5.0 mg of tetrakis-O-DMBI-H and 18 mg of PCBM) in *o*-DCB (1.0 mL), precipitation was observed after 2 h. The nature of precipitation was investigated using MALDI, which showed tetrakis-O-DMBI-H is capable of transferring hydrides to PCBM and in negative mode the signal for $\text{PCBM}^{\bullet-}$ was observed (not shown here).

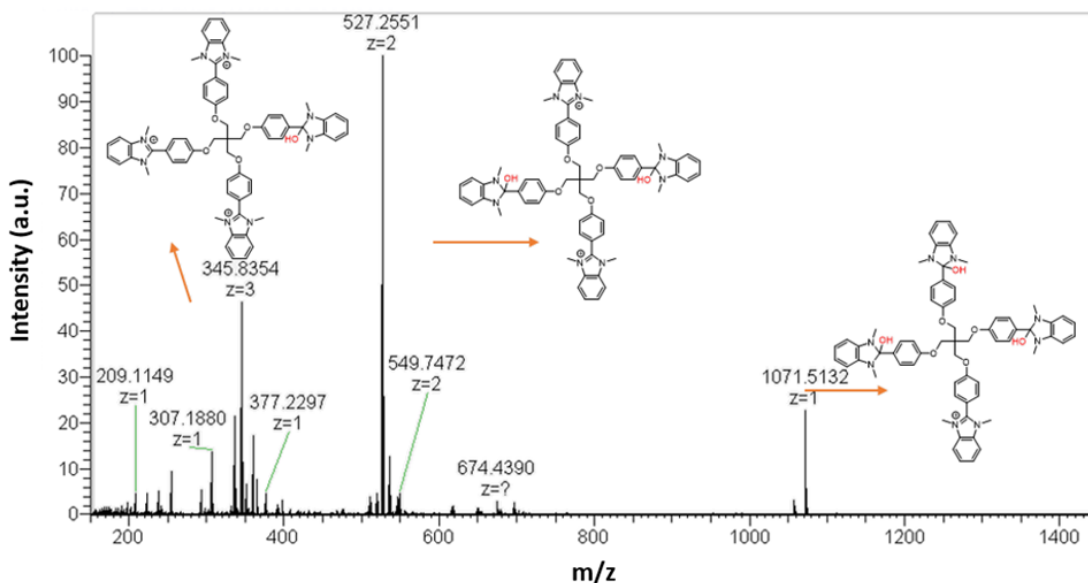


Figure 2.5 ESI spectrum obtained from the reaction product of tetrakis-O-DMBI-H and PCBM (4.0 equivalents).

Moreover, the observed peaks in ESI spectrum are consistent with tetrakis-O-DMBI-H being able to transfer up to 4 hydrides to PCBM and formation of a tetra-cation, which subsequently underwent a reaction with residual water (Figure 2.5). At this stage, the structure of the main product resulting from the addition of water to the cationic center is unclear. The initial product of nucleophilic attack and proton loss is likely the alcohol form shown in Figure 2.6 (left), but this may well isomerize to the amide form, as depicted in Figure 2.6 (right). Amide species of this type are encountered as side products in the synthesis of DMBI dimers by alkali-metal reduction of DMBI⁺ cations, presumably as a result of nucleophilic attack by trace hydroxide followed by isomerization as well as the decomposition products of the dimers on exposure to air.⁶⁹

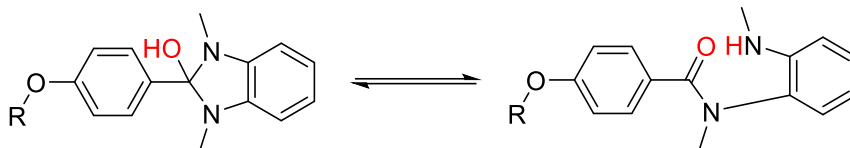


Figure 2.6 The initial product of nucleophilic attack and proton loss is likely the alcohol form (left), but this may well isomerize to the amide form.

2.3.2 Film retention and electrical conductivity studies on tetrakis-*O*-DMBI-*H*-doped PCBM

The electrical conductivity of doped films was evaluated using a 4-point probe in a Van der Pauw configuration. A PCBM film has an in-plane conductivity of $8 \times 10^{-8} \text{ S cm}^{-1}$.⁹² When the tetrakis-*O*-DMBI-*H* (10 mol%, 40 mol% of hydride) was incorporated into the casting solution, the conductivity of PCBM increased to $3 \times 10^{-3} \text{ S cm}^{-1}$ and if the doped film was annealed at 120 °C for 2 h, the conductivity increased to 0.14 S cm^{-1} , consistent with the expected effects of thermal annealing on the rate and extent of the hydride transfer reaction. By increasing the dopant concentration to 20 mol%, the conductivity value decreased to $2 \times 10^{-3} \text{ S cm}^{-1}$ for an annealed film. Atomic force microscopy (AFM) images reveal morphological differences between the films with different doping ratios; smooth surfaces were seen when 10 mol% dopant was used while large nanoaggregates were observed when 20 mol% of tetrakis-*O*-DMBI-*H* was used, Figure 2.7 (d).

Figure 2.7 (b) provides observations that were obtained for solvent resistance studies using UV-vis-NIR. Undoped PCBM films and solutions exhibited no UV-vis-IR absorptions. However, PCBM-doped with tetrakis-*O*-DMBI-*H* exhibited a new, weak and relatively broad band with a maximum absorption at 1020 nm, consistent with the previously reported absorption spectra of PCBM^{•-}.⁶² After submerging the PCBM-doped tetrakis-*O*-DMBI-*H*

film in o-DCB, the absorption intensity of the signals at 1020 and 390 nm decreased in absorption, as the doped film started to dissolve in o-DCB, indicating a low stability of doped film to solvent treatments.

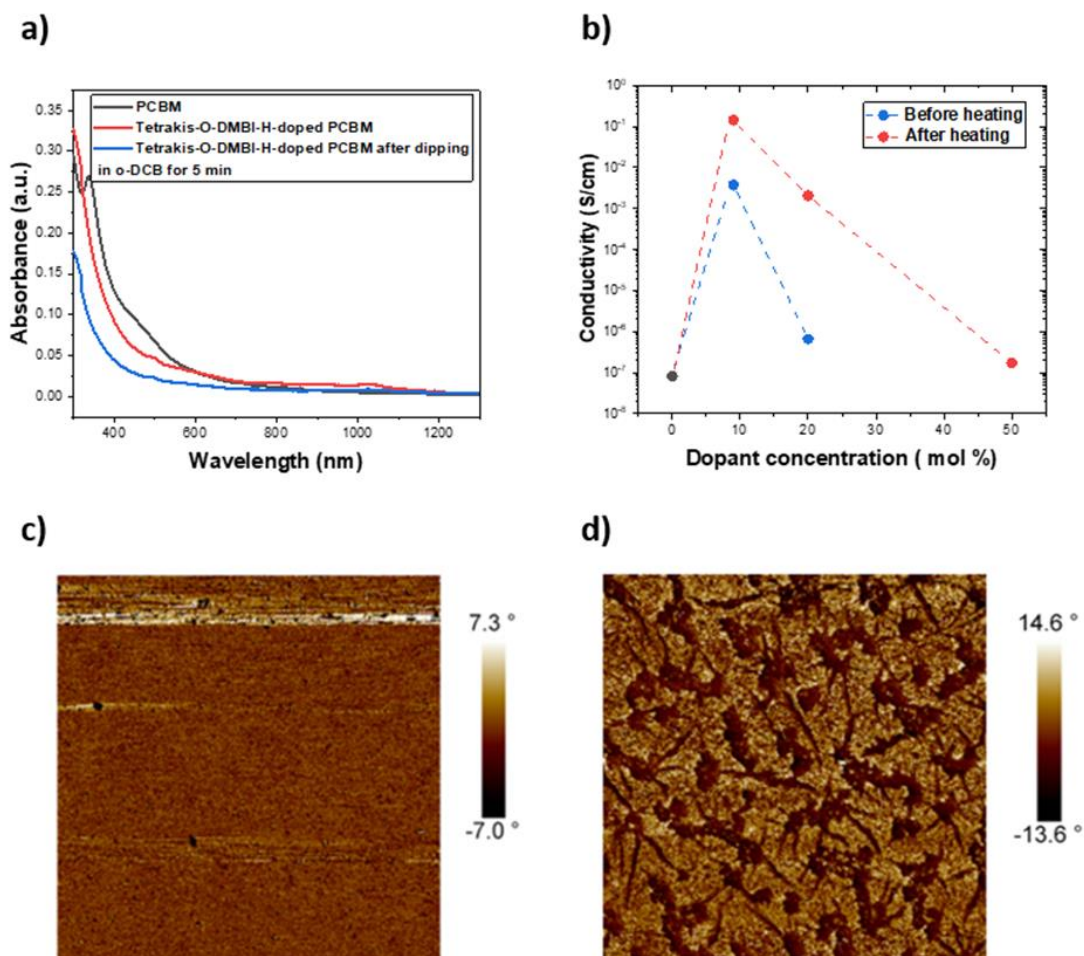


Figure 2.7 a) UV-vis-NIR studies on doped PCBM before and after solvent treatment b) electrical conductivity of tetrakis-O-DMBI-H-doped PCBM (10 mol%) films before and after solvent treatment, c) and d) AFM images on tetrakis-O-DMBI-H-doped PCBM at 10 and 20 mol %.

2.4 Film Retention and Electrical Conductivity Studies on Polymer Doped with Tetrakis-O-DMBI-H

In our first attempt to investigate the film retention on n-type polymer doped *tetrakis-O-DMBI-H*, N2200 ([*N,N'*-bis(2-octyldodecyl)-naphthalene-1,4,5,8-bis(dicarboximide)-2,6-diyl]-alt-5,5'-(2,2'-bithiophene) P(NDI2OD-T2)) was chosen as arguably one of the most widely known and studied electron-transporting D–A copolymer (see Figure 2.8 for chemical structure).⁹³

In the undoped pristine state, N2200 shows the typical absorption features already reported in the literature, which are assigned to an NDI-based π – π^* transition at 390 nm and a broad, low-energy band centered at 705 nm, mainly associated with an intrachain charge transfer between the bithiophene units and the naphthalene dicarboximide moiety. N-doping using tetrakis-O-DMBI-H (25 mol%) is accompanied by a decrease of the intensity of the band 705 nm, along with an increase of an absorption band at roughly 500 nm, consistent with the formation of radical anion species ($\text{NDI}^{\cdot-}$). However, after rinsing the doped film using o-DCB, all doped film was washed away, indicating low film retention ($\sim 0\%$). In general, the conductivity of N2200 doped with DMBIs is in the range of 10^{-4} – 10^{-3} S cm^{-1} . The low conductivity of doped N2200 has been attributed to low doping efficiency because of low dopant/host miscibility and significant steric hindrance, leading to twisted backbone and low electron mobility.^{84, 94}

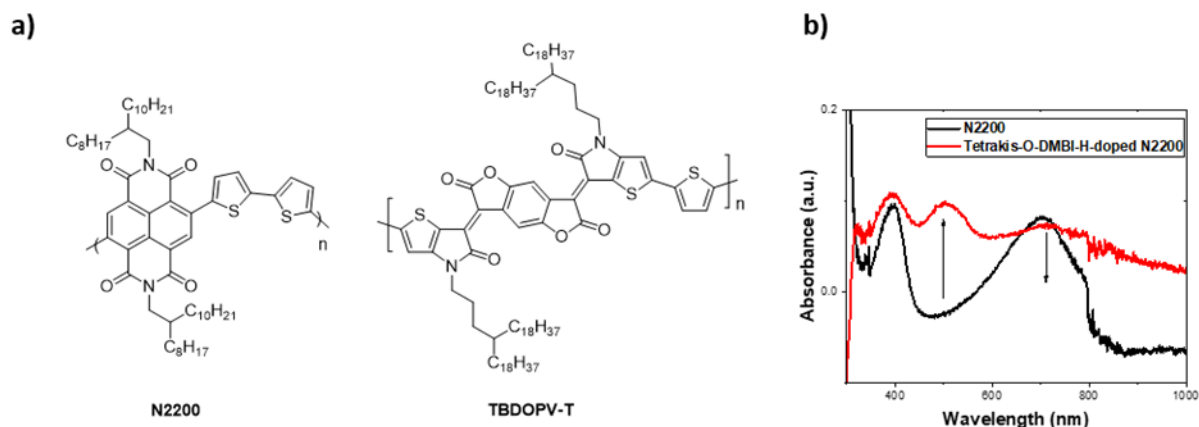


Figure 2.8 Chemical structure on N2200 and TBDOPV-T polymers and UV-vis absorption spectra of pristine N2200 and tetrakis-O-DMBI-H-doped N2200.

In the next step, TBDOPV-T polymer (thiophene-fused benzodifurandione-based oligo(p-phenylenevinylene))-co-thiophene) developed by the Pei group (Figure 2.8) was chosen as the host polymer for subsequent studies. TBDOPV-T has been observed to exhibit a high conductivity (60 S cm^{-1}) when it n-doped with N-DMBI-H dopant (24 mol%). This high conductivity was attributed to the rigid planar backbone (thiophene-fused benzodifurandione-based oligo(p-phenylenevinylene)) of the polymers and excellent miscibility with the dopant molecules.⁹⁴

2.4.1 Film retention and electrical conductivity studies on TBDOPV-T-doped tetrakis-O-DMBI-H

Doped films were prepared by co-deposition of a solution of the polymer and tetrakis-O-DMBI-H by spin-coating and annealing at 140°C for 2.5 h. UV-vis-NIR absorption spectroscopy (Figure 2.9) indicates that the main NIR absorption band of neutral TBDOPV-T polymer was bleached when it was doped using tetrakis-O-DMBI-H with new feature extending deep into the NIR, which is attributed to negatively charged TBDOPV-

T polymer, consistent with the literature report.⁹⁴ Submerging the doped film in o-DCB for 5 and 10 min did not lead to any significant decrease in the intensity of the signal corresponded to negatively charged TBDOPV-T polymer. The film retention was calculated to be about 93%.

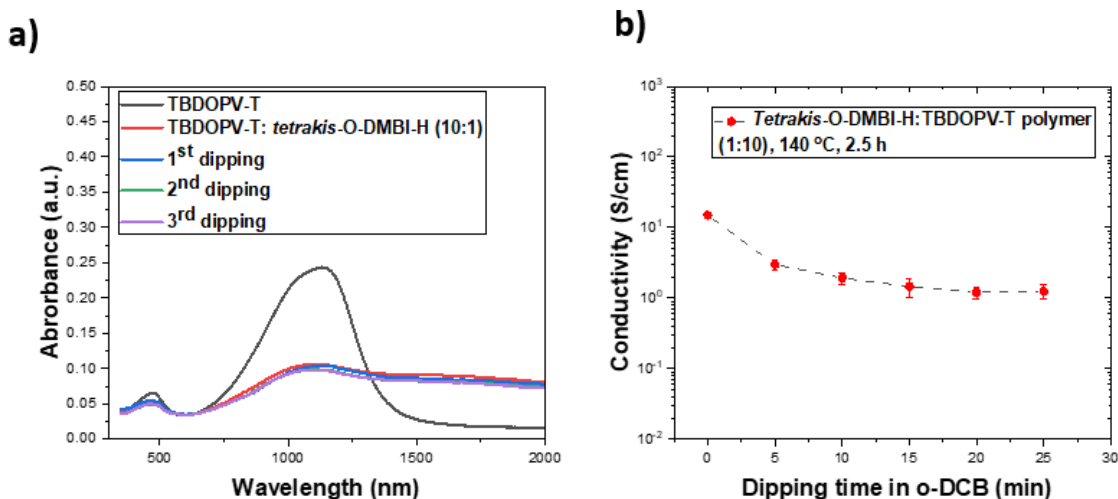


Figure 2.9 a) Optical absorption spectra of undoped and tetrakis-O-DMBI-H -doped TBDOPV-T films before and after immersing into o-DCB for 5 min. b) Electrical conductivity of tetrakis-O-DMBI-H -doped TBDOPV-T films before and after dipping in o-DCB.

The conductivity of tetrakis-O-DMBI-H -doped TBDOPV-T films was measured as a function of dipping time, as shown in Figure 2.9 (b). Upon optimizing the tetrakis-O-DMBI-H concentration (10 mol% dopant, 40 mol% hydride), the film showed a conductivity value of 15 S cm⁻¹. Since the conductance of the pristine TBDOPV-T film was too low to provide a reliable signal, a reference value of 1×10⁻⁸ S cm⁻¹ (being the detection limit of the used device) was taken as the upper limit. Next, the doped film was immersed into o-DCB for 5 min, which led to a drop in conductivity to 3 S cm⁻¹. Upon the second dipping step, the conductivity remained constant within the range of uncertainty, which was consistent with optical absorption data, Figure 2.9 (a). It is reasonable to assume

that some solvent molecules are able to diffuse into the film when it was dipped in o-DCB. Although the films were dried under a stream of nitrogen, we speculate that residual solvent molecules may affect the film microstructure and leading to the observed decrease in conductivity.

2.4.2 *Ultraviolet photoelectron spectroscopy (UPS)*

Ultraviolet photoelectron spectroscopy (UPS) was used to investigate the changes of the electronic properties of TBDOPV-T with the tetrakis-O-DMBI-H, Figure 2.10. Upon doping, a strong decrease in sample work function by 0.6 eV was observed. Furthermore, the valence band shifts to higher binding energy upon doping, due to the shift of Fermi level toward the conduction band. Simultaneously, a new feature close to the Fermi level appears. The change in the electronic structure of a conjugated polymer upon addition of an electron is commonly explained in the model of a localized negative polaron. In this model, a new singly occupied state on a polymer segment is formed and is at lower energy than the conduction band (CB) minimum of the surrounding neutral polymer. A second, doubly occupied, new state is considered as being formed above the valence band (VB) maximum of the neutral polymer.⁹⁵ Within the framework of the simple polaron model, the low-binding-energy feature observed here corresponds to the partially filled sub-level, located within the semiconductor gap, and represents a clear manifestation of n-type doping.

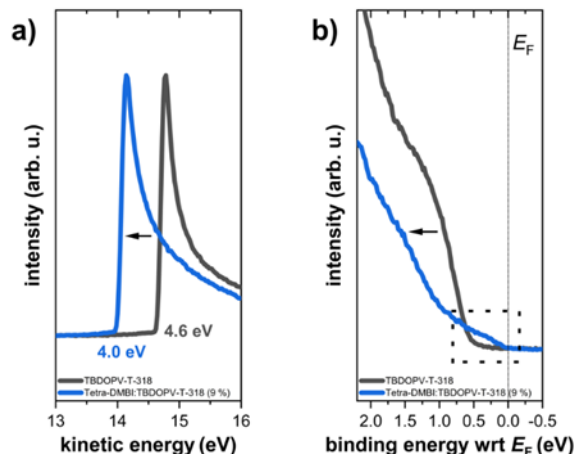


Figure 2.10 UPS a) secondary electron cut off (SECO) and b) valence band spectra with respect to the Fermi level E_F of pristine (gray) and tetrakis-O-DMBI-H-doped TBDOVP-T (blue) films. The numbers next to the SECO spectra give the work function of the measured samples. Note that in (b) the main VB onset in the doped film is seen at higher binding energy than in the pristine material, but that there is also a new feature at low binding energy (indicated by dotted box).

2.5 Diffusion Studies on Tetrakis-O-DMBI-H-doped TBDOVP-T Films

The remarkable stability of tetrakis-O-DMBI-H-doped TBDOVP-T films to solvent treatment, presumably as a result of multiple electrostatic interaction between dopants ions and polymer, might also lead to a suppressed diffusion of the dopant ions or dopant molecules. In the next step the stability of the doped film was studied at elevated temperatures. To do so, the doped polymer film was annealed at 140 °C for 5 h on a hot plate in an inert atmosphere. Negligible changes in intensity upon annealing was observed.

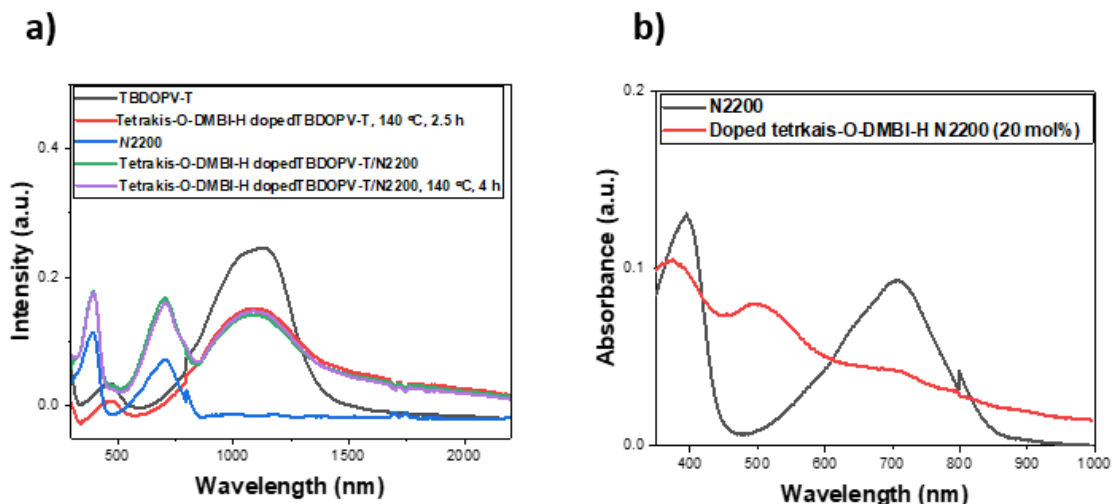


Figure 2.11 Optical absorption spectra of (a) tetrakis-O-DMBI-H-doped TBDOPV, and sequentially deposited N2200 on tetrakis-O-DMBI-H-doped TBDOPV films before and after heating, (b) N2200 and sequentially tetrakis-O-DMBI-H-doped N2200.

To gain some insights into the diffusion of molecular dopants/ions, N2200 polymer was sequentially deposited on a tetrakis-O-DMBI-H doped TBDOPV-T film (10 mol%). The film was heated at 140 °C for 4 h in an inert atmosphere. The reduction potentials of N2200 and TBDOPV-T polymers are both ca. -1.0 V vs. ferrocene,^{94, 96} therefore, no energetic penalty is expected for dopant and charge-carrier migration from TBDOPV-T into the N2200. In case of dopant migration, one would expect to observe a polaron feature of N2200 around 500 nm and a decrease in features associated with the doped tetrakis-O-DMBI-H doped TBDOPV-T material.

As it can be seen from Figure 2.11 (a), there is no sign or increase in the intensity ~ 500 nm, or a decrease in the intensity of the signal corresponded to negatively charged TBDOPV-T polymer. Thus, under this condition, no sign of diffusion of dopant for tetrakis-O-DMBI-H was observed.

Moreover, a control experiment was conducted to assure N2200 can sequentially be doped by tetrakis-O-DMBI-H, Figure 2.11 (b), as some dopants reported to fail to sequentially dope N2200.⁹⁷ As it can be seen, after sequential doping of N2200 with tetrakis-O-DMBI-H (20 mol%) and heating at 140 °C for 2h , the polaron signal appears.

2.5.1 *Grazing-incidence wide-angle X-ray scattering (GIWAXS)*

To gain an insight into how the molecular dopants and/or counterions affect the polymer packing, and, therefore, influence the charge-transport properties, a series of GIWAXS data was acquired for TBDOPV-T polymer with different dopant concentrations, Figure 2.12 (a). The doping of TBDOPV-T, in common with many other previously studied systems, induces increased structural disorder, particularly at high dopant ratio.⁹⁸ Here, reflections from lamellar and π - π stacking are denoted as (100) and (010), respectively. Neat TBDOPV-T shows well resolved (100) and (010) reflections in both in-plane and out-of-plane directions suggesting the presence of face-on and edge-on crystallite populations. In the following discussion, changes in the d-spacing of the (100) and (010) peaks are used to track changes in the packing of TBDOPV-T. Neat TBDOPV-T exhibits a lamellar packing with a d-spacing of 34.6 Å, and π - π stacking with a d-spacing of 3.39 Å. Overall, a systematic increase of (100) and (010) d-spacings with increasing dopant fractions was observed. Specifically, an increased (100) d-spacing of 36.0 Å and a π - π stacking distance of 3.45 Å for a dopant fraction 10 mol %. With increasing dopant fraction, we observe reduced scattering intensity and an increased width for the (100) peak. Higher orders of the lamellar peak are only observed for the neat polymer and rapidly vanish with increasing dopant fractions. Furthermore, the (010) peak vanishes at 33 mol% or higher dopant fraction, Figure 2.12 (b and c). These results indicate that the tetrakis-O-DMBI-H cations

significantly interfere with the polymer packing. To quantify the effects of the dopant concentration on polymer crystallinity and texture in TBDOPV-T, pole-figure⁹⁹ and approximate relative degree of crystallinity (rDoC) analysis of the polymer scattering patterns were performed for the (100) peak, Figure 2.12 (d). The polar angle χ describes the relative orientation of crystallites with respect to the substrate, with the $\chi = 0^\circ$ and 90° orientations of the (100) peak representing edge-on and face-on orientation of crystallites, respectively. The background corrected and normalized scattering intensities of the (100) peaks were integrated over $\chi = [-80^\circ, 80^\circ]$, and the total integrated areas are compared between samples of TBDOPV-T with different loading of tetra-DMBI, yielding their respective approximate rDoC. The rDoC analysis of (100) peaks for TBDOPV-T shows that polymer crystallinity is reduced with increasing the concentration of dopant, particularly for 23 and 33 mol%. This means that the lamellar packing of the polymer becomes increasingly disordered with increased doping. Additionally, with increased concentration of tetrakis-O-DMBI-H, the predominantly face-on orientation is diminished, with both face-on and edge-on populations evident from the relative increase of scattering intensity around $\chi = [-30^\circ, 30^\circ]$ in the relevant pole figure. This drastic changes to the packing of TBDOPV-T with increasing dopant fractions can be rationalized by the large 3D size of tetrakis-O-DMBI-H species inducing significant structural disorder and reduced polymer crystallinity.

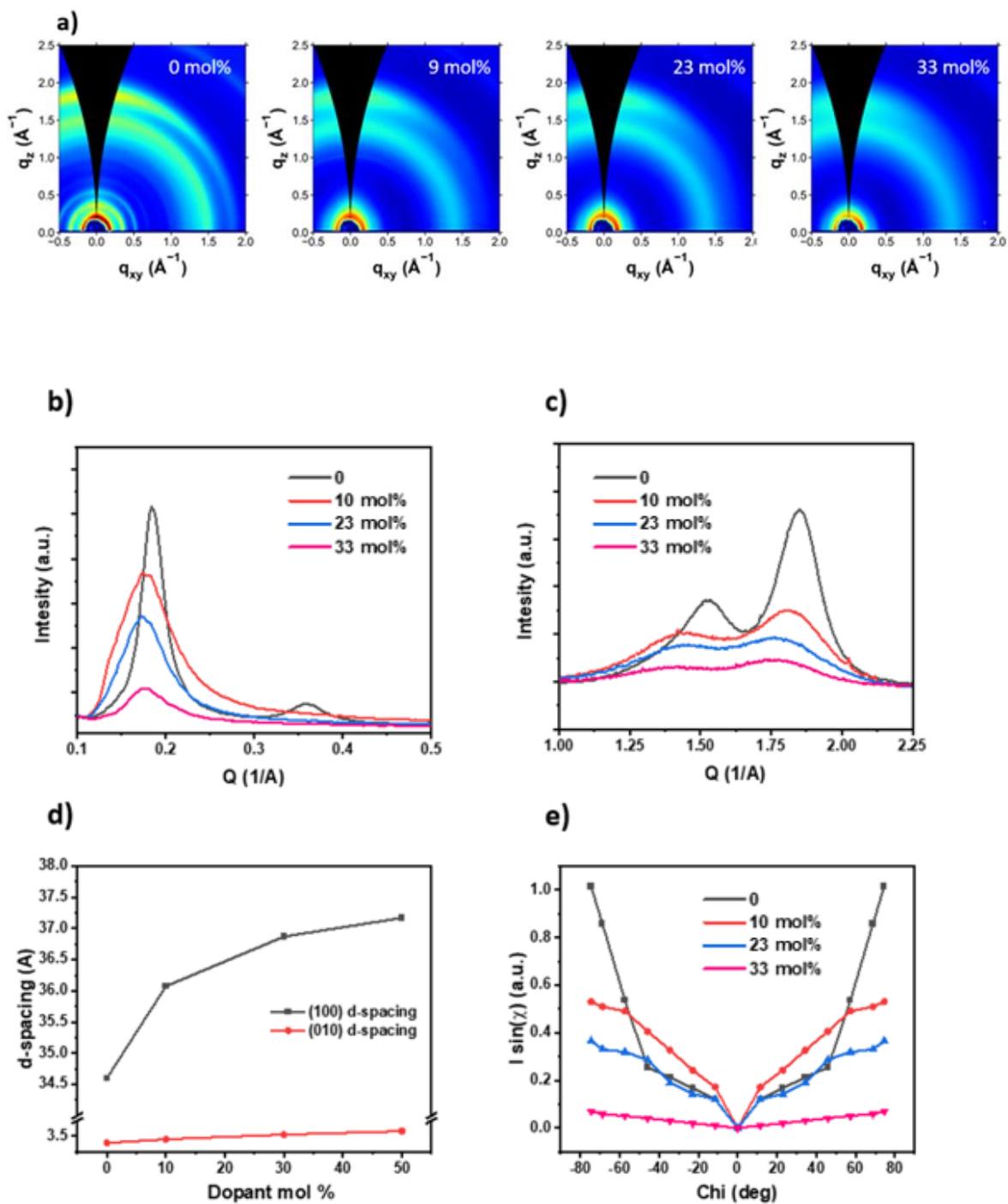


Figure 2.12 a) GIWAXS patterns of pristine TBDOPV-T and doped TBDOPV-T with different mol ratios of tetrakis-O-DMBI-H. b) 1D-GIWAXS linecuts of TBDOPV-T at

different dopant ratios (in-plane direction), c) 1D-GIWAXS linecuts of TBDOPV-T at different dopant ratios (out-of-plane direction), d) lamellar distances, and e) relative degrees of crystallinity (rDoC).

2.6 Summary and Conclusion

Two dopants (tetrakis-DMBI-H and tetrakis-O-DMBI-H) have been synthesized in which 4 units of DMBI-H units are linked together via an sp^3 carbon. Due to the presence of electron donating groups, oxygens, in para position of the 2-phenyl groups in each DMBI-H unit, tetrakis-O-DMBI-H is the more reactive hydride donor. Tetrakis-O-DMBI-H could dope PCBM, transfer up to 4 hydrides and form a tetra-cation. Incorporation of 10 mol% of dopant with PCBM resulted in a conductivity of 0.14 S cm^{-1} , however the doped film showed very low resistance to solvents, as is very common for doped small-molecule semiconductors.

The, tetrakis-O-DMBI-H was able to dope polymers; including N2200 and PBTOPV-T. Although, the N2200 films showed very low resistance toward solvent treatment, tetrakis-O-DMBI-H-doped-PBTOPV-T film exhibited remarkable solvent resistance.

Electrical conductivity measurements on tetrakis-O-DMBI-H-doped-TBDOPV-T revealed a conductivity value of 15 S cm^{-1} , using 10 mol% of the dopant. The doped films also were characterized using UPS and a significant decrease in sample work function was observed. Furthermore, the valence band shifts to higher binding energy upon doping which is related to an increase in electron density near the Fermi level.

The diffusion of dopant molecules/ions in doped films have also been examined; by sequential depositing of N2200 on the top of tetrakis-O-DMBI-H-doped-PBTOPV-T film

and heating the film at 120 °C for 4 h. Negligible changes in intensity of the signal corresponded to negatively charged TBDOPV-T polymer upon annealing was observed.

At this stage, there is no mechanistic data, confirming the formation of tetra-cations when TBDOPV-T was doped using tetrakis-O-DMBI-H, although based on the rapid reactivity of other DMBI and DOPV-type polymers and the large Fermi-level shifts encountered in this work, one would expect formation of some multiple-charged species. Nevertheless, the preliminary diffusion data is promising, indicating that, indeed, the multiple electrostatic interactions between the dopant ions and ionized polymer segments, to a large extent, could lead to dopant immobilization in solid state.

2.7 Experimental Details

2.7.1 Synthesis

Chemicals were obtained from commercial sources and used as received unless stated otherwise. TBDOPV-T polymer was synthesized following reported procedures.⁹⁴ N2200 polymer was purchased from Polyera (Lot: CZH-XV-77-22). All operations involved in synthesis were performed under an atmosphere of nitrogen using standard Schlenk techniques or in a glove box. ¹H-NMR and ¹³C-NMR spectra were recorded in CDCl₃ or C₆D₆, on Varian 500 or 700 MHz spectrometers. The chemical shifts (δ) are reported in parts per million (ppm).

Synthesis of tetra(4-bromophenyl) methane (2.2)

As per the reported procedure,¹⁰⁰ bromine (8.0 mL, 156 mmol) was added slowly to tetraphenylmethane (5.0 g, 14.4 mmol) with continuous stirring. The resulting slurry was

stirred for an additional 5 h and then poured into ethanol (400 mL), which was cooled to -78 °C. The precipitated solid was filtered, washed with saturated aqueous NaHSO₃ solution (100 × 3 mL) and dried at 50 °C under vacuum to give a pale yellow solid (6.0 g, 9.5 mmol, 60%). ¹H NMR data were consistent with the literature.

Synthesis of 4,4',4'',4'''-methanetetrayltetrabenzaldehyde (2.3)

As per the reported procedure,⁹¹ a solution of tetra(4-bromophenyl) methane (5.07 g, 8.0 mmol) in THF (300.0 mL) was stirred at -78 °C under nitrogen and treated dropwise with a solution of n-butyllithium (28 mL, 2.5 M in hexane, 70.0 mmol). The resulting mixture was kept at -78 °C for 30 min, and then DMF (10 mL, 128.0 mmol) was added dropwise. The mixture was stirred 12 h, while the temperature was allowed to rise to 25 °C. To the solution was added 1.0 M aqueous HCl (20.0 mL), and solvent evaporated under reduced pressure. The remaining aqueous concentrate was extracted with EtOAc, and the combined organic extracts dried over Na₂SO₄, and filtered. The solvent was removed by evaporation under reduced pressure, and the residue was recrystallized from EtOAc to yield a white solid (0.90 g, 2.0 mmol, 28%). ¹H NMR data were consistent with the literature.

Synthesis of tetrakis(4-(1,3-dimethyl-2,3-dihydro-1*H*-benzo[*d*]imidazol-2-yl)phenyl)methane (2.5)

4,4',4'',4'''-Methanetetrayltetrabenzaldehyde (238 mg, 0.550 mmol) was dissolved in 2.0 mL CH₂Cl₂ and 3.0 mL MeOH. To this solution, *N,N'*-dimethyl-1,2-phenylenediamine (300 mg, 0.220 mmol) in 1.0 mL methanol was added. While stirring, a drop of glacial acetic acid was added. After 45 min, the precipitate was separated from the reaction mixture by filtration, and then washed with cold methanol. The yellow solid was dissolved in

CH₂Cl₂ and recrystallized from methanol to yield a yellow solid (200 mg, 0.220 mmol, 40%). ¹H NMR (400 MHz, CDCl₃) δ 7.53-7.43 (m, 8H), 7.31–7.23 (m, 8H), 6.77-6.69 (m, 8H), 6.47-6.49 (m, 8H), 4.91 (s, 4H), 2.64 (s, 24H).

Synthesis of tetrakis[(4-formylphenoxy)methyl]methane (2.9)

As per the reported procedure,¹⁰¹ pentaerythrityl tetrabromide (5.0 g, 12.8 mmol), 4-hydroxybenzaldehyde (7.9 g, 65 mmol), KOH (3.6 g, 65 mmol), and tetrabutylammonium iodide (40 mg, 0.11 mmol) were added to a two-neck flask. A reflux condenser was installed, and the flask evacuated, refilled with nitrogen three times. DMF (40 mL) was added and the mixture was stirred at 120 °C for 12 h. The reaction mixture was cooled to room temperature and poured into water. The crude product was extracted with EtOAc, and washed with saturated brine, dried over sodium sulfate, and the solvents were evaporated to afford a yellow solid to which methanol (30 mL) was added. The solids were filtered and rinsed with methanol again to get yellow shiny crystals (4.0 g, 7.23 mmol, 56%). ¹H NMR (500 MHz, CDCl₃) δ 9.89 (s, 4H), 7.83 (d, *J* = 8.8 Hz, 8H), 7.05 (d, *J* = 8.8 Hz, 8H), 4.48 (s, 8H). ¹³C{¹H} NMR (176 MHz, CDCl₃) δ 190.78, 163.27, 132.13, 130.73, 114.98, 66.58, 44.82. HRMS (ESI) calcd for C₃₃H₂₉O₈ (M+H⁺), 553.1856; found 553.1850.

Synthesis of tetrakis[(4-(1,3-dimethyl-2,3-dihydro-1*H*-benzo[*d*]imidazol-2-yl)phenoxy)methyl]methane (tetrakis-O-DMBI-H, 2.10)

In a glove box, Compound 2.9 (2.0 g, 3.6 mmol) was dissolved in anhydrous CH₂Cl₂ (20 mL). *N,N'*-dimethyl-1,2-phenylenediamine (2.0 g, 14.68 mmol) was dissolved in 5.0 mL CH₂Cl₂ and added to reaction flask, which then was sealed with a septum and transferred

outside the glove box. Three drops of acetic acid were added by a syringe. The mixture was stirred at room temperature overnight. To the mixture, methanol was added, which results in white precipitate. The solid was filtered and dissolved in CH₂Cl₂ and precipitated with methanol to obtain off-white solid (this process was repeated three times) (500 mg, 14%). ¹H NMR (700 MHz, C₆D₆) δ 7.42 (d, *J* = 8.6 Hz, 8H), 6.93 – 6.84 (m, 16H), 6.41 (dd, *J* = 5.4, 3.2 Hz, 8H), 4.60 (s, 4H), 4.37 (s, 8H), 2.31 (s, 24H). ¹³C{¹H} NMR (176 MHz, C₆D₆) δ 160.12, 142.62, 132.58, 130.63, 119.98, 114.92, 106.28, 94.11, 67.11, 45.16, 33.05. ESI-MS = (1027.5 [M+3H]⁺, 4.0%), 1026.5 [M+2H]⁺, 7.9%, 1025.5 [M+H]⁺, 0.2%), 1023.5 [M-H]⁺. HRMS (ESI) calcd for [M-H]⁺, 1023.5280; found 1023.5277. Anal Calcd. For C₆₅H₆₈N₈O₄: C, 76.14; H, 6.69; N, 10.93, Found C, 75.29; H, 6.63.43; N, 10.56.

2.7.2 Characterizations: general procedures and experimental details

Stock solutions with concentrations of 5 mg/ml for tetrakis-O-DMBI-H and TBDOPV-T were prepared under nitrogen atmosphere in an inert gas box using dried 1,2-dichlorobenzene (o-DCB). The stock solutions were stirred overnight in order to enable complete dissolution of the materials. The reported dopant concentration of 9 mol% is given as $c = \frac{N_D}{N_D + N_P}$, where N_D is the number of dopant molecules and N_P is the number of polymer monomer units as contained in the solutions. Thin films were prepared via spin-coating. Therefore, a standard laboratory spin-coater was used at 1000 rpm for 1 min, followed by 2000 rpm for 20 sec. Thermal activation was performed by annealing the 9 mol%-doped thin films at 140 °C for 2.5 h on a hot plate in the glovebox, if not otherwise stated.

Optical absorption spectroscopy was performed using a Lambda 950 UV-vis-NIR spectrophotometer (PerkinElmer, Inc.). Undoped and doped thin films were prepared on glass substrates with thickness between 5 and 20 nm.

Conductivity measurements were performed inside a nitrogen-filled glovebox. The samples were prepared by spin-coating the undoped and tetrakis-O-DMBI-H-doped TBDOPV-T films on glass substrates. The sheet resistance was measured by using an in-line four-point probe with 0.635 mm tip spacing, connected to a resistivity test unit (RM3000) from Jandel Engineering. Resistivity values were calculated by multiplying the film's sheet resistance by the film thickness, which was measured with a Dektak profilometer. The conductivity was obtained by taking the inverse of the resistivity.

Ultraviolet photoelectron spectroscopy (UPS) and X-ray photoelectron spectroscopy (XPS) measurements of thin films on ITO substrates were performed in an ultrahigh vacuum chamber with a base pressure of 10^{-9} mbar. UPS measurements were performed at a SPECS UHV system, equipped with a monochromated helium-gas-discharge lamp (21.22 eV). For XPS measurements, non-monochromated Al K α (1486.7 eV) radiation was used for excitation. The spectra were collected in normal emission by using an Omicron EA125 hemispherical electron energy analyzer. A pass energy of 5 eV and 20 eV was used for UPS and XPS measurements, respectively. The secondary electron cutoff (SECO) spectra were measured with a bias of -10 V, which was applied to the sample in order to clear the analyzer work function.

The film surface topography was characterized with a Bruker Dimension Icon scanning force system, operated in Peak Force Tapping TM mode using ScanAsyst-Air cantilevers.

Grazing incidence wide angle X-ray scattering (GIWAXS) measurements were performed at the Stanford Synchrotron Radiation Lightsource (SSRL) beamline 11–3 with an X-ray wavelength of 0.9752 Å and sample-to-detector distance of 321 mm at an incident angle of 0.14°. Measurements were carried out using a helium-filled sample chamber to reduce air scattering background. The 2DGIWAXS patterns were collected with a 2D CCD X-ray detector (MX225, Rayonix, L.L.C) with a pixel size of 73.2 μm (3072 × 3072 pixels).

CHAPTER 3: IMMOBILIZATION VIA CHEMICAL BOND FORMATION: AN APPROACH TO RESTRICT THE DIFFUSION RATE OF N-TYPE DOPANTS

This project was accomplished in collaboration with:

- Marder group, Georgia Tech (Farzaneh Saeedifard, Stephen Barlow, Seth Marder),

Synthesis and characterization of dopants

The content of this chapter is unpublished.

3.1 Introduction

As it was discussed in Chapter 2, creating multiple electrostatic interactions between DMBI cations and doped acceptors is a promising strategy for decreasing the diffusion rate of DMBI cation. Another approach to decrease diffusion of DMBI-H derivatives and the corresponding DMBI cations is using covalently crosslinkable materials. Advantages of applying crosslinkable materials are that: 1) covalent linking of molecular components to form polymer matrices and densification to reduce diffusion through free volume; 2) even moderate crosslinking densities are usually sufficient to render polymers highly insoluble. This second aspect could be useful for multilayer device fabrication from solution.

Some of the well-developed methodologies involve using cross-linkable groups such as siloxanes, styrenes, acrylates, benzocyclobutenes, cinnamates, chalcones, oxetanes, or using “click chemistry” such as the reactions between alkynes and azides.¹⁰²⁻¹⁰⁵ Most of the aforementioned functional groups have been utilized successfully in the general field of polymer chemistry, but approaches have been less explored for immobilizing electrical dopants.

The focus of this chapter is on the exploration of the use of crosslinkable functional groups for DMBI-H n-dopants. One important design consideration is the ease of synthesis, as it is desirable for the functional group to be easily incorporated into the dopants/cations, and not interfere with the dopant chemistry in the devices. As benzocyclobutenes are not readily reducible, they are expected to be suitable for the crosslinking of DMBI-H dopants without to a first approximation interfering with dopant chemistry. Benzocyclobutene or bicycle[4.2.0]octa-1,3,5-triene (BCB), has been widely studied in the field of polymer

science as a thermo-crosslinking agent, owing to its ability to crosslink by ring opening the strained cyclobutene ring.¹⁰⁶⁻¹¹⁰

Figure 3.1 shows the ring opening of the benzocyclobutene at elevated temperatures. The crosslinking reaction of BCB proceeds by application of thermal energy, which results in the strained cyclobutene moiety undergoing an electrocyclic ring opening rearrangement to form a highly reactive o-xylylene intermediate. This intermediate can then undergo a cycloaddition reaction with unsaturated functionalities, such as vinyl units to afford a tetrahydronaphthalene linkage, or with another o-xylylene unit by converting the π -bonds at the termini of the acyclic conjugated π -system to σ bonds, to yield the reactive spiro-dimer intermediate that can rearrange to the energetically lower 1,2,5,6-dibenzocyclooctadiene linkage.^{106, 110, 111}

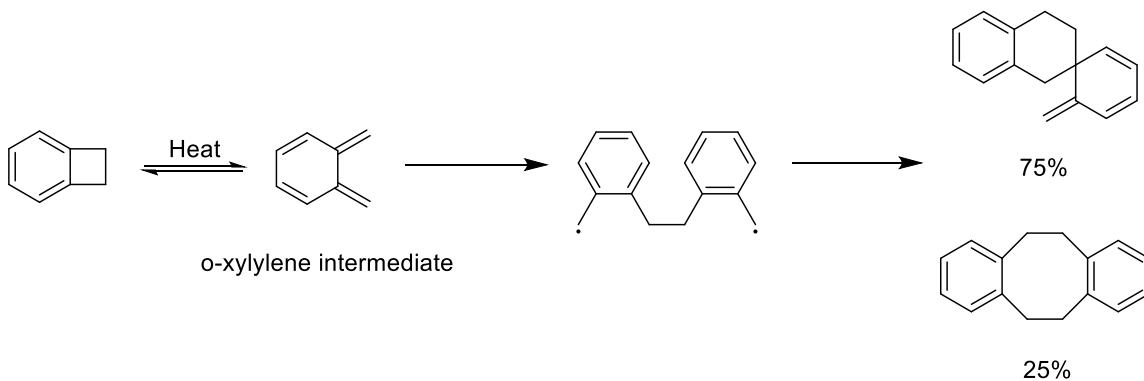


Figure 3.1 Ring opening of benzocyclobutene to form the cross-linked product.

3.2 Design and Synthesis of the Thermo-crosslinkable DMBI-H

One key drawback of BCBs linked to other moieties through alkyl bridges, however, is that their cross-linking reaction necessitates temperatures of over 240 °C,^{110, 112} which might be unsuitable for thermal stability of DMBI units and also potentially limits the compatibility of the approach with certain substrates. It has been reported that the introduction of electron donating alkoxy groups to the cyclobutene ring of the BCB moiety can significantly lower the temperature at which the electrocyclic ring opening reaction responsible for cross-linking takes place.^{97, 113, 114} Therefore, it was decided to synthesize a DMBI cation unit attached to BCB with an oxygen bridge and test the thermal stability of the cation at the condition required for crosslinking, Figure 3.2 represents the synthetic scheme that was employed. The dopant can then potentially be covalently bound to semiconductors matrices that contain the same BCB units, which may also lead to crosslinking of the matrices on heating.

3.2.1 Synthesis of the cation

The DMBI-containing benzocyclobutene derivative was synthesized from bicyclo[4.2.0]octa-1,3,5-trien-7-ol, **3.1**, which was synthesized according to the published procedure.¹¹⁵

Compound 4-(bicyclo[4.2.0]octa-1,3,5-trien-7-yloxy)benzaldehyde, **3.2**, was synthesized from **3.1** by a Mitsunobu reaction from 4-hydroxybenzaldehyde in 64% yield, as shown in Figure 3.2. In the next the step, 2-(4-(bicyclo[4.2.0]octa-1,3,5-trien-7-yloxy)phenyl)-1*H*-benzo[*d*]imidazole was synthesized from the reaction of **3.2** and 1,2-phenylenediamine in the presence of Na₂S₂O₅. Cation **3.4** was synthesized from the reaction of **3.3** and methyl

iodide followed by anion exchange reaction with tetrabutylammonium hexafluorophosphate in MeOH to give the desired product as off-white solid.¹¹⁶

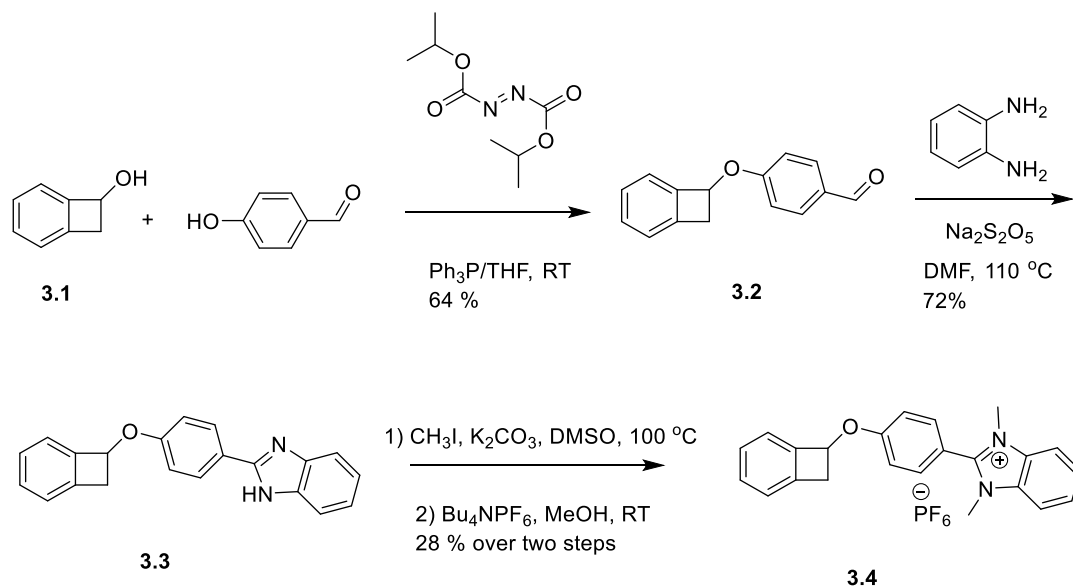


Figure 3.2 Synthetic route for the synthesis of BCB-DMBI cation.

3.2.2 Thermal stability experiments of 2-(4-(bicyclo[4.2.0]octa-1,3,5-trien-7-yloxy)phenyl)-1,3-dimethyl-1H-3H-benzo[d]imidazole (compound 3.4)

To test the thermal stability DMBI-cation, **3.4**, a solution containing 2.0 mg of **3.4** and 16.0 mg of **3.2** was dissolved in CH₃CN (1.0 mL) and drop-cast on a glass substrate. After drying in air, the film was heated at 205 °C for 15 min to initiate the crosslinking condition. The composition of the annealed film was investigated by mass spectrometry (MALDI-TOF-MS), which identified a peak at 565 m/z, consistent with the expected asymmetric dimerization product. However, there are other peaks at 443 and 667.83 m/z that are as a result of decomposition of the desired product and further side reactions, Figure 3.3.¹¹⁷

It was speculated that thermal heating product of the alkoxy-substituted BCB-based moiety (Figure 3.4 compound **A**) underwent an elimination reaction to produce alkene-containing species as side product (compound **B**). Compound **B** reacted with another reactive intermediate and generated compound **C**, however, we can exclude the possibility that this side reaction occurs during acquisition of the mass spectral data. This analysis (Figure 3.4) is consistent with the signals appeared from MALDI-TOF-MS spectrum.

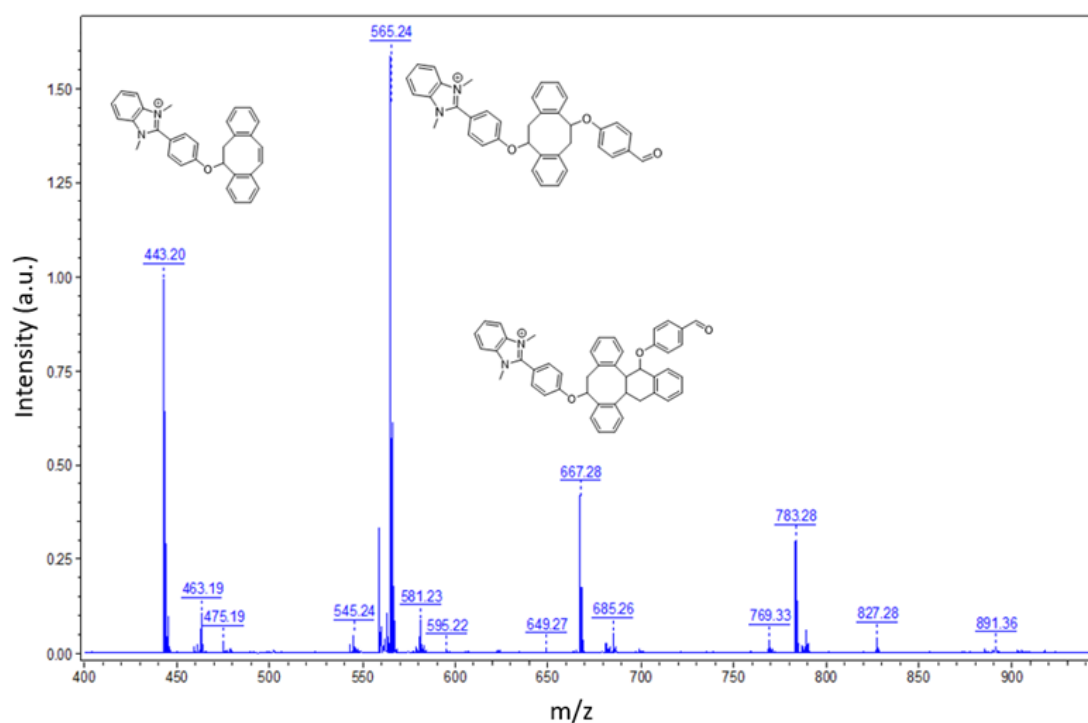


Figure 3.3 MALDI-TOF-MS spectrum from the reaction products of compound 3.2 and 3.3.

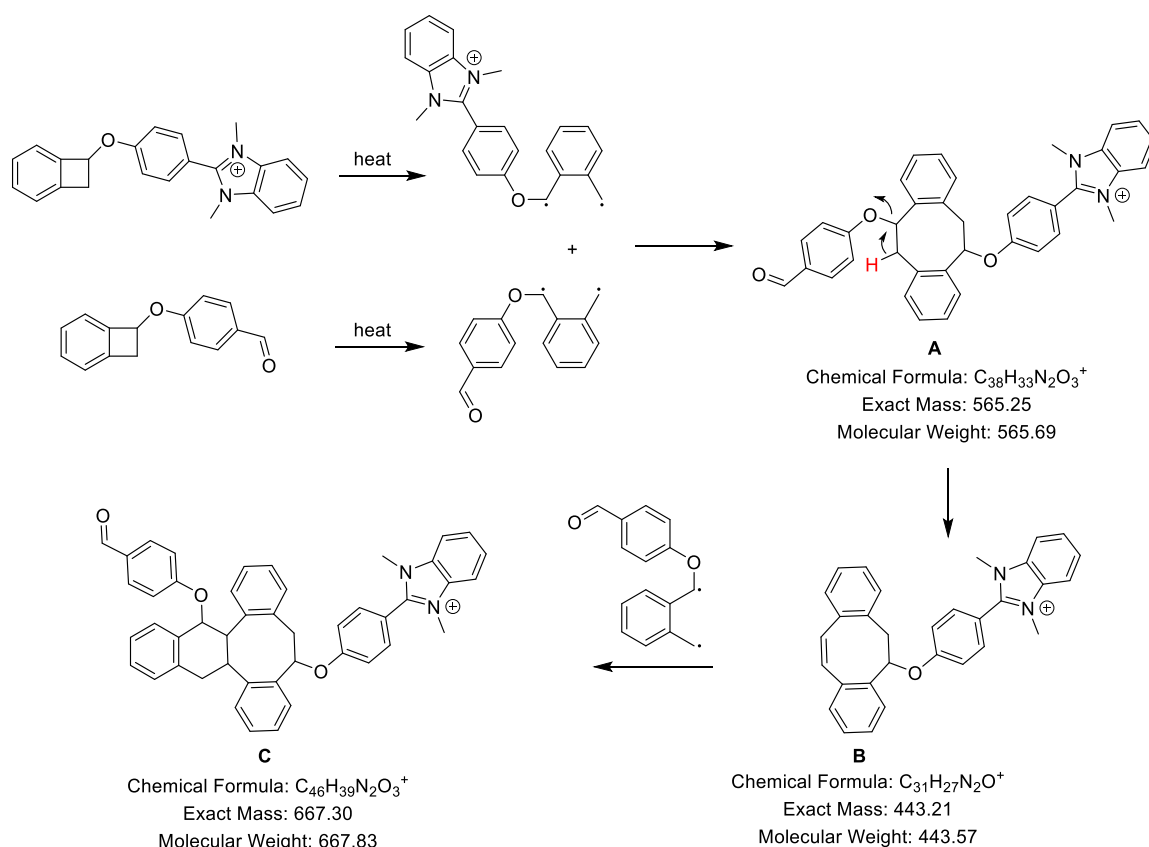


Figure 3.4 Assignments of possible chemical structures to the signals observed in MALDI-TOF-MS spectrum.

Although the above-mentioned work provides proof of principle for the compatibility of DMBI cations with the dimerization conditions for BCBs, the approach was modified in the light of recent findings. Specifically, Anthopoulos's group has shown that the introduction of a butoxide substituent at the 7-position of the benzocyclobutene unit could decrease the crosslinking temperatures to 120 °C,¹¹⁸ somewhat lower than reported for aryloxy derivatives such as those used in the preceding section, **3.2**. The crosslinking temperature of the butoxybenzocyclobutene (BBCB) could be suitable and compatible with thermal stability of DMBI units. Therefore, it was decided to synthesize a DMBI-H and a

fullerene derivative contains BBCB thermo-crosslinkable unit and characterize the doping products and the effect of crosslinking in solid state.

3.3 Synthesis of Low-temperature Thermo-crosslinkable DMBI-H

To synthesize a DMBI-H derivative that contains thermo-crosslinkable unit BBCB (BBCB-DMBI-H), compound **3.5** was synthesized in 6 steps, similar to the literature report.¹¹⁸ Treatment with *n*-BuLi at -78 °C, followed by addition of DMF, afforded butoxybicyclo[4.2.0]octa-1,3,5-triene-3-carbaldehyde **3.6**. It is worth mentioning that **3.5** and **3.6** are each obtained as mixtures of two regioisomers based on the position of butoxy group attached to four membered ring and based on ¹H NMR, the ratio of two isomers was estimate as ~ 95:5.

In the next step, **3.6** underwent reaction with *N,N'*-dimethyl-1,2-phenylenediamine in the presence of catalytic amount of acid to obtain the desired 2-(butoxybicyclo[4.2.0]octa-1,3,5-trien-3-yl)-1,3-dimethyl-2,3-dihydro-1*H*-benzo[*d*]imidazole in moderate yield as a mixture of two isomers, **3.7**, Figure 3.5.

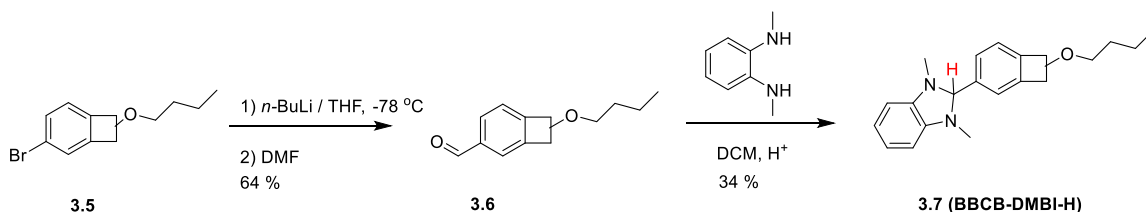


Figure 3.5 Synthesis of DMBI-H contains BBCB thermo-crosslinkable functional group, **3.7**.

3.4 Synthesis and Characterization of the Thermo-crosslinkable BBCBPCB

Synthesis of a PCBM-like fullerene with a BBCB thermal crosslinker was carried out as shown in Figure 3.5. The starting materials of [6,6]-phenyl- C_{60} -butyric acid (PCBA), synthesized from commercially sourced PCBM.¹¹⁹ Alcohol **3.6** was synthesized from the reduction of **3.5** in the presence of $NaBH_4$ in MeOH with 80% yield. The PCBA was subsequently reacted with **3.9** under *N,N*-dicyclohexylcarbodiimide (DCC)-assisted esterification conditions in *o*-DCB in order to obtain the desired product, phenyl- C_{61} -butyric acid butoxybenzocyclobutene ester **3.10** (BBCBPCB). BBCBPCB, which is readily soluble in common organic solvents (toluene, CH_2Cl_2 , benzene), was purified through column chromatography with 50% yield. It is also worth mentioning that PCBM-like fullerene with a BCB thermal crosslinker are known to undergo dimerization reactions through BCB-BCB type reactions and BCB- fullerene cage type reactions.¹¹⁹

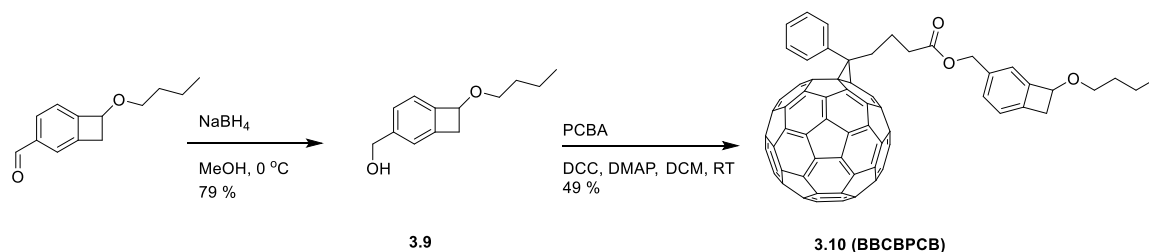


Figure 3.6 Synthesis of related fullerene with a BBCB thermal crosslinker, BBCBPCB.

3.4.1 Differential scanning calorimetry (DSC)

DSC analysis of the BBCBPCB in hermetically sealed Al pans was carried out from a starting temperature of -50 °C with heating to 300 °C at a rate of 10 °C min. The heating and cooling cycles are shown in Figure 3.7 (a). The first cycle showed a feature, beginning

at 120 °C, indicative of an exothermic chemical reaction, attributed to the dimerization or oligomerization reactions of BBCB.

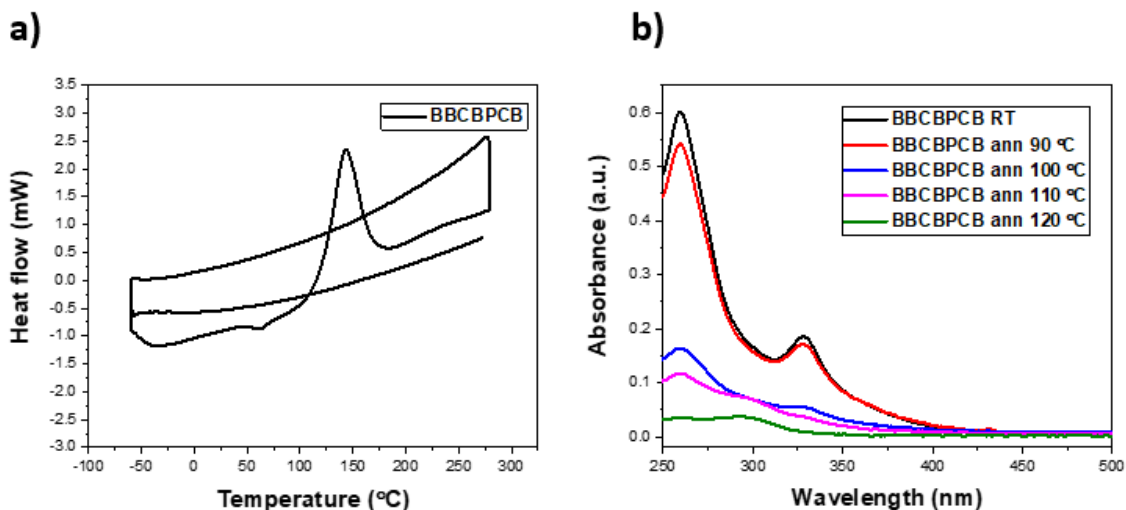


Figure 3.7 a) DSC thermogram of cross-linking reaction of BBCBPCB moieties and b) UV-vis absorption spectra of BBCBPCB annealed at different temperatures.

3.4.2 UV-vis spectra analysis

To determine the effect of heating the BBCBPCB precursor on solubility, UV-vis spectroscopy was used. Drop-cast films from the PCBBCB precursor (1 mg) in CH₂Cl₂ (1 ml) were deposited on glass substrates and annealed at different temperatures for 10 min. The films were subsequently washed with 1 ml of CH₂Cl₂ each and sonicated to remove any soluble parts of the film. These 1 ml solutions were diluted to 10 times their volume and the absorption spectra for those were then obtained. As it can be seen, by varying the annealing temperature from 90 °C to 120 °C, the percentage conversion increased; at 120 °C no detectable soluble material was obtained, suggesting 98% of the film to be insoluble, Figure 3.7 (b).

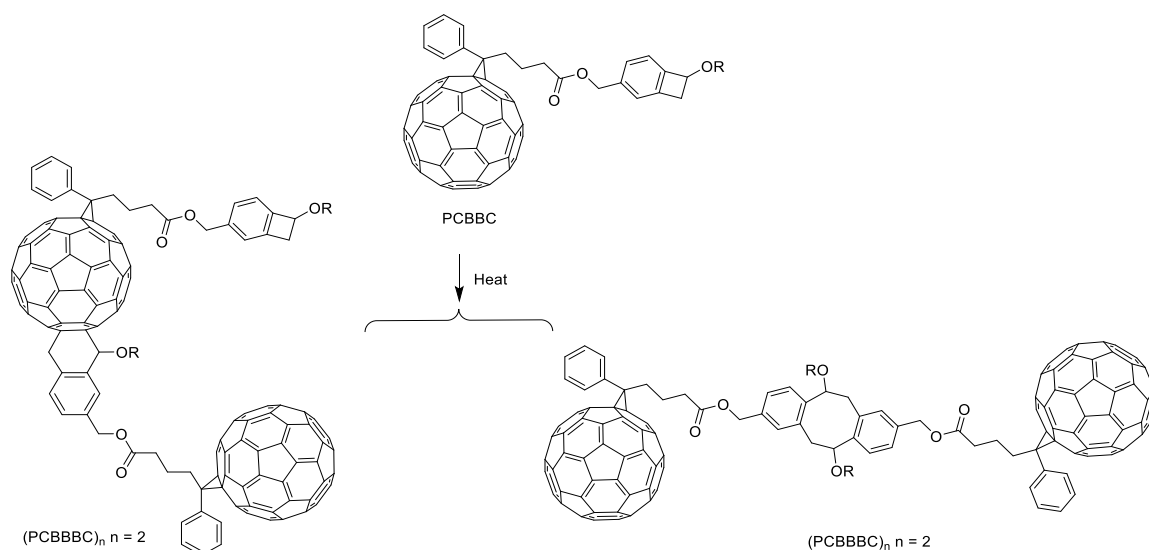


Figure 3.8 Schematic representation of oligomeric fullerene formation ((PCBBC)_n, n = 2) via thermal cross-linking of BCBPCB.

Experimentally, in the related PCBCB system, which differs in the BCB attachment chemistry and, therefore, crosslinking temperature, it was found that dimers (i.e., n = 2) are the major product of the thermally activated ring-opening reaction.¹¹⁹ However, since the crosslinked films are insoluble in DMF and o-DCB, it is reasonable to assume that larger oligomers may be formed as well. Figure 3.8 represents thermally activated reaction pathways of BCBPCB molecules, where two reactive o-xylylene intermediate groups can react together, and where a reactive o-xylylene intermediate group reacts with the fullerene cage.

The thermal crosslinking condition was also measured when films of BCBPCB were spin-coated (1000 rpm, 60 s). It was noticed that BCBPCB film (with 30 nm thickness) would undergo full insolubilization at 150 °C for 10 min, as the concentration of materials is significantly less compared to drop-casting condition.

3.5 Doping Products

3.5.1 Characterization of the reaction product(s) by MALDI-TOF-MS

The doping product(s) of the reaction of BBCB-DMBI-H and BBCBPCB were characterized by mass spectrometry. BBCBPCB (13.0 mg) and BBCB-DMBI-H (3.7 mg, 1.0 equivalent) were dissolved in o-DCB (1.0 ml) and heated at 120 °C for 90 min. The MALDI-TOF spectrum of the concentrated filtrate left from the precipitation reaction between BBCB-DMBI-H and BBCBPCB show a strong peak at 1405 m/z, which can be assigned to expected heterodimer, Figure 3.9.

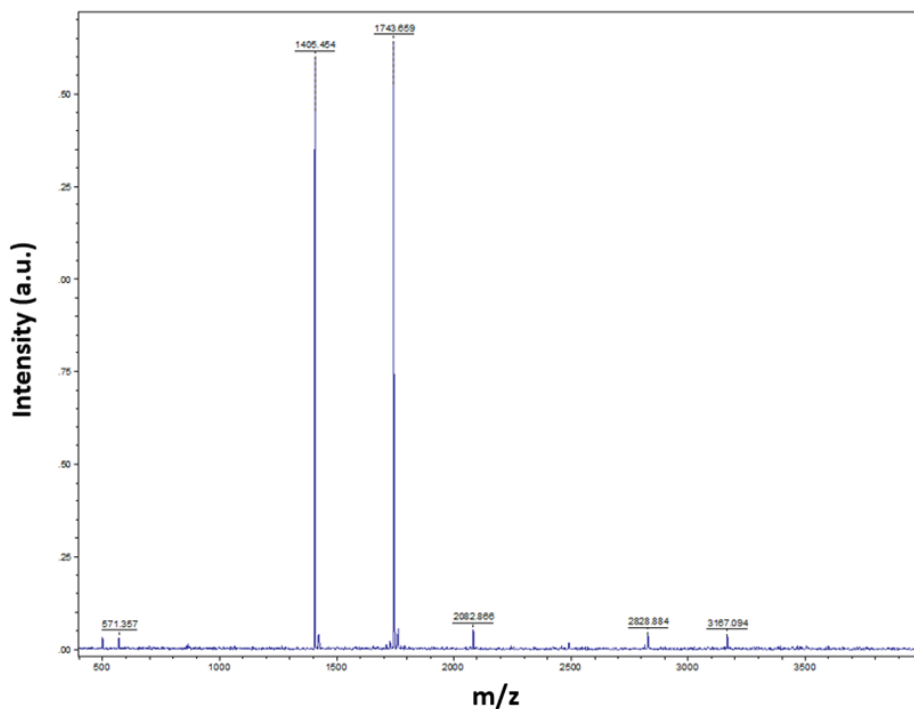


Figure 3.9 MALDI-TOF-MS spectra for the black precipitate formed from the reaction between BBCB-DMBI-H and BBCBPCB. Peak at 1405 m/z represents the mass of the heterodimer.

There was another signal at 1743 m/z that could be the decomposition product of the oligomer of BBCBPCB and BBCB-DMBI-H.

To characterize the insolubilization efficiency in solid state, an UV-vis experiment was performed. A solution of BBCB-DMBI-H (2.0 mg, 0.5 equivalent) and BBCBPCB (13.0 mg) was prepared in o-DCB in glove box. Films were spin-coated (1000 rpm, 60 s), annealed at 120 °C for 10 min and the UV-vis were obtained before and after rinsing the films with o-DCB, Figure 3.10.

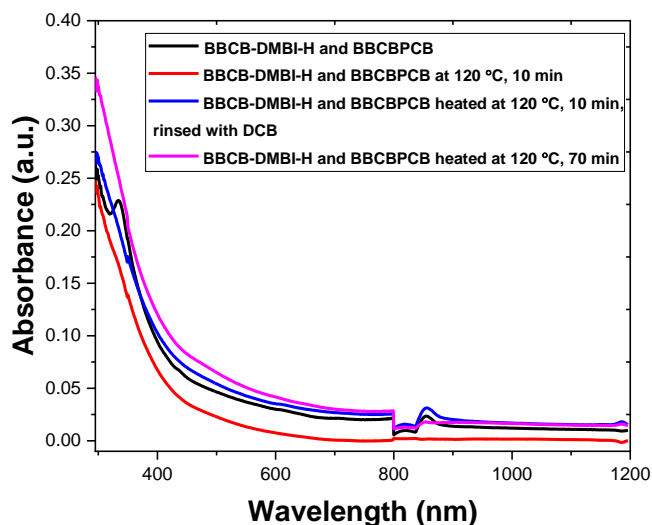


Figure 3.10 UV-vis experiment performed to measure the film retention of BBCB-DMBI-H and BBCBPCB to o-DCB.

No discernable reduction in the peak intensity at 360 nm was observed after rinsing the films with o-DCB, indicating high resistance (~100%) to o-DCB. Moreover, the peak corresponding to the fullerene radical anion (~ 900 nm) was not observed, even when the film was heated at 120 °C for 70 min. As it was observed in Chapter 2, section 2.3.2, the

fullerene radical anion signal in solid state is relatively weak and broad and may not be observed in all cases.

3.5.2 Characterization of the reaction product by electron paramagnetic resonance (EPR)

An EPR experiment was performed to get evidence of formation of fullerene radical anion. A solution of BBCB-DMBI-H (3.2 mg, 1.0 equivalent) and BBCBPCB (11.0 mg) was prepared in o-DCB, in 3 mm quartz EPR tubes and heated at 120 °C for 90 min. Solvent was evaporated under high vacuum overnight to obtain a thin film deposited on the wall of EPR tube. Undoped BBCBPCB films exhibited no appreciable radical signal by EPR spectroscopy.

However, co-deposition of BBCBPCB with BBCB-DMBI-H revealed two strong signals with g values of 2.001 and 2.003 indicating the presence of two radical species, suggesting the presence of two distinct types of fullerene radical anion, Figure 3.11. The signal with lower g-value (2.001) was assigned to radical anion species when BBCBPCB and BBCB-DMBI-H undergo cycloaddition reaction with another o-xylylene intermediate while the other signal at higher g-value (2.003) was associated with the species when o-xylylene intermediate attacks the C₆₀ cage (Figure 3.8). Kadish and co-workers also reported that the g-value of radical anion of C₆₀ could appear at higher g-value when the C₆₀ cage undergoes desymmetrization.¹²⁰

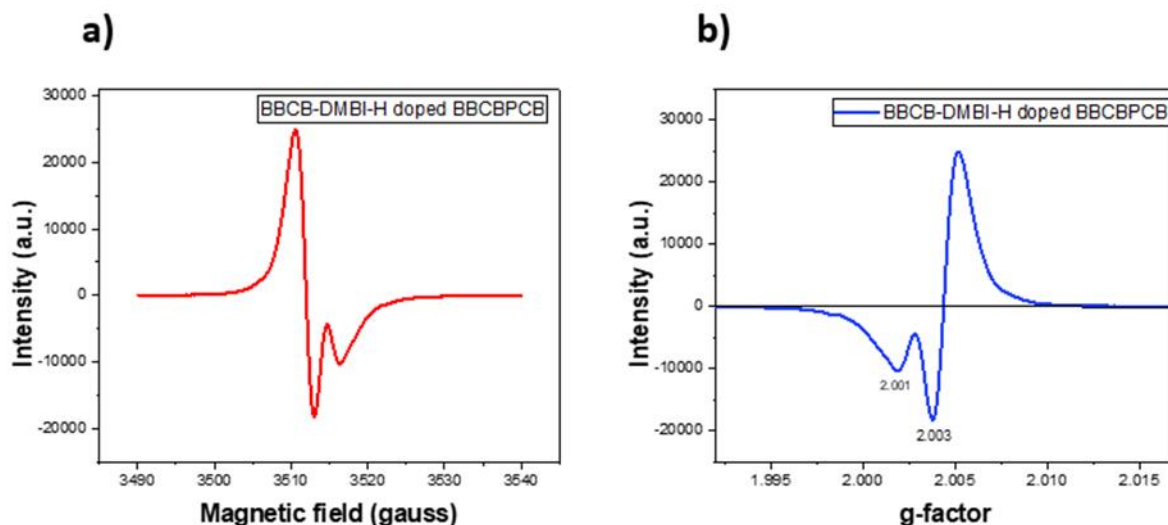


Figure 3.11 a) EPR spectra of BBCB-DMBI-H doped BBCBPCB and b) calculated g-values.

3.6 Synthesis of BBCB-N-DMBI-H as a Stronger Hydride Donor Derivative

BBCB-DMBI-H is a weak hydride donor. As it has been discussed in Chapter 2, the presence of a π -donor group such as a nitrogen and oxygen in the para position a DMBI-H derivative has been found to increase the reaction rate;⁶² therefore, in the next step, another derivative of DMBI-H was synthesized. The designed strategy is based on N-DMBI-H that contains two thermo-crosslinkable BBCB units that increase the chances for crosslinking of dopant and potentially better immobilization, while the presence of nitrogen also would increase the rate for the hydride transfer reaction. Figure 3.12 represents the synthesis of BBCB-N-DMBI-H.

First, aniline was used in a Buchwald-Hartwig amination reaction¹²¹ with 2.2 equivalent of compound **3.5** in the presence of XPhos to give compound **3.11** as a mixture of three

isomers that all were purified together though column chromatography with 83% yield. Next, **3.11** was reacted with POCl₃ and DMF (Vilsmeier reaction) to produce aldehyde **3.12** in 31% yield. The reaction of **3.12** with *N,N'*-dimethyl-1,2-phenylenediamine in acidic conditions yielded the BBCB-N-DMBI-H derivative that was purified though column chromatography to give a moderate yield (39%) of a yellow foam.

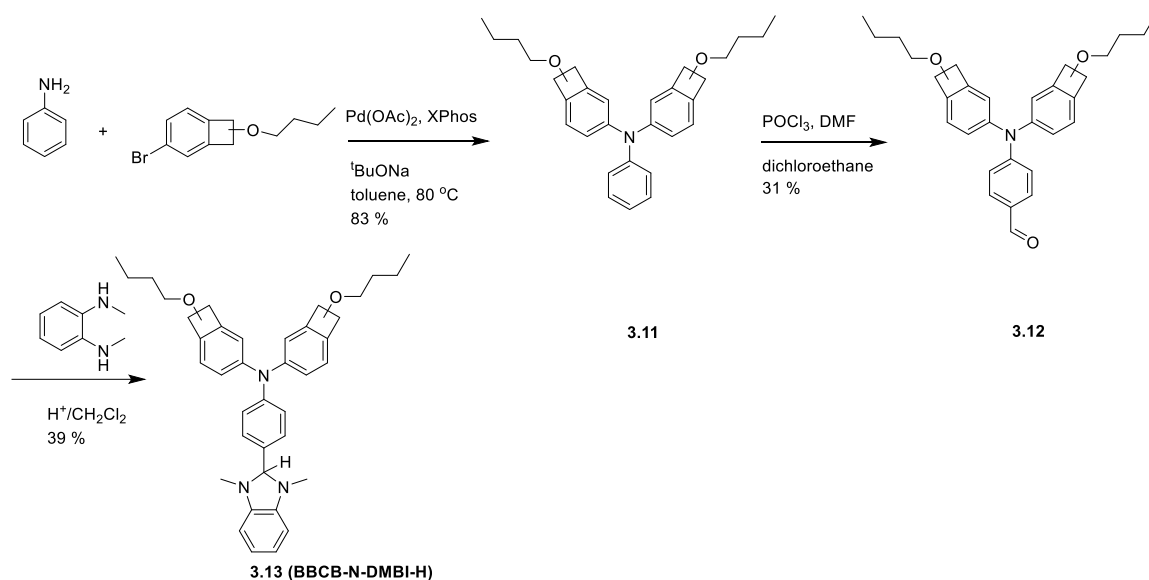


Figure 3.12 Synthesis route for BBCB-N-DMBI-H.

3.6.1 Characterization of the doping products by EPR and MALDI-TOF-MS

An EPR experiment was performed on BBCB-N-DMBI-H doped BBCBPCB and the result was compared to BBCB-DMBI-H doped BBCBPCB, Figure 3.13. To do so, a solution of BBCB-N-DMBI-H (1.08 mg, 20 mol%) and BBCBPCB (10.0 mg) was prepared in *o*-DCB, in 3 mm quartz EPR tubes and heated at 120 °C for 90 min. Solvent was evaporated under high vacuum overnight to obtain a thin film deposited on the wall of EPR tube. As it can be observed from Figure 3.13, compared to BBCB -DMBI-H doped BBCBPCB, only one signal was observed at higher magnetic field for BBCB-N-DMBI-H doped BBCBPCB.

Since BBCB-N-DMBI-H has two cross-linkable units attached, there is a higher possibility to react with C₆₀ cage and, therefore, the PCB radical anion with desymmetrized C₆₀ cage might predominate.

The same product was also analysed using MALDI-TOF-MS. The signal at 1671 m/z represents the mass of heterodimer (BBCB-N-DMBI-H:BBCBPCB) and the signal at 2755 m/z the mass of heterotrimer when the BBCB-N-DMBI-H:BBCBPCB reacted with another BBCBPCB molecule, Figure 3.14.

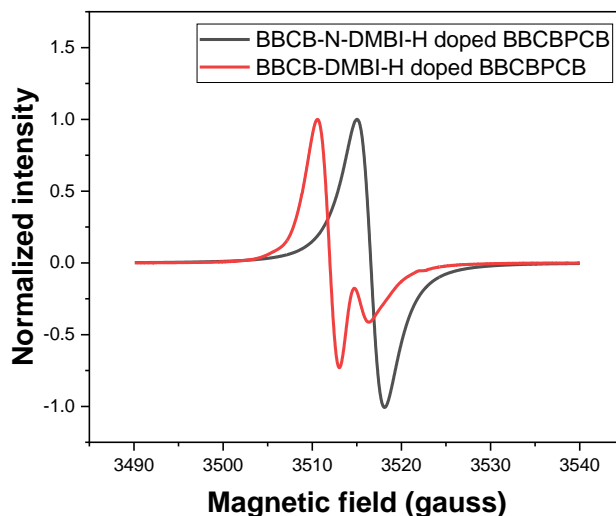


Figure 3.13 Comparison of normalized EPR spectra of BBCB-DMBI-H (red) and BBCB-N-DMBI-H doped BBCBPCB (gray).

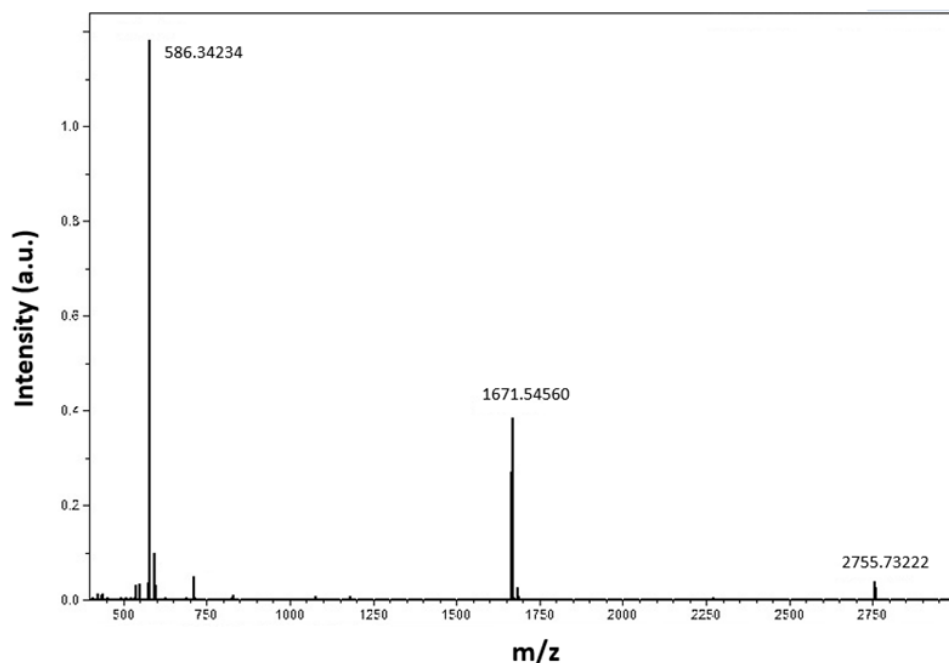


Figure 3.14 MALDI-TOF-MS spectra from the reaction between BBCBPCB and BBCB-N-DMBI-H. The signal at m/z 586 represents the mass of BBCB-N-DMBI-H after loss of a hydride, the signal at 1671 represents the mass of BBCB-N-DMBI-H:BBCBPCB dimer.

3.7 Diffusion Studies on BBCB-NDMBI-H-doped BBCBPCB Films

Diffusion of BBCB-N-DMBI-H into BBCBPCB was investigated using UV-vis-NIR method. A solution contains 80 mg of PPCBPCB and BBCB-N-DMBI-H (40 mol%) was prepared and stirred in the glove box overnight. The UV-vis-NIR of the solution was obtained to confirm that the doping reaction occurred (appearance of the signal for PCB radical anion around 900 nm). Films were spin-coated (1000 rpm, 60 s). One of the films was annealed at 150 °C for 10 min to crosslink. 2CN-NDI (a very strong electron acceptor (with reduction potential of -0.54 eV vs. ferrocene)⁶³ was evaporated (at 200 °C) and deposited on the top of doped films to reach the thickness of 300 nm. The films were sealed and the UV-vis-NIR of films were obtained and the results are depicted in Figure 3.15.

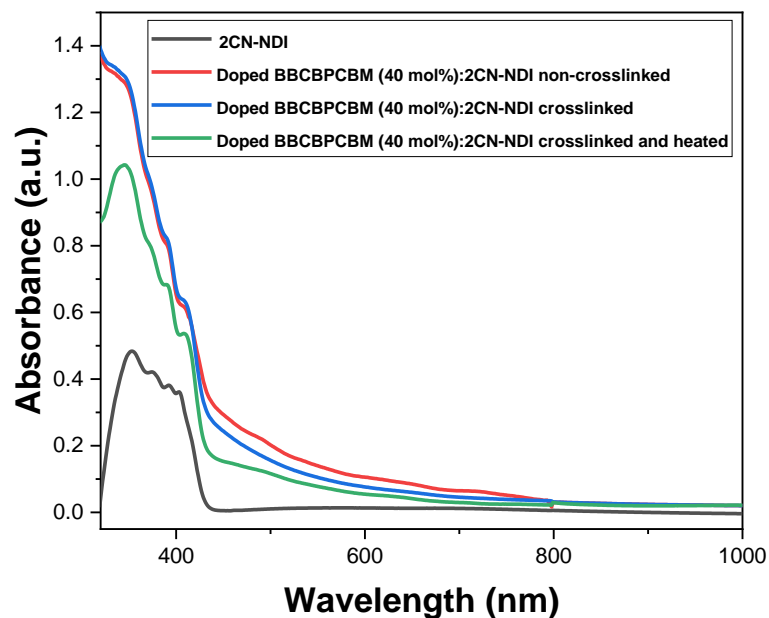


Figure 3.15 Investigation of diffusion rate of thermo-crosslinkable BBCB-N-DMBI-H/BBCB-N-DMBI cation into 2CN-NDI as a strong electron acceptor.

As it can be seen, there is no sign or increase in the intensity at wavelengths shorter than 800 nm for doped cross-linked films while the non-crosslinked films showed some increase in absorbance and broadening at wavelengths shorter than 800 nm, suggesting the presence of $2\text{CN-NDI}^{\bullet-}$.⁶³ To examine whether moderate heating could lead to discernable dopant diffusion in 2CN-NDI, a crosslinked film was heated then at 70 °C for 1 h and the UV-vis-NIR was obtained; again no sign of diffusion was observed.

A control experiment was performed on the solution processed doped BBCB-N-DMBI-H doped 2CN-NDI (20 mol%) and is shown in Figure 3.16. The doped film exhibited a broad signal between 480 – 800 nm, indicate of the formation of $2\text{CN-NDI}^{\bullet-}$, consistent with a literature report in solution for N-DMBI-H doped 2CN-NDI.⁶³

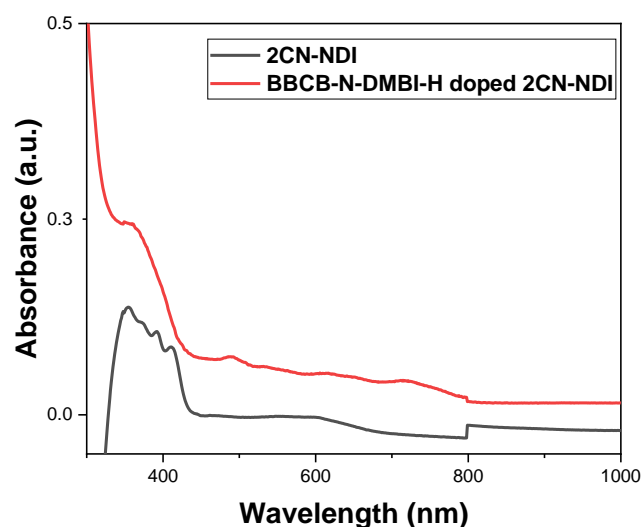


Figure 3.16 Optical absorption of solution processed doped film of BBCB-N-DMBI-H doped 2CN-NDI (20 mol%).

3.8 Summary and Conclusion

Thermal crosslinking using benzocyclobutene was investigated as an approach for immobilization of DMBI-H derivatives. The introduction of a butoxy group on the four membered ring of benzocyclobutane moiety can significantly lower the temperature at which the electrocyclic ring opening reaction responsible for cross-linking takes place (120 °C). Therefore, two new derivatives of DMBI-H and a new fullerene derivative with pendant butoxybenzocyclobutene (BBCB) groups were synthesized, (BBCB-DMBI-H, BBCB-N-DMBI-H and BBCBPCB). BBCBPCB could thermally crosslink in the range of 120 °C – 150 °C. DSC showed an exothermic peak attributed to the ring opening of cyclobutene. UV-vis experiment showed high retention of thermally annealed films on exposure solvents including o-DCB.

The doping products of the DMBI-H derivatives and BBCBPCB were characterized using MALDI-TOF-MS and EPR. Mass spectrometry confirmed the formation of heterodimer and EPR showed the signal for formation of PCB radical anion. UV-vis experiment also suggests that there was a high level of film retention upon exposure to o-DCB for BBCB-DMBI-H doped BBCBPCB. This approach is currently being studied and, in the future, it paves the way for diffusion studies of the DMBI-H in the solid-state, as covalent tethering of the dopant with organic semiconductors, in principle, is a way of minimizing diffusion.

3.9 Experimental Details

3.9.1 Synthesis

Chemicals were obtained from commercial sources and used as received unless stated otherwise. All operations involved in synthesis were performed under an atmosphere of nitrogen using standard Schlenk techniques or in a glove box. ^1H -NMR and ^{13}C -NMR spectra were recorded in CDCl_3 , C_6D_6 , CD_3OD or CD_2Cl_2 , on Varian 500 or 700 MHz spectrometers. The chemical shifts (δ) are reported in parts per million (ppm).

Synthesis of 4-(bicyclo[4.2.0]octa-1,3,5-trien-7-yloxy)benzaldehyde (3.2)

4-Hydroxybenzaldehyde (1.52 g, 12.4 mmol), triphenylphosphine (3.25 g, 12.3 mmol), and BCB-OH (1.5 g, 12.50 mmol) were dissolved in anhydrous THF (30 mL) and stirred under nitrogen in an ice bath. Diisopropyl azodicarboxylate (2.52 g, 12.4 mmol) was added slowly and let the reaction to stir at room temperature for 4 h. The reaction mixture was poured in 50 mL hexane to remove the unreacted triphenylphosphine oxide byproduct. The solvent was removed under reduced pressure and the product was purified by column

chromatography (6:1 hexane/EtOAc) to yield product as a white solid (1.8 g, 64%). ^1H NMR (500 MHz, CDCl_3) δ 9.92 (s, 1H), 7.92 – 7.86 (m, 2H), 7.41 – 7.33 (m, 1H), 7.31–7.27 (m, 2H), 7.22 (d, J = 7.2 Hz, 1H), 7.17 – 7.09 (m, 2H), 5.76 (dd, J = 4.3, 1.9 Hz, 1H), 3.78 (dd, J = 14.2, 4.3 Hz, 1H), 3.37 – 3.30 (m, 1H). $^{13}\text{C}\{^1\text{H}\}$ NMR (126 MHz, CDCl_3) δ 190.89, 163.17, 143.85, 142.47, 132.19, 130.39, 130.33, 127.74, 123.66, 123.13, 115.38, 74.55, 39.45. HRMS (ESI) calcd for $\text{C}_{15}\text{H}_{13}\text{O}_2$ ($\text{M}+\text{H}^+$), 225.0910; found 225.0907. Anal Calcd. For $\text{C}_{15}\text{H}_{12}\text{O}_2$: C, 80.34; H, 5.39, Found C, 80.11; H, 5.35.

Synthesis of 2-(4-(bicyclo[4.2.0]octa-1,3,5-trien-7-yloxy)phenyl)-1H-benzo[*d*]imidazole (3.3)

To a 20 mL vial with a Teflon septum, 4-(bicyclo[4.2.0]octa-1,3,5-trien-7-yloxy)benzaldehyde (100 mg, 0.44 mmol), 1,2-phenyldiamine (48.0 mg, 0.44 mmol) and $\text{Na}_2\text{S}_2\text{O}_5$ (84 mg, 0.44 mmol) were added. The vial was capped and evacuated and refilled with nitrogen 3 times. Anhydrous DMF (3.0 mL) was added, and the reaction mixture was heated at 100 °C overnight. The reaction mixture cooled down to room temperature, water (20 mL) added and extracted with DCM (3×30 mL). The combined organic layers were dried over Na_2SO_4 and solvent evaporated. The product was purified through column chromatography (1:1 hexanes/EtOAc) to yield a white solid (100 mg, 72 %). ^1H NMR (700 MHz, CD_3OD) δ 8.04 – 8.01 (m, 2H), 7.57 – 7.50 (m, 2H), 7.32 – 7.27 (m, 1H), 7.24 – 7.17 (m, 5H), 7.15 – 7.12 (m, 2H), 5.72 (dd, J = 14.1, 4.3 Hz, 1H), 3.71 (dd, J = 14.1, 4.3 Hz, 1H), 3.18 (dd, J = 14.2, 1.9 Hz, 1H). $^{13}\text{C}\{^1\text{H}\}$ NMR (176 MHz, CD_3OD) δ 161.28, 153.46, 145.84, 143.84, 131.12, 129.55, 128.52, 124.43, 123.94, 123.93, 123.71, 116.64, 75.59, 40.17. Two carbon signals are missing and most likely they are overlapped. HRMS

(ESI) calcd for $C_{21}H_{17}N_2O$ ($M+H^+$), 313.1335; found 313.1329. Anal Calcd. For $C_{21}H_{16}N_2O$: C, 80.75; H, 5.16; N, 8.97, Found C, 79.43; H, 5.07; N 8.76.

Synthesis of 2-(4-(bicyclo[4.2.0]octa-1,3,5-trien-7-yloxy)phenyl)-1,3-dimethyl-1H-benzo[d]imidazol-3-ium hexafluorophosphate (3.4)

To a 20 mL vial with Teflon septum, 2-(4-(bicyclo[4.2.0]octa-1,3,5-trien-7-yloxy)phenyl)-1H-benzo[d]imidazole (181 mg, 0.580 mmol), K_2CO_3 (800 mg, 5.79 mmol, 10.0 equivalent) added follow by addition of DMSO. The vial was capped and flushed with nitrogen for 5 min. Iodomethane (658 mg, 4.63 mmol, 8.0 equivalent) was added by syringe and the reaction mixture stirred at 80 °C for 12 h. Water was added to the mixture, which was then extracted with CH_2Cl_2 two times. The organic phase was dried over Na_2SO_4 and the solvent evaporated to obtain a white solid, 80 mg, 0.170 mmol. The solid was dissolved in MeOH (3.0 mL and tetrabutylammonium hexafluorophosphate (58 mg, 0.180 mmol) was added. After stirring for 1 h, a white precipitate was formed, which was filtered and dried under high vacuum to obtain off-white solid (70 mg, 28%). 1H NMR (500 MHz, $(CD_3)_2CO$) δ 8.15 – 8.08 (m, 2H), 8.07 – 8.01 (m, 2H), 7.86 – 7.78 (m, 2H), 7.57 – 7.48 (m, 2H), 7.44 (t, J = 7.5 Hz, 1H), 7.39 (d, J = 7.5 Hz, 1H), 7.35 – 7.30 (m, 1H), 7.28 (d, J = 7.4 Hz, 1H), 6.00 (dd, J = 4.3, 1.9 Hz, 1H), 4.14 (s, 6H), 3.92 (dd, J = 14.2, 4.1 Hz, 1H), 3.34 (d, J = 14.1 Hz, 1H). $^{13}C\{^1H\}$ NMR (126 MHz, $(CD_3)_2CO$) δ 162.67, 152.08, 144.93, 143.44, 133.73, 133.13, 131.12, 128.40, 127.79, 124.39, 123.91, 117.06, 113.99, 113.96, 75.44, 39.88, 33.46. HRMS (ESI) calcd for $C_{23}H_{21}N_2O$ ($M-PF_6^+$), 341.1648; found 341.1643. Anal Calcd. For $C_{23}H_{21}F_6N_2OP$: C, 56.80; H, 4.35; N, 5.76, Found C, 56.65; H, 4.43; N, 5.78.

Synthesis of 7-butoxybicyclo[4.2.0]octa-1,3,5-triene-3-carbaldehyde (**3.6**)

A solution of 3-bromo-7-butoxybenzocyclobutene (1.0 g, 3.91 mmol) in THF (25.0 mL) was stirred at -78°C under dry N_2 and treated dropwise with a solution of *n*-butyllithium (1.72 mL, 2.5 M in hexane, 4.30 mmol). The resulting mixture was kept at -78°C for 60 min, and then DMF (0.500 mL, 6.45 mmol) was added dropwise. The mixture was stirred overnight (12 h), while the temperature was allowed to rise to room temperature. To the solution water added and extracted with CH_2Cl_2 (3×30 mL). The combined organic layer was dried over Na_2SO_4 and solvent evaporated. The residue was purified over silica gel (10:1 hexane/EtOAc) to obtain the product as a mixture of two isomers (90:10) and pale-yellow oil (517 mg, 64%). ^1H NMR for the main isomer (500 MHz, CDCl_3) δ 9.96 (s, 1H), 7.83 (dd, $J = 7.6, 1.3$ Hz, 1H), 7.75 (s, 1H), 7.31 (dd, $J = 7.6, 1.0$ Hz, 1H), 5.07 (dd, $J = 4.5, 2.1$ Hz, 1H), 3.71-3.66 (m, 1H), 3.53 (dd, $J = 15.14.6$ Hz, 1H), 3.55-3.51 (m, 1H), 3.20 – 3.15 (m, 1H), 1.68 – 1.58 (m, 2H), 1.47 – 1.35 (m, 2H), 0.94 (t, $J = 7.4$ Hz, 3H). $^{13}\text{C}\{^1\text{H}\}$ NMR (126 MHz, CDCl_3) δ 192.43, 150.63, 147.46, 136.05, 132.51, 124.24, 123.60, 76.34, 69.25, 39.22, 32.02, 19.49, 14.05. The observed signals for the other isomer, δ 192.51, 153.52, 143.58, 137.78, 130.48, 124.40, 123.41, 78.51, 38.42. HRMS (ESI) calcd for $\text{C}_{13}\text{H}_{17}\text{O}_2$ ($\text{M}+\text{H}^+$), 205.1223; found 205.1221.

Synthesis of (BBCB-DMBI-H) (**3.7**)

In the glove box, to a 20 mL vial with Teflon septum, compound **3.6** (300 mg, 1.46 mmol) added and dissolved in 3.0 mL anhydrous CH_2Cl_2 followed by addition of *N,N'*-dimethyl-1,2-phenylenediamine (217 mg, 1.59 mmol). The vial was capped and transferred outside the glove box. Two drops of acetic acid were added by a syringe and the mixture was stirred

at room temperature for two days. The solvent was evaporated, and the product was purified on silica gel (4:1 hexane/CH₂Cl₂) to get a yellow oil and a mixture of two regioisomers (160 mg, 0.496 mmol, 34%). ¹H NMR (700 MHz, C₆D₆) δ 7.78 (s, 1H), 7.56 (dd, *J* = 7.5, 1.3 Hz, 1H), 7.14 (dd, *J* = 7.5, 1.0 Hz, 1H), 7.12 – 7.02 (m, 2H), 6.63 – 6.49 (m, 2H), 5.07–5.05 (m, 1H), 4.80 (s, 1H), 3.71–3.68 (m, 1H), 3.60–3.57 (m, 1H), 3.45 – 3.40 (m, 1H), 3.32 – 3.29 (m, 1H), 2.47 (d, *J* = 9.9 Hz, 6H), 1.78–1.73 (m, 2H), 1.58 – 1.53 (m, 2H), 1.04 (t, *J* = 7.4 Hz, 3H). ¹³C{¹H} NMR (176 MHz, C₆D₆) δ 148.42, 147.58, 144.15, 143.02, 141.16, 139.07, 130.67, 124.57, 123.47, 119.90, 119.89, 106.17, 106.14, 106.11, 106.09, 95.02, 94.94, 76.93, 76.87, 68.99, 68.80, 38.74, 38.55, 33.04, 33.02, 32.44, 32.42, 19.80, 19.57, 14.12, 14.11. HRMS (ESI) calcd for C₂₁H₂₆N₂O (M+H⁺), 323.2117; found 323.2117.

Synthesis of (8-butoxybicyclo[4.2.0]octa-1,3,5-trien-3-yl)methanol (3.9)

To a solution of 7-butoxybicyclo[4.2.0]octa-1,3,5-triene-3-carbaldehyde (1.0 g, 4.9 mmol) in dry THF (15 mL) at 0 °C was added sodium borohydride (223 mg, 5.86 mmol, 1.2 equivalent) and stirring was continued for another 2 h at room temperature. Excess sodium borohydride was quenched by addition of water. The mixture was extracted with EtOAc and the organic layer was separated, dried over Na₂SO₄, filtered and concentrated. The crude product was purified through column chromatography (5:1 hexanes/EtOAc) to yield the desired product as a mixture of two isomers as a colorless oil (800 mg, 79%). ¹H NMR for the main isomer (500 MHz, CDCl₃) δ 7.30 – 7.27 (m, 1H), 7.26 (s, 1H), 7.13 (dd, *J* = 7.5, 1.0 Hz, 1H), 5.02 (dd, *J* = 4.4, 2.0 Hz, 1H), 4.65 (s, 2H), 3.66 (m, 1H), 3.58 (m, 1H), 3.44 (dd, *J* = 14.1, 4.3 Hz, 1H), 3.13 – 3.06 (m, 1H), 1.69 – 1.57 (m, 2H), 1.48 – 1.33 (m, 2H), 0.94 (t, *J* = 7.4 Hz, 4H). ¹³C{¹H} NMR (126 MHz, CDCl₃) δ 146.71, 142.18, 140.01,

128.52, 123.70, 121.81, 76.55, 68.92, 66.02, 38.45, 32.07, 19.51, 14.06. Observed signals for the other isomer, δ 145.86, 143.02, 142.31, 126.16, 122.98, 122.45, 76.51, 68.79, 38.47. HRMS (ESI) calcd for $C_{13}H_{19}O_2$ ($M+H^+$), 207.1380; found 207.1378. Anal Calcd. For $C_{13}H_{18}O_2$: C, 75.69; H, 8.80, Found C, 75.54; H, 8.68.

Synthesis of PCBBCB (3.10)

PCBA¹¹⁹ (200 mg, 0.222 mmol), **3.9** (65.0 mg, 0.31 mmol) and 4-dimethylaminopyridine (41 mg, 0.33 mmol) was degassed in a flask and then dissolved in 100 mL of dichlorobenzene. The solution was sonicated for 30 min to allow complete dissolution and then cooled to 0 °C (in an ice bath) and stirred for 5 min. *N,N'*-dicyclohexylcarbodiimide, DCC, (46.0 mg, 0.22 mmol) was added to the solution and the mixture was stirred in ice bath for 3 h before warming it to room temperature. It was then allowed to stir at room temperature for 48 h. The crude product collected was purified through column chromatography (2:1 CH_2Cl_2 /hexanes or toluene) to yield **BBCBPCB** (120 mg, 49%). ¹H NMR (700 MHz, CD_2Cl_2) δ 7.96 (m, 2H), 7.55 (t, $J = 7.6$ Hz, 2H), 7.49 (m, 1H), 7.28 – 7.10 (m, 3H), 5.07 (s, 2H), 5.03 – 4.94 (m, 1H), 3.62 (q, $J = 7.3$ Hz, 1H), 3.55 (d, $J = 7.3$ Hz, 1H), 3.42 (dd, $J = 14.1, 4.3$ Hz, 1H), 3.04 (d, $J = 14.1$ Hz, 1H), 2.98 – 2.87 (m, 2H), 2.55 (t, $J = 7.4$ Hz, 2H), 2.21–2.12 (m, 2H), 1.59 (p, $J = 7.0$ Hz, 2H), 1.40 (q, $J = 7.5$ Hz, 2H), 0.93 (t, $J = 7.5$ Hz, 3H). ¹³C{¹H} NMR (176 MHz, CD_2Cl_2) δ 172.73, 149.11, 147.99, 146.93, 145.98, 145.29, 145.20, 145.16, 145.06, 144.88, 144.79, 144.75, 144.69, 144.51, 144.39, 144.05, 143.78, 143.09, 143.02, 143.01, 142.99, 142.96, 142.94, 142.88, 142.27, 142.15, 140.95, 140.72, 138.18, 138.01, 137.47, 137.29, 136.91, 135.03, 132.24, 129.57, 129.01, 128.40, 128.22, 128.20, 127.19, 125.27, 123.64, 123.49, 122.77, 122.74, 80.07, 76.46, 68.84, 66.82, 53.86, 53.81, 53.70, 53.65, 53.50, 53.34, 53.26, 53.19, 52.12, 38.45,

34.03, 33.64, 32.05, 22.44, 22.43, 21.20, 19.46, 19.45, 13.79, 13.76. HRMS (MALDI) calcd for $C_{84}H_{28}O_3$ (M^+), 1084.2038; found 1084.2056. Anal Calcd. For $C_{84}H_{28}O_3$: C, 92.97; H, 2.60, Found C, 91.56; H, 2.71.

Synthesis of compound (3.11)

To a 250 mL two neck flask with a reflux condenser, $Pd(OAc)_2$ (224 mg, 1.0 mmol) and 2-dicyclohexylphosphino-2',4',6'-triisopropylbiphenyl (XPhos) (0.086 g, 1.05 mmol), aniline (1.8 g, 10.4 mmol), compound 3.5 (6.0 g, 23.5 mmol), and NaO^tBu (3.4 g, 35.3 mmol) were added. The flask was sealed and evacuated refilled with nitrogen three times. Anhydrous toluene (100 mL) added, and the mixture was heated at 80 °C for two days. The reaction mixture was cooled down to room temperature. Water (30 mL) added, and the organic layer was extracted with CH_2Cl_2 (3×100 mL). The combined organic layer was dried over Na_2SO_4 and filtered. The solvent was evaporated under reduced pressure and the crude product collected was purified through column chromatography (8:1 hexane: EtOAc) to yield the desired product, as a mixture of isomers (3.86 g, 83%). 1H NMR (700 MHz, $CDCl_3$) δ [7.22-7.18 (m), 7.11 – 7.09 (m), 7.04 – 7.01 (m), 6.96 – 6.92 (m), 6.87 (s), 11 H], [5.00 – 4.98 (m), 4.97 – 4.95 (m), 2H], [3.66 – 3.63 (m), 3.62 – 3.58 (m), 3.57 – 3.53 (m), 4H]. [3.41 (dd, $J = 13.9, 4.4$ Hz), 3.37 (d, $J = 14.0$), 2H], [3.07 (dd, $J = 14.0, 2.0$ Hz), 3.03 (d, $J = 14.0$ Hz), 2H], 1.69 – 1.57 (m, 4H), 1.49 – 1.37 (m, 4H), [0.96 (t, $J = 7.4$ Hz), 0.93 (t, $J = 7.5$ Hz), 6H]. For ^{13}C NMR, all observed signals for isomers are reported; $^{13}C\{^1H\}$ NMR (176 MHz, $CDCl_3$) δ 149.66, 148.72, 148.57, 147.63, 147.53, 147.10, 147.08, 147.06, 143.41, 143.37, 140.35, 137.30, 137.18, 137.00, 136.97, 129.17, 129.15, 127.13, 126.90, 126.89, 124.59, 124.57, 124.56, 124.04, 124.02, 123.86, 123.84, 123.46, 123.03, 122.07, 121.77, 120.07, 120.05, 119.83, 119.80, 119.78, 76.40, 76.39, 76.34,

76.32, 68.99, 68.98, 68.86, 38.44, 38.42, 38.24, 38.19, 32.10, 32.04, 32.02, 19.54, 19.47, 19.46, 14.08, 14.03. HRMS (ESI) calcd for $C_{30}H_{36}NO_2$ ($M+H^+$), 442.2740; found 442.2734. Anal Calcd. For $C_{30}H_{35}NO_2$: C, 81.59; H, 7.99; N, 3.17, Found C, 81.42; H, 8.18; N, 3.17.

Synthesis of aldehyde (3.12)

Phosphorus oxychloride (2.53 g, 16.5 mmol) was added into DMF (1.2 g, 16.4 mmol) at 0 °C under nitrogen. After stirred at 0 °C for 30 min, compound 3.11 (4.86 g, 11.0 mmol) in 1,2-dichloroethane (20 mL) was added into reaction mixture at 0 °C. The reaction mixture was stirred at 60 °C for 15 h. The resulting mixture was poured into an iced water (150 mL), neutralized with sodium Na_2CO_3 . The product was extracted with dichloromethane (2×100 mL). After removal of solvents, the crude product was purified through column chromatography on silica gel (5:1 hexane: EtOAc), as a mixture of isomers, yellow oil (1.6 g, 31%). 1H NMR for the major isomer (700 MHz, $CDCl_3$) δ 9.76 (s, 1H), 7.63 (d, $J = 8.8$ Hz, 2H), 7.13 – 7.10 (m, 4H), 7.10 – 7.07 (m, 2H), 6.92 (dd, $J = 8.9, 2.5$ Hz, 2H), 4.97 (m, 2H), 3.62–3.58 (m, 2H), 3.57–3.53 (m, 2H), 3.44 (dd, $J = 14.2, 4.4$ Hz, 2H), 3.09 (dd, $J = 14.2, 2.1$ Hz, 2H), 1.63 – 1.57 (m, 4H), 1.43 – 1.35 (m, 4H), 0.91 (t, $J = 7.5$ Hz, 6H). For ^{13}C NMR, all observed signals for isomers were reported; $^{13}C\{^1H\}$ NMR (176 MHz, $CDCl_3$) δ 190.31, 153.94, 147.56, 147.56, 145.35, 145.34, 139.65, 139.60, 128.60, 128.56, 128.40, 128.38, 125.11, 125.08, 121.62, 121.60, 118.25, 118.20, 76.16, 76.14, 69.07, 38.36, 38.34, 31.90, 31.89, 19.35, 13.91. HRMS (ESI) calcd for $C_{31}H_{36}NO_3$ ($M+H^+$), 470.2690; found 470.2686. Anal Calcd. For $C_{31}H_{35}NO_3$: C, 79.28; H, 7.51; N, 2.98, Found C, 79.57; H, 7.79; N, 2.98.

Synthesis of BBCB-N-DMBI-H (3.13)

In the glove box, to a 20 mL vial with Teflon septum compound **3.12** (1.4 g, 2.98 mmol) was added and dissolved in 12.0 mL anhydrous CH₂Cl₂ followed by addition of N,N'-dimethyl-1,2-phenylenediamine (490 mg, 3.59 mmol, 1.2 equivalent). The vial was capped and transferred outside the glove box. Two drops of acetic acid were added by a syringe and the mixture was stirred at room temperature for 5 days. The solvent was evaporated and the product was purified on silica gel (10:1 hexane/EtOAc) to obtain a yellow foam (700 mg, 1.19 mmol, 39%). ¹H NMR for the main isomer: ¹H NMR (700 MHz, CD₂Cl₂) δ 7.42 – 7.38 (m, 2H), 7.12 – 7.08 (bro, 4H), 7.06 – 7.01 (m, 4H), 6.70 – 6.68 (dd, *J* = 5.4, 3.1 Hz, 2H), 6.44 – 6.41 (dd, *J* = 5.4, 3.2 Hz, 2H), 4.98 (dd, *J* = 4.4, 1.9 Hz, 2H), 4.81 (s, 1H), 3.63 – 3.59 (m, 2H), 3.58 – 3.55 (m, 2H), 3.44 (dd, *J* = 14.0, 4.4 Hz, 2H), 3.05 (dd, *J* = 14.0, 1.9 Hz, 2H), 2.59 (s, 6H), 1.63 – 1.58 (m, 4H), 1.45 – 1.39 (m, 4H), 0.94 (t, *J* = 7.4 Hz, 6H). ¹³C NMR for all isomers and, ¹³C{¹H} NMR (176 MHz, C₆D₆) δ 150.12, 148.26, 147.90, 147.88, 142.75, 137.97, 137.90, 132.39, 130.18, 127.64, 127.60, 125.06, 125.03, 122.06, 120.63, 120.61, 119.85, 119.84, 106.21, 94.20, 76.69, 76.66, 68.80, 38.38, 38.34, 33.22, 32.42, 32.40, 19.74, 14.10, 14.08. ESI-MS 586.3433 (M-H⁺), Anal Calcd. For C₃₉H₄₅N₃O₂: C, 79.69; H, 7.72; N, 7.15, Found C, 79.14; H, 7.93; N, 7.21.

3.9.2 Selected ¹H NMR and ¹³C NMR spectra

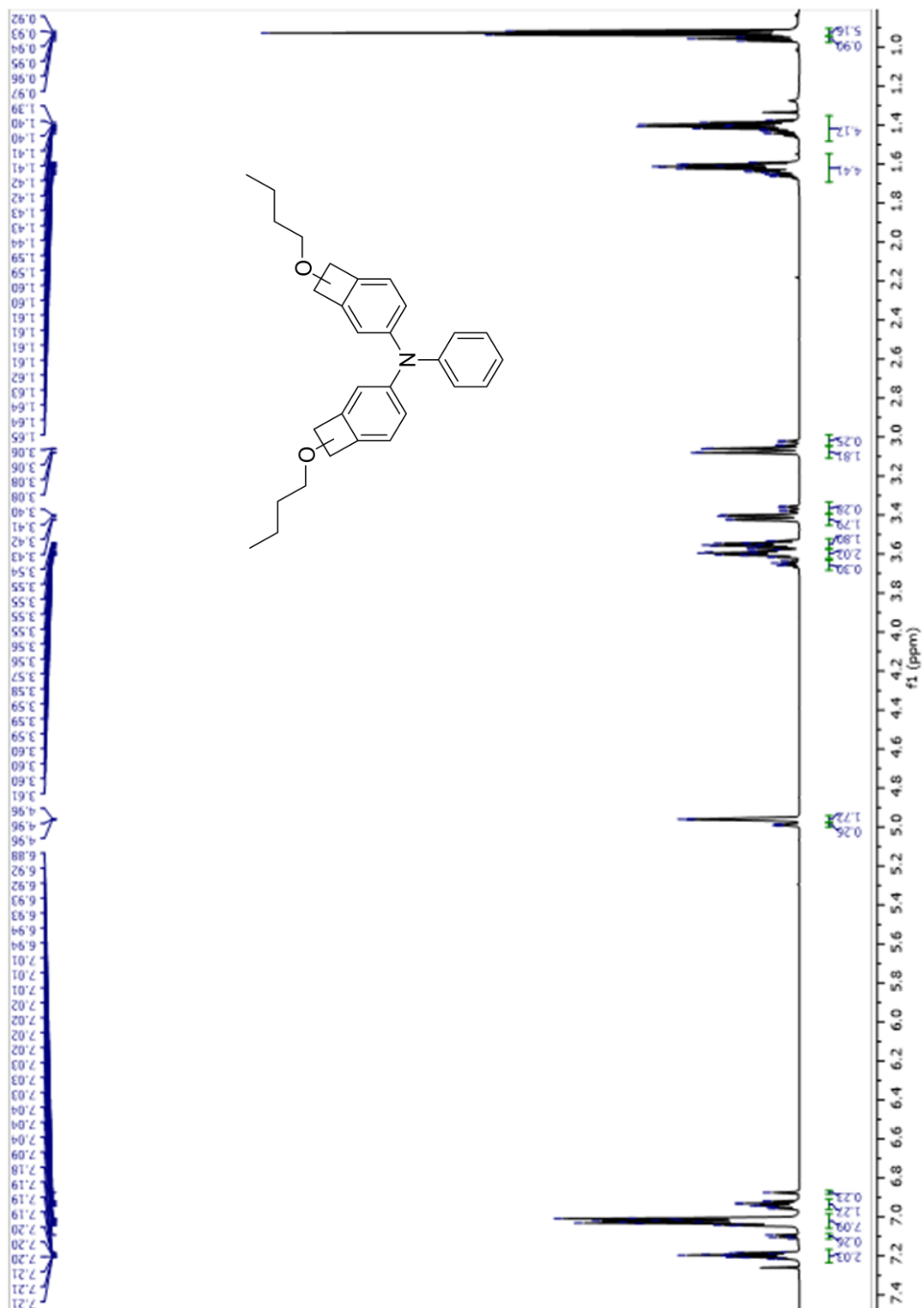
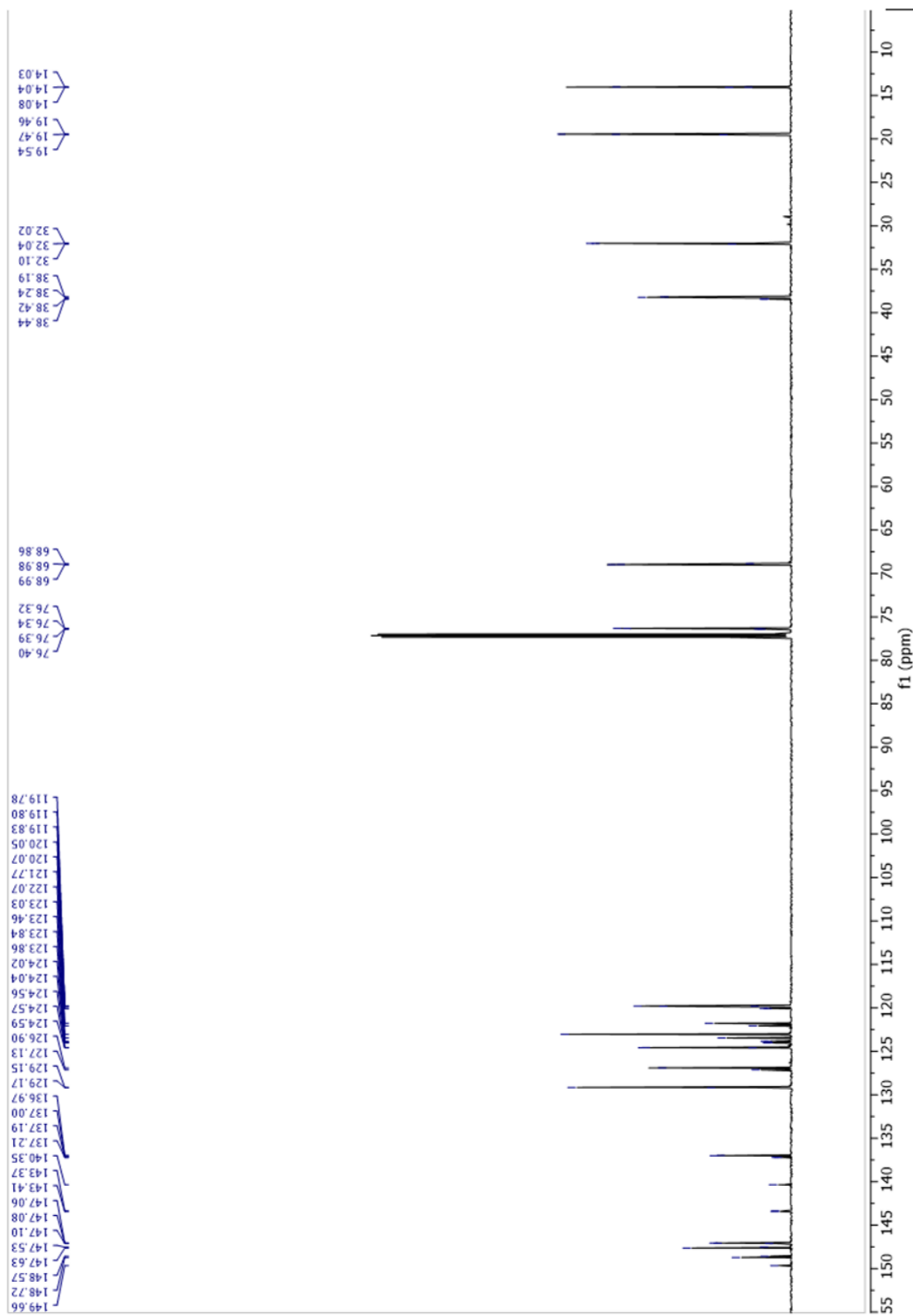


Figure S1. ^1H NMR spectrum of compound **3.11** in CDCl_3 .



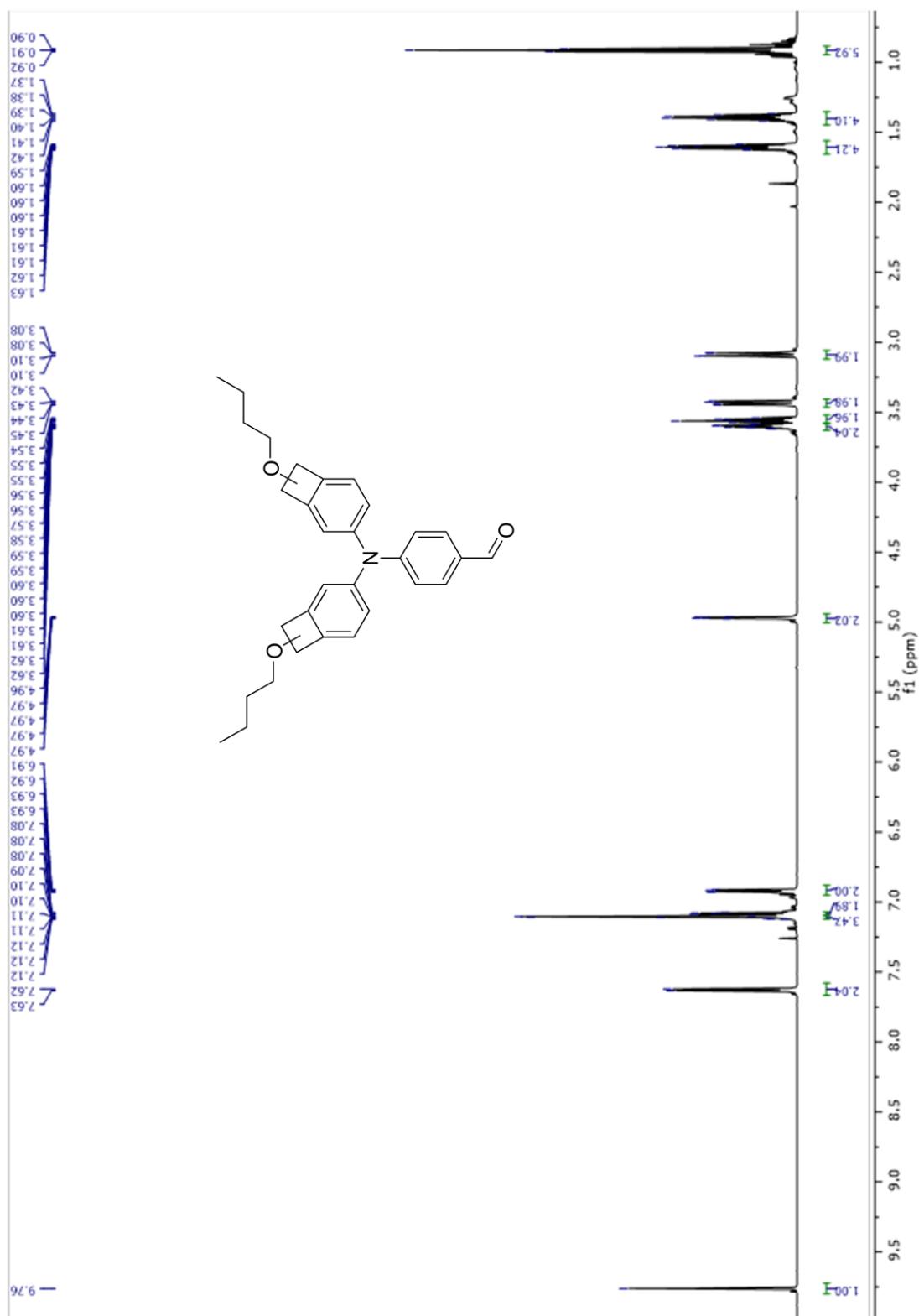


Figure S4. ¹H NMR spectrum of compound 3.12 in CDCl₃.

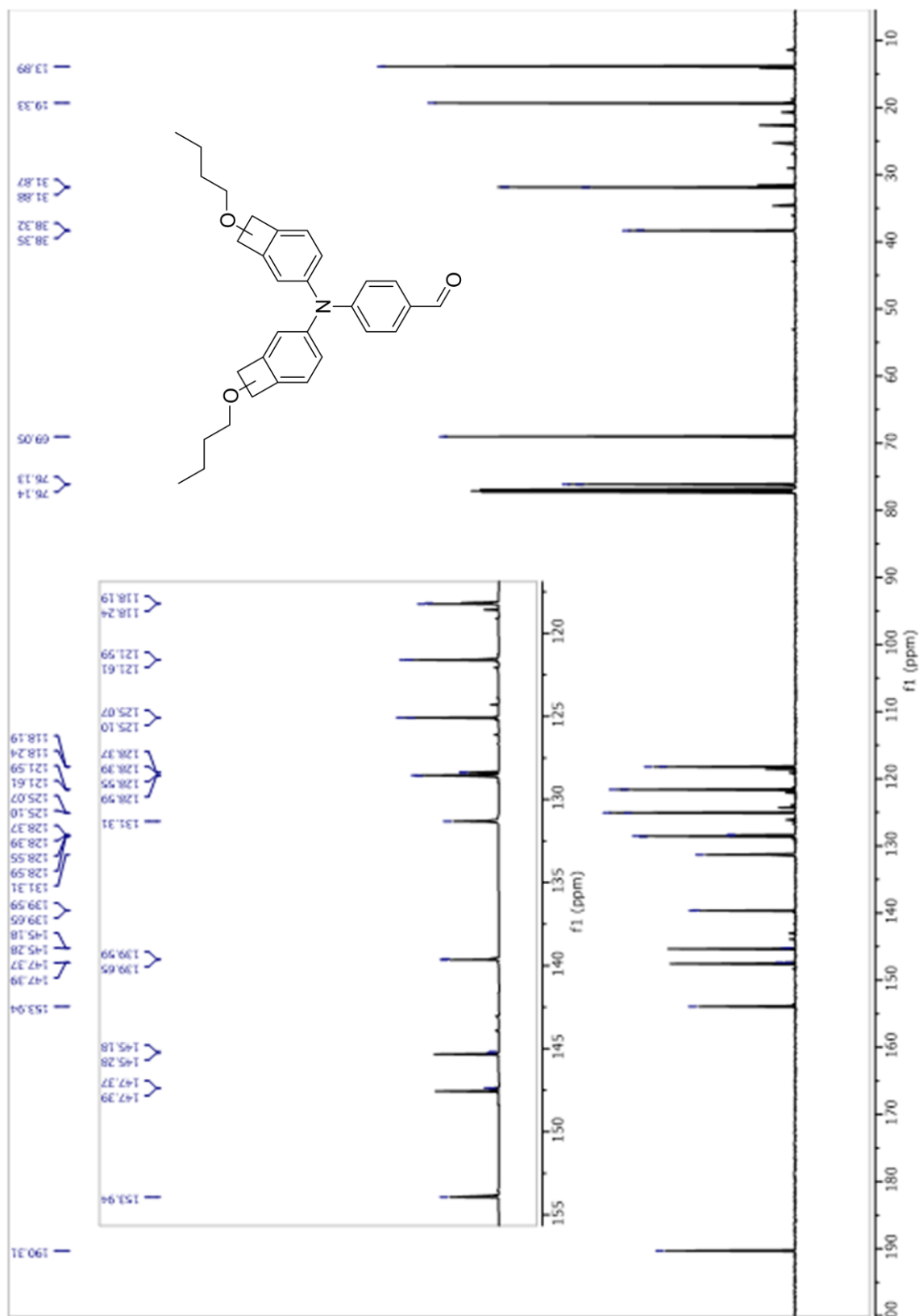


Figure S5. ¹³C NMR spectrum of compound 3.12 in CDCl₃.

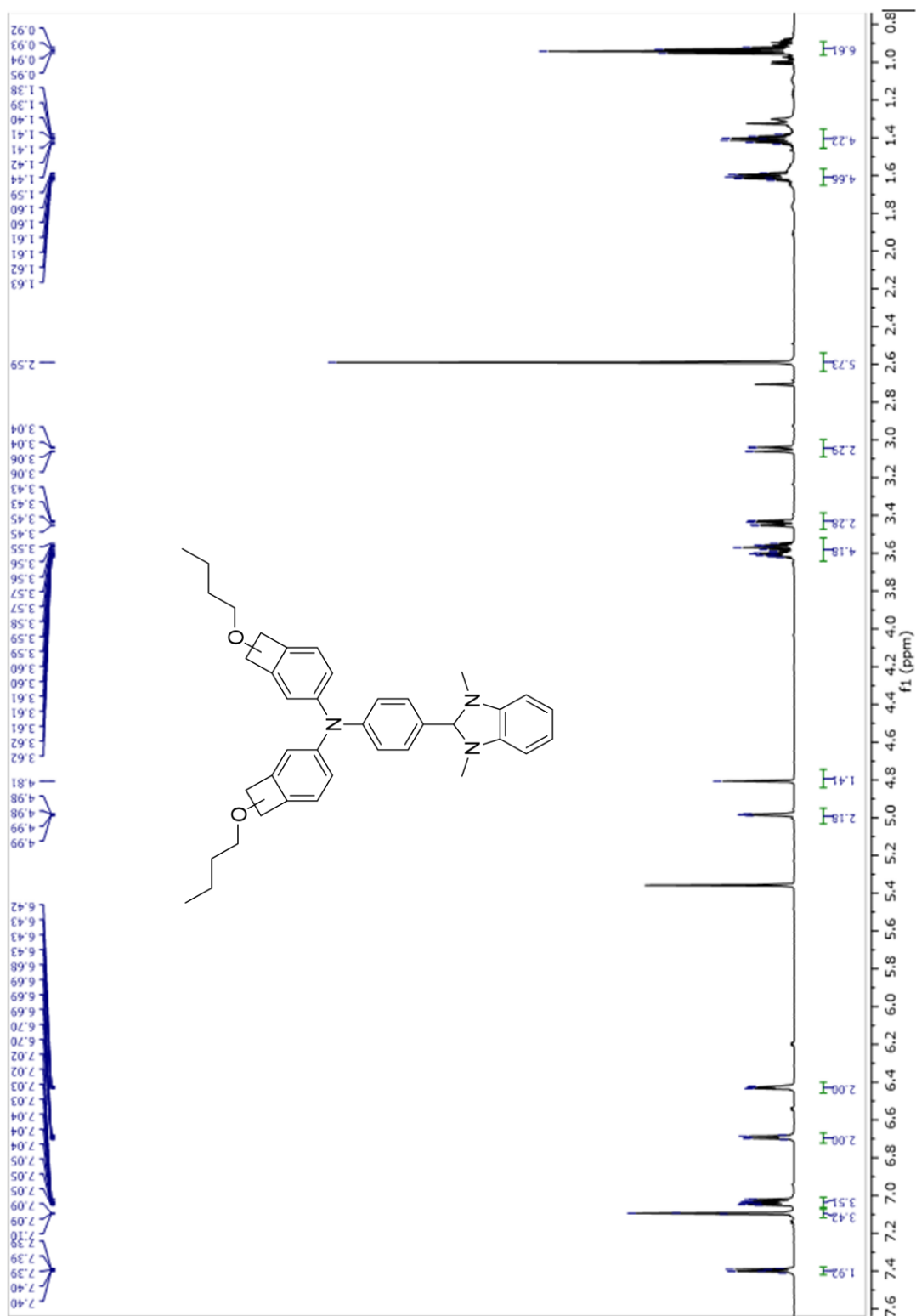


Figure S6. ¹H NMR spectrum of compound 3.13 (BBCB-N-DMBI-H) in CD₂Cl₂.

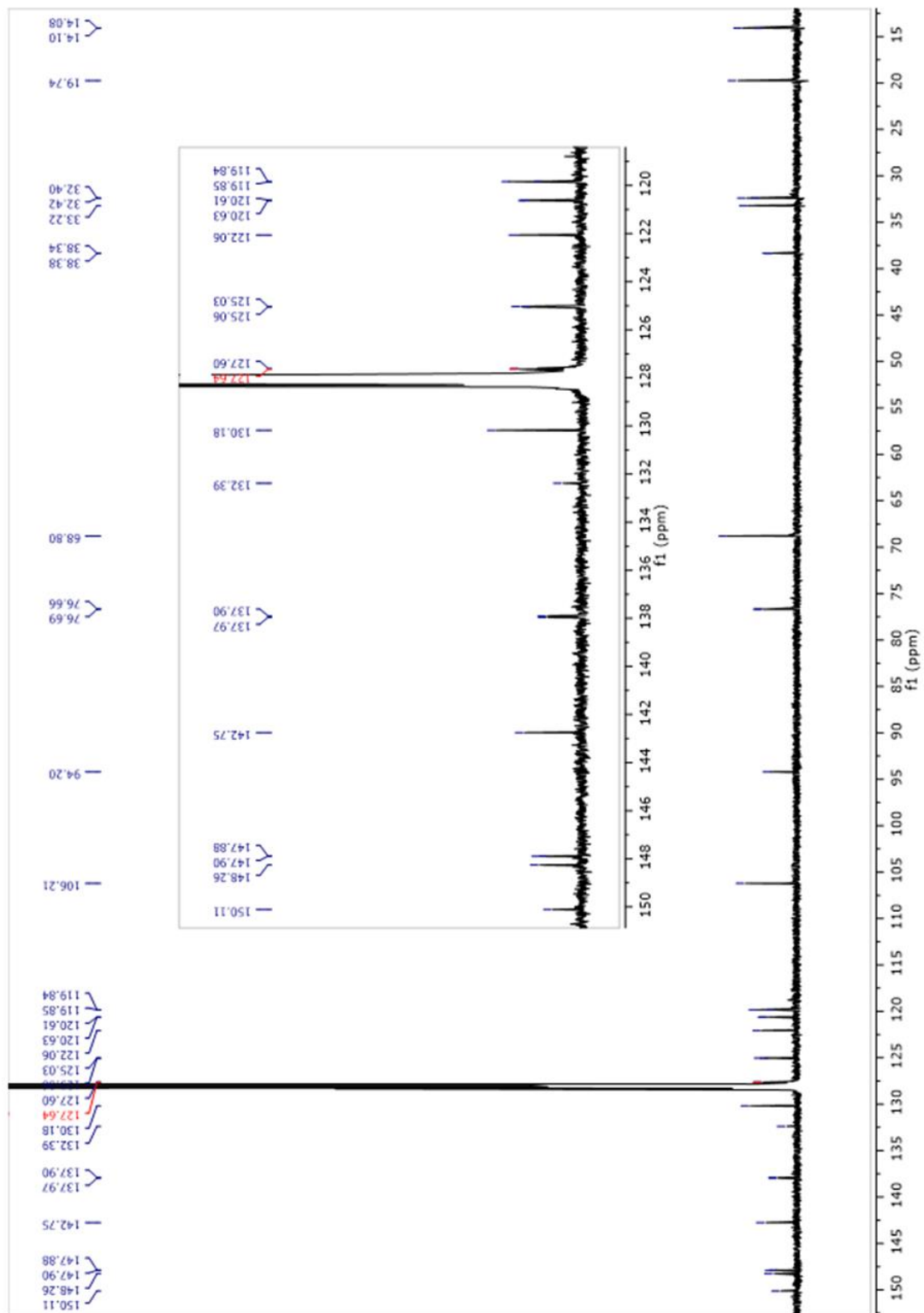


Figure S7, ^{13}C NMR spectrum of compound 3.13 (BBCB-N-DMBI-H) in C_6D_6 .

3.9.3 *Characterizations: general procedures and experimental details*

All stock solutions were prepared under nitrogen atmosphere in an inert gas box using dried 1,2-dichlorobenzene (o-DCB). The stock solutions were stirred overnight in order to enable complete dissolution of the materials.

Optical absorption spectroscopy was performed using a Cary 5000 UV–vis-NIR spectrometer. Undoped and doped thin films were prepared on glass substrates with thickness between 20 and 80 nm.

The EPR measurements were performed on an X-band Bruker EMX operating 9.44 GHz with a Bruker SHQ cavity.

CHAPTER 4: INVESTIGATION OF THE EFFECT OF A POLAR SIDE CHAIN ON THE DOPING BEHAVIOR OF A DMBI-H DERIVATIVE

This project is a collaboration among:

- Marder group, Georgia Tech (Farzaneh Saeedifard, Stephen Barlow, Seth Marder):
Synthesis and characterization of dopants
- Jurchescu group, Wake Forest University (Colin Tyznik, Oana Jurchescu):
Electrical conductivity and transistor measurements
- Toney group, CU Boulder (Thomas Chaney, Mike Toney): GIWAXS
measurements

The content of this chapter is unpublished.

4.1 Introduction

The development of n-type doping of organic semiconductors still lags behind that of their p-type counterparts. One of the key factors is the relatively low doping efficiency (the stoichiometric ratio of free carrier density to dopant density), especially with DMBI-H derivatives.⁹⁷ For example, N-DMBI-H has been used as a dopant to dope PCBM and achieved an electrical conductivity of $1.9 \times 10^{-3} \text{ S cm}^{-1}$, which (as discussed in the following paragraph is thought to partly represent poor doping efficiency).⁹⁷ A maximum conductivity of $\approx 10^{-3} \text{ S cm}^{-1}$ and doping efficiency of $\approx 1\%$ for the benchmark electron-transporting polymer (N2200) n-doped with N-DMBI-H were reported and the low doping efficiency was attributed to poor host/dopant miscibility.⁸⁴

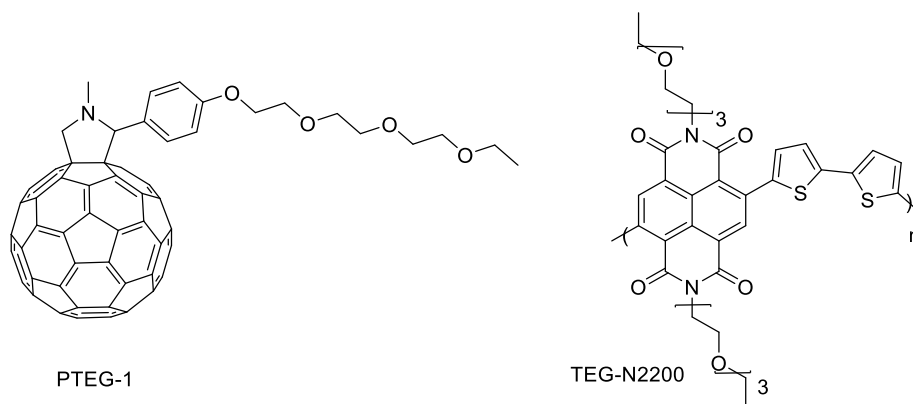


Figure 4.1 Structures of some of the compounds in Chapter 5.

By functionalizing the fullerene derivatives with polar glycol ether side chains, higher electrical conductivity of over 2 S cm^{-1} and doping efficiency of 18% was obtained when using 30 mol% of N-DMBI-H.¹²² By tailoring the side chains of N2200 polymer, using polar triethylene glycol type side chains instead of the traditional alkyl side chains (TEG-

N2200, Figure 4.1), a doping efficiency of 20% was obtained using 20 mol% of N-DMBI-H.¹²³ The insertion of polar side chains increases the polarity of the host, which improves the miscibility of the polar dopant molecules and the resulting dopant ions in the doped films and thus encourages higher doping efficiency, as it has been investigated using coarse-grained molecular dynamics simulations that indicated a rather strong tendency for the apolar alkyl environment to induce clustering of the dopant molecules, as opposed to the polar TEG phase, which instead favors the molecular dispersion of N-DMBI-H.

Moreover, increasing the length or the steric hindrance of the alkyl substituents on DMBI-H derivatives has been used as an effective strategy to improve the miscibility between dopant and host, leading to optimized electrical conductivity.¹²⁴

All the mentioned work focused on n-doped systems with a high doping concentration. Recently, the Koster group investigated the effect of polar side chains on the doping mechanism at a molecular level.¹²⁵ By inclusion of a triethylene glycol type side chain on a fullerene derivative (PTEG-1, Figure 4.1), very high doping efficiency (approaching 100%) was obtained using N-DMBI-H.

Molecular doping consists of two distinct processes: Firstly, the n-dopant is ionized, transferring a charge to (or accepting a charge from in the case of a p-dopant) the host material to form tight ion pairs (or integer charge transfer complexes (CTCs), although, as it has been mentioned in Chapter 2, in the case of DMBI-H derivatives, this process itself involves several steps, hydride transfer reaction, followed by an ET reaction.⁶² Secondly, the tight ion pairs dissociate to generate free charge carriers. Thus, achieving a high doping efficiency depends on both achieving a high-yielding reaction between the dopant and the

semiconductor and on minimizing electrostatic interactions between the dopant ions and the semiconductor ions, thus leading to low dissociation energies of CTCs.

The enhanced molecular n-doping for PTEG-1 is attributed to the effects of the polar environment offered by the triethylene glycol diether side chain on the electrostatic binding energy of the CTC: a higher dielectric constant medium will lower the energy of the CTCs and isolated dopant ion by a greater margin.¹²⁶

Inspired by this work, in this chapter a DMBI-H derivative with a triethylene glycol type side chain was synthesized. The idea was to investigate the impact of the polar side chain attached to the dopant rather than to the polymer on doping behavior at the molecular level. To that end, TEG-DMBI-H and MeO-DMBI-H were identified as target dopants that are expected to be electronically similar (with similar abilities as hydride donors), while differing in the polarity of their side chain, Figure 4.2.

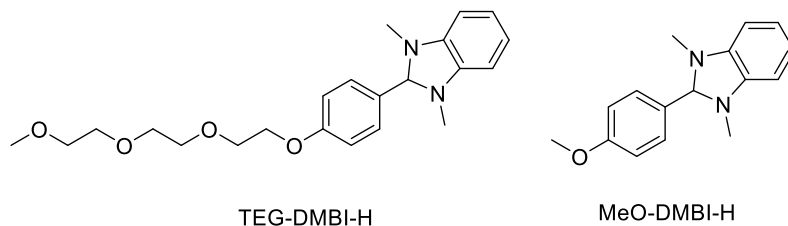


Figure 4.2 Structures of the dopants discussed in Chapter 5.

4.2 Synthesis of Dopants

Figure 4.3 shows the synthesis of the two dopants. MeO-DMBI-H was synthesized following a literature report from the reaction of 4-methoxybenzaldehyde and *N,N'*-dimethyl-1,2-phenylenediamine with 37% yield.⁵⁵ For synthesis of TEG-DMBI-H, 1-bromo-2-(2-(2-methoxyethoxy)ethoxy)ethane was reacted with 4-hydroxybenzaldehyde

in the presence of K_2CO_3 as a base to afford 4-(2-(2-(2-methoxyethoxy)ethoxy)ethoxy)benzaldehyde **4.1**.¹²⁷

4.1 was reacted with 1,2-phenylenediamine in the presence of $Na_2S_2O_5$ to obtain 2-(4-(2-(2-(2-methoxyethoxy)ethoxy)ethoxy)phenyl)-1*H*-benzo[*d*]imidazole **4.2**.

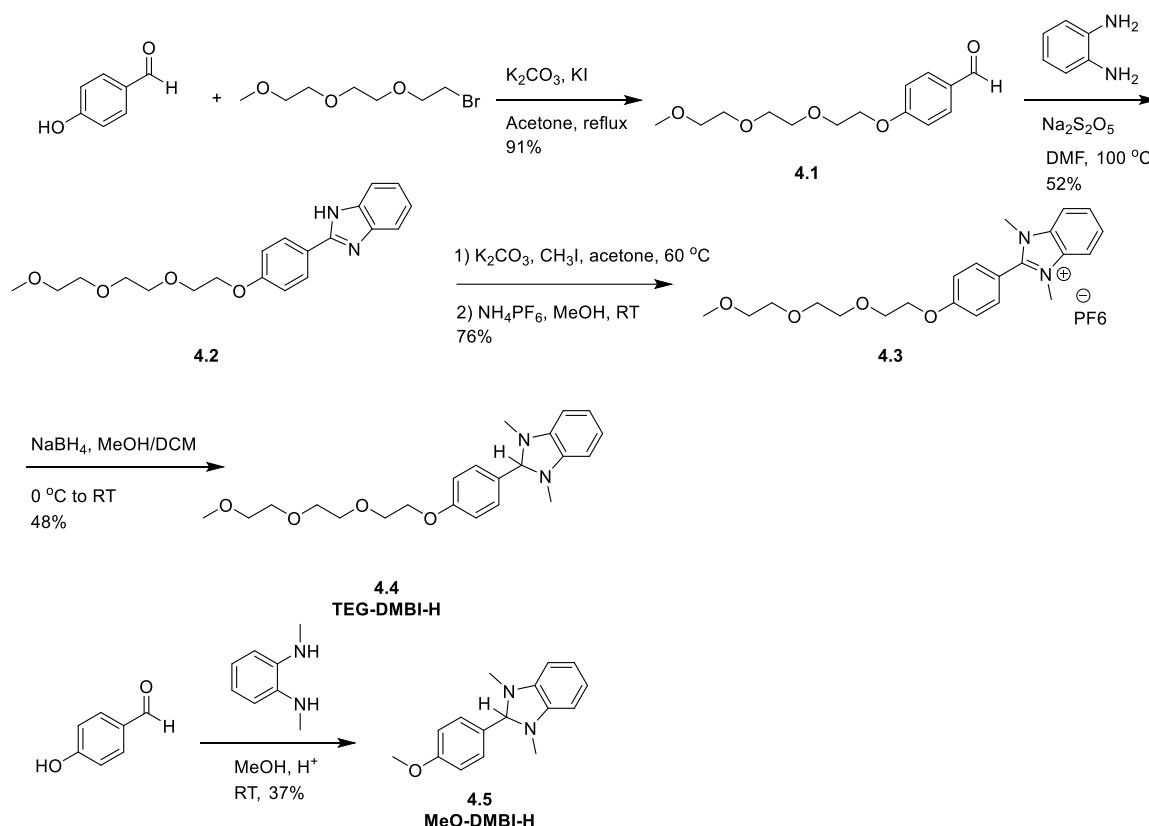


Figure 4.3 Synthesis routes for MeO-DMBI-H and TEG-DMBI-H.

Cation **4.3** was synthesized from the reaction of **4.2** and methyl iodide followed by anion exchange reaction with tetrabutylammonium hexafluorophosphate in MeOH to give the desired product **4.3** as off-white solid. TEG-DMBI-H was synthesized from the reaction of **4.3** and sodium borohydride in MeOH and was purified by column chromatography to give a pale-yellow oil with 48% yield.

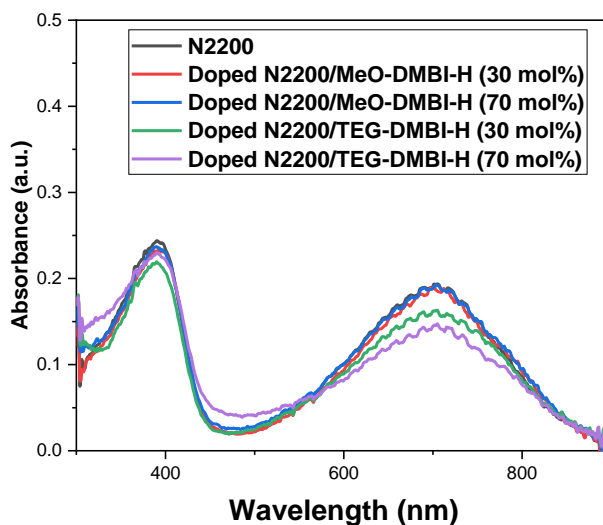


Figure 4.4 The UV–vis–NIR absorption spectra of pristine and doped N2200 with 30 and 70 mol% of MeO-DMBI-H and TEG-DMBI-H.

4.2.1 Characterization of doped N2200 using MeO-DMBI-H or TEG-DMBI-H using UV-vis-NIR

Figure 4.4 displays the UV–vis–NIR absorption spectra of thin films of pristine N2200 and doped N2200 using different mol ratios of TEG-DMBI-H or MeO-DMBI-H. Doped films were prepared by co-deposition of a solution of the polymer and each dopant by spin-coating (1000 rpm, 60 s) and annealing at 120 °C for 2 h. The main signal of neutral N2200 polymer at 690 nm was bleached to a greater extent using TEG-DMBI-H and more broadening and increasing of the absorbance around 500 nm was observed, suggesting

more generation of N2200 polarons, and thus, all things being equal, more carriers, than when using MeO-DMBI-H.

4.2.2 *Characterization of doped N2200 using MeO-DMBI-H or TEG-DMBI-H using electrical conductivity measurements.*

To characterize the electrical conductivities of the doped films, mixed solutions of N2200 and dopants (either MeO-DMBI-H or TEG-DMBI-H) were spin-coated on substrates (1000 rpm, 45 s), followed by deposition of narrow and parallel strip Au electrodes as the top contacts. The resultant devices were subjected to thermal annealing at 120 °C for 2 h.

The electrical conductivities of doped N2200 films were measured and the results are shown in Figure 4.5. It is worth mentioning that at least 5 devices were measured for each dopant level and the results shown here are the averages of those measurements.

The N2200 film exhibited an electrical conductivity of $7.5 \times 10^{-7} \text{ S cm}^{-1}$, which, as expected is low, and broadly consistent with a reported value ($2.0 \times 10^{-7} \text{ S cm}^{-1}$).¹²⁸ With 1 mol% of dopants a slight increase in the conductivities for N2200 films were observed (8.0×10^{-6} for MeO-DMBI-H doped-N2200 and $1.2 \times 10^{-6} \text{ S cm}^{-1}$ for TEG-DMBI-H doped-N2200). However, by adding 5 mol% of the dopant, the conductivity values decreased ($1.08 \times 10^{-6} \text{ S cm}^{-1}$ for polymer doped-MeO-DMBI-H and $8.9 \times 10^{-7} \text{ S cm}^{-1}$ for polymer doped-TEG-DMBI-H), while adding 10 and 20 mol% of each dopant led to additional increases in conductivity.

Table 4-1 conductivity values for doped N2200 polymer using MeO-DMBI-H and TEG-DMBI-H

Dopant mol ratio (%)	MeO-DMBI-H (S cm ⁻¹)	TEG-DMBI-H (S cm ⁻¹)
0 (Pristine N2200)	7.5×10^{-7}	7.5×10^{-7}
1	8.0×10^{-6}	1.2×10^{-6}
5	1.08×10^{-6}	8.9×10^{-7}
10	4.8×10^{-6}	7.9×10^{-6}
20	2.7×10^{-5}	7.4×10^{-5}

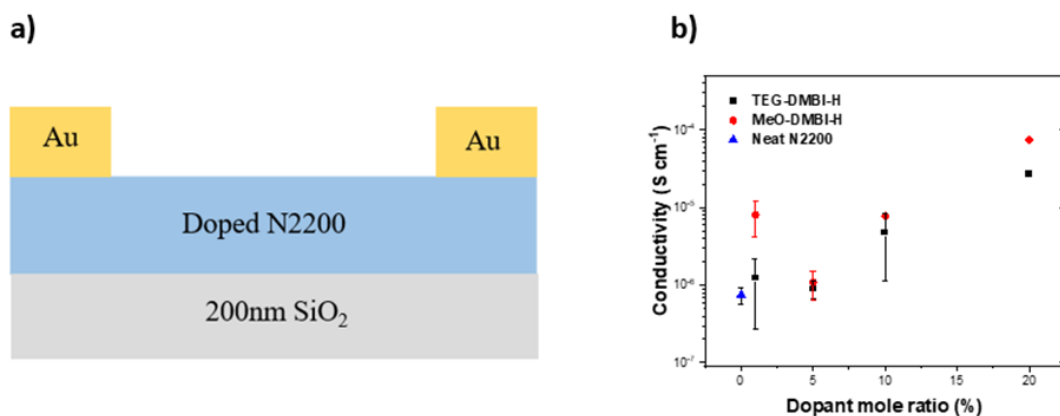


Figure 4.5 a) The architecture of the devices used for conductivity measurements and (b) The electrical conductivities for N2200 doped MeO-DMBI-H and TEG-DMBI-H at different mol ratios of the dopants.

4.2.3 Characterization of doped N2200 using MeO-DMBI-H or TEG-DMBI-H using charge density and mobility measurements

In the next step, charge carrier densities were measured with the architecture shown in Figure 4.5 (a).

A DC bias is applied across the device and causes the charge carriers to move towards or away from the SiO₂/polymer interface. This change is measured using an applied AC voltage. In fact, the charge carriers are gradually depleted by modulating DC voltage bias (V) from negative to positive. As a result, capacitance (C_p) starts to drop due to additional capacitance from the depleted active layer.

By plotting the reciprocal of C_p⁻² vs. voltage and fitting the linear regime, the charge density can be calculated using equation (4.1):

$$n = \frac{2}{\epsilon_0 \epsilon_r A^2 \frac{\partial C_p^{-2}}{\partial V}} \quad (4.1)$$

where e, ϵ_0 , ϵ_r , and A are an elementary charge, the dielectric constant of vacuum, the relative dielectric constant of the active layer and the active layer area.¹²⁵ For N2200, the relative dielectric constant was obtained from literature report ($\epsilon_r = 3$).¹²⁹ For all doped samples, the relative dielectric constant was assumed to be that previously reported for undoped N2200, i.e. the dopant ions were anticipated to have a relatively small effect on relative dielectric constant of the active layer.

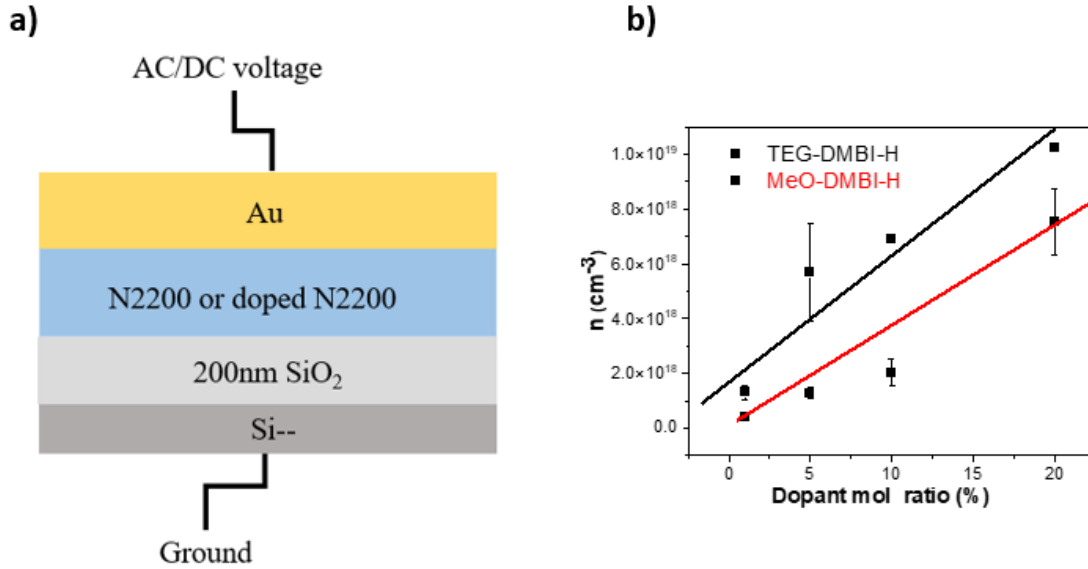


Figure 4.6 a) The architecture of the devices used for charge-carrier density measurements and b) The charge-carrier densities for N2200 doped with MeO-DMBI-H and with TEG-DMBI-H at different molar ratios of the dopants.

At it can be seen from Figure 4.6 (b), TEG-DMBI-H doped N2200 films showed higher carrier densities compared to MeO-DMBI-H doped N2200 and with increasing the dopant ratios, more charge carriers are generated.

The doping efficiency then was calculated as follows:¹³⁰

The doping concentration C is expressed in terms of molar ratio (MR) being the ratio of the number of dopant (n_D) to host (n_H) molecules:

$$C = \frac{n_D}{n_H} \quad (4.2)$$

The sum of host and dopant number densities gives the total number density of molecules n_{Mol} .

$$n_{Mol} = n_D + n_H \quad (4.3)$$

From equations (4.2) and (4.3) follows:

$$n_D = n_{Mol} \times \frac{C}{1+C} \quad (4.4)$$

In an intrinsic compound, n_{Mol} can be derived from the material's mass density ρ and molar mass M , together with Avogadro's constant N_{Avo} .

$$n_{Mol} = \frac{N_{Avo} \times \rho}{M} \quad (4.5)$$

For N2200, assuming a density of 1 g cm^{-3} and $M = 989.5 \text{ g mol}^{-1}$ yields a molecular density of $n_{Mol, N2200} = 6.08 \times 10^{20} \text{ cm}^{-3}$. In the following, the common assumption is that each dopant molecule substitutes one unit of the host polymer and hence n_{Mol} is unaltered upon doping.

In doped layers, n (charge carrier densities) is proportional to the number density of dopant molecules n_D and the doping efficiency η_{dop} :

$$\eta_{dop} = n \times \frac{1+C}{n_{Mol} \times C} \quad (4.6)$$

Table 4-2 Doping efficiency values for doped N2200 polymer using MeO-DMBI-H and TEG-DMBI-H.

Dopant mol ratio (%)	MeO-DMBI-H	TEG-DMBI-H
1	7%	22%
15	4%	19%
10	3%	12%
20	1%	1%

Therefore, based on equation (4.6), at 1 mol%, doping efficiencies of 7% and 22% were obtained for MeO-DMBI-H and TEG-DMBI-H, respectively. By increasing the doping ratio to 5 mol%, the doping efficiency stayed relatively the same, 4% and 19% for MeO-DMBI-H and TEG-DMBI-H but then it started decreasing for 10 and 20 mol% dopant level. One reason for doping efficiency to be low at 10 and 20 mol% doping levels could be the miscibility issues between dopant and host (N2200) that could lead to disruption of π - π stacking of N2200 polymer or aggregation of the dopant with itself. Furthermore, TEG-DMBI-H offered better doping efficiency compared to MeO-DMBI-H. A higher doping efficiency at lower doping level could be due to a higher charge transfer efficiency, presumably due to better miscibility of the dopant and polymer leading to more CTC formation. The second reason for the enhanced doping efficiency with the polar side chain may be related to the polar oligoethylene side chains that possess permanent dipoles. As the ionized dopant molecules are charged, the main barrier for creating a free charge carrier is the Coulomb force from the positive charge DMBI cation. The polar oligoethylene side chains contain permanent dipoles and those dipoles can potentially screen the electrostatic field of DMBI cation. Therefore, the ionized DMBI cation is stabilized by such a polarizable environment, which lets free charge carriers more easily be created.¹³¹

In the next step, field-effect mobility values were obtained for N2200 doped films; the results are summarized in Table 4.3. Pristine N2200 exhibited a field-effect mobility of $7 \times 10^{-3} \text{ cm}^2 \text{ V}^{-1} \text{ s}^{-1}$, consistent with a reported literature value.¹²³ By increasing the molar ratio of dopants, the field-effect mobility decreases such that for 5 mol% of dopant, it decreased to $8 \times 10^{-4} \text{ cm}^2 \text{ V}^{-1} \text{ s}^{-1}$ for MeO-DMBI-H and $2 \times 10^{-4} \text{ cm}^2 \text{ V}^{-1} \text{ s}^{-1}$ for TEG-DMBI-H; for dopant levels of 5 - 20 mol% the mobility remains fairly constant.

Table 4-3 Field-effect mobility measurements on N2200 doped using MeO-DMBI-H or TEG-DMBI-H.

Dopant mol ratio (%)	MeO-DMBI-H (cm ² V ⁻¹ s ⁻¹)	TEG-DMBI-H (cm ² V ⁻¹ s ⁻¹)
0 (Pristine N2200)	7×10^{-3}	7×10^{-3}
1	4×10^{-3}	3×10^{-3}
5	8×10^{-4}	2×10^{-4}
10	7×10^{-4}	2×10^{-4}
20	6×10^{-4}	-

4.2.4 Temperature dependence of the electrical conductivity of doped N2200 using MeO-DMBI-H or TEG-DMBI-H

Figure 4.7 (a) and (b) displays the temperature dependence of the electrical conductivity σ (T) in the doped layers. The temperature dependence of the conductivity in doped N2200 films can be well described by the classic Arrhenius equation, allowing determination of the hopping transport activation energy E_A simply by:

$$\sigma = \sigma_0 \times \exp \left[-\frac{E_A}{k_b T} \right] \quad (4.7)$$

where σ_0 is a pre-exponential, k_b is the Boltzmann constant, and T is the temperature. The activation energies were obtained, giving values of 0.39 eV for 1 mol% of MeO-DMBI-H and 0.27 eV for 1 mol% of TEG-DMBI-H. By increasing the mol ratio to 5 mol%, the E_A underwent a sudden decrease to 0.15 eV for MeO-DMBI-H and 0.14 eV for TEG-DMBI-H. As it has been discussed in Section 4.3.2, the electrical conductivity of doped N2200

also decreased using 5 mol% of each dopant. A low activation barrier implies a higher conductivity, however, given the obtained value for the conductivity at this doping level, this might suggest that the electronic coupling for in-plane charge hopping is relatively poor in this dopant level (5 mol%) compared to 1 mol%. By increasing the dopant ratio to 10 mol%, the E_A increased to 0.25 eV for MeO-DMBI-H and 0.27 eV for TEG-DMBI-H, while conductivity values also increased, perhaps suggesting that the electronic coupling associated with in-plane charge hopping increases again at these doping levels.

The slightly lower E_A value obtained for the dopant with a polar side chain (TEG-DMBI-H) at 1 mol% may potentially be attributable to the stabilization of the separated charges offered by the triethylene glycol diether side chain, consistent with the doping efficiency, which was estimated to be higher for this dopant than for MeO-DMBI-H.

Similar trends of E_A vs. doping were reported for electron transporting C_{60} n-doped with $[RuCp^*(mes)]_2$ and N2200 doped $[RuCp^*(mes)]_2$.^{132, 133} However, the doping ratio at which the E_A was minimized was reported to be less than 1 mol% in both of these studies. A decrease in E_A is observed with doping attributed to reduced trapping of charge carriers brought about by trap filling and the shift of the Fermi energy closer to the transport level, with concomitant increase in carrier density. However, in the case of doped N2200, 5 mol% dopant ratio is high to be considered as the concentration of dopant needed for trap filling. Moreover, the conductivity value is higher at 1 mol% compared to 5 mol%, that is not consistent with purely trap-filling effects.

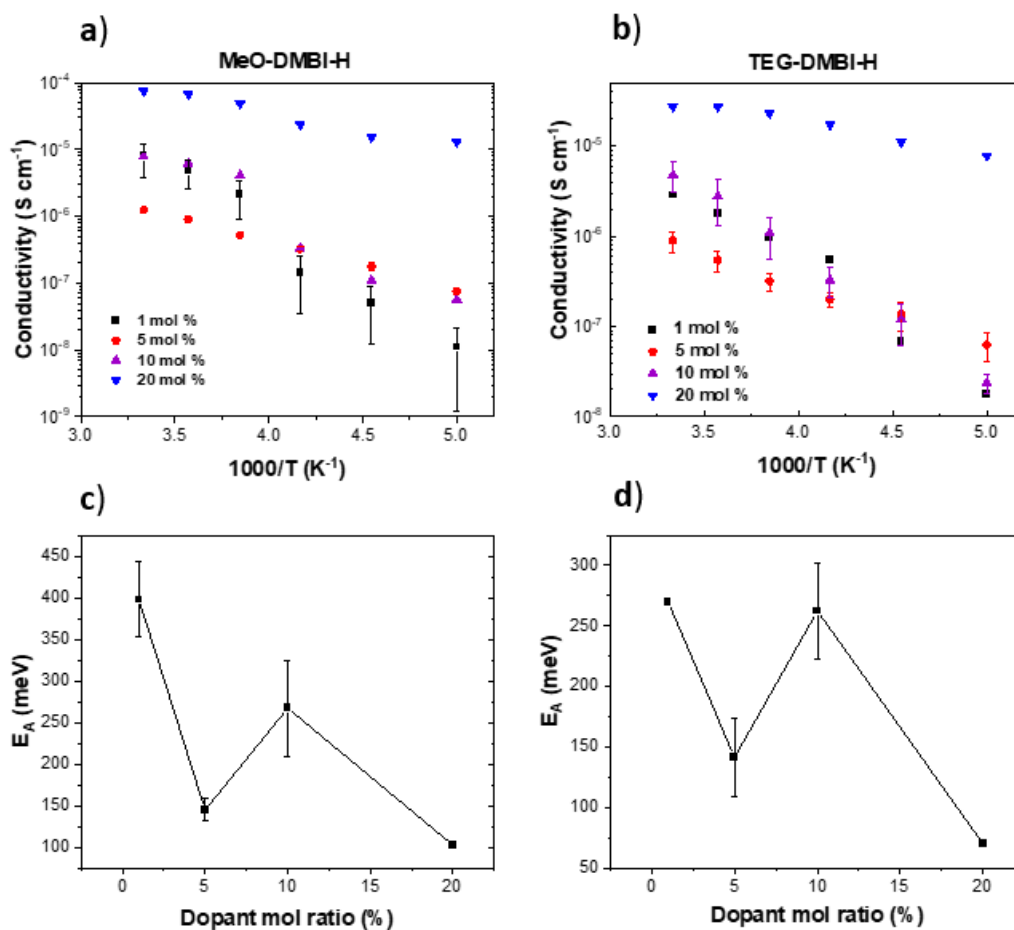


Figure 4.7 The plots of electrical conductivities of a) MeO-DMBI-H doped N2200, b) TEG-DMBI-H doped N2200 as a function of the inverse temperature, c) the plot of activation energy as a function of dopant mol ratios for Me-ODMBI-H and d) TEG-DMBI-H.

4.3 Grazing-incidence Wide-angle X-ray Scattering (GIWAXS)

Determination of the texture or the crystallographic lattice orientation distribution is crucial for understanding the correlation between the microstructure of OSCs and optoelectronic properties. Therefore, 2D-GIWAXS was applied to probe the morphology of the polymer as a function of dopant concentration in the present systems to examine whether the above-

mentioned variations in electrical characteristics could be correlated to structural changes, Figure 4.8.

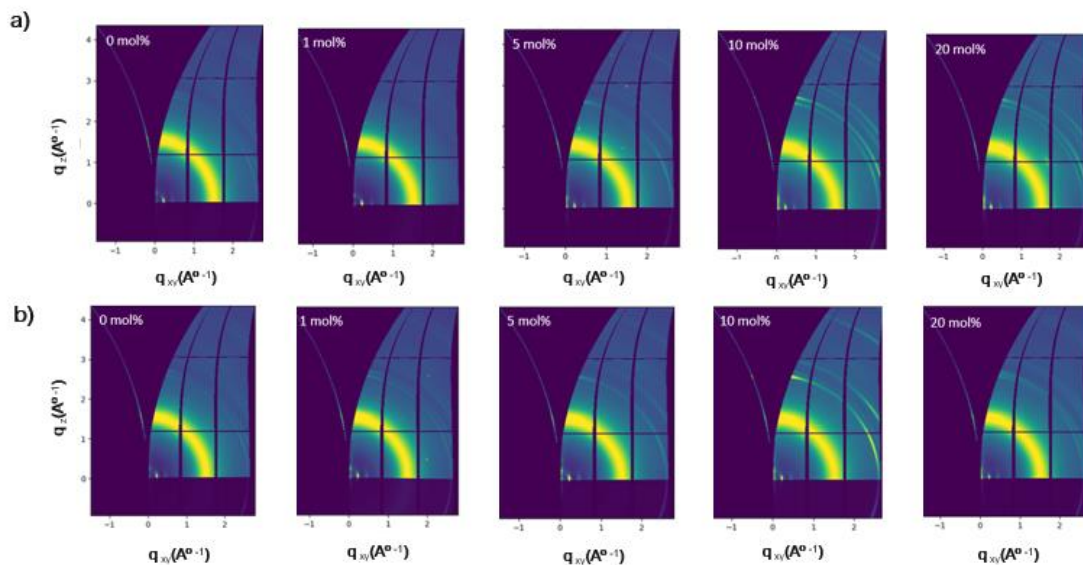


Figure 4.8 2D-GIWAXS patterns of pristine N2200 and doped N2200 with different mol ratios (0, 1, 5, 10, 20 mol%) of a) TEG-DMBI-H and b) MeO-DMBI-H.

1D-GIWAX linecuts of N2200 at different mol ratios of dopants are plotted in Figure 4.9 and 4.10. Upon doping of N2200 using MeO-DMBI-H or TEG-DMBI-H, no significant changes in the in-plane (IP) and out-of-plane (OOP) directions were observed for the π - π stacking. In the case of the lamellar stacking, no changes observed comparing the in-plane directions for TEG-DMBI-H and MeO-DMBI-H. Although a sudden increase [d-spacing] for dopant level of 20 mol% to 29 Å was observed, this was assumed to be an experimental artifact.

Furthermore, only minor changes were observed for the out-of-plane direction for TEG-DMBI-H, Figure 4.10, indicating no significant change in π - π stacking and lamellar

spacing and suggesting that the majority of dopants are located in the amorphous region of the polymer rather the crystalline region. Small change in the long-range organization with the introduction of the N-DMBI-H dopant is consistent with previous reports suggesting the dopants were located in the aggregated region.⁸⁴

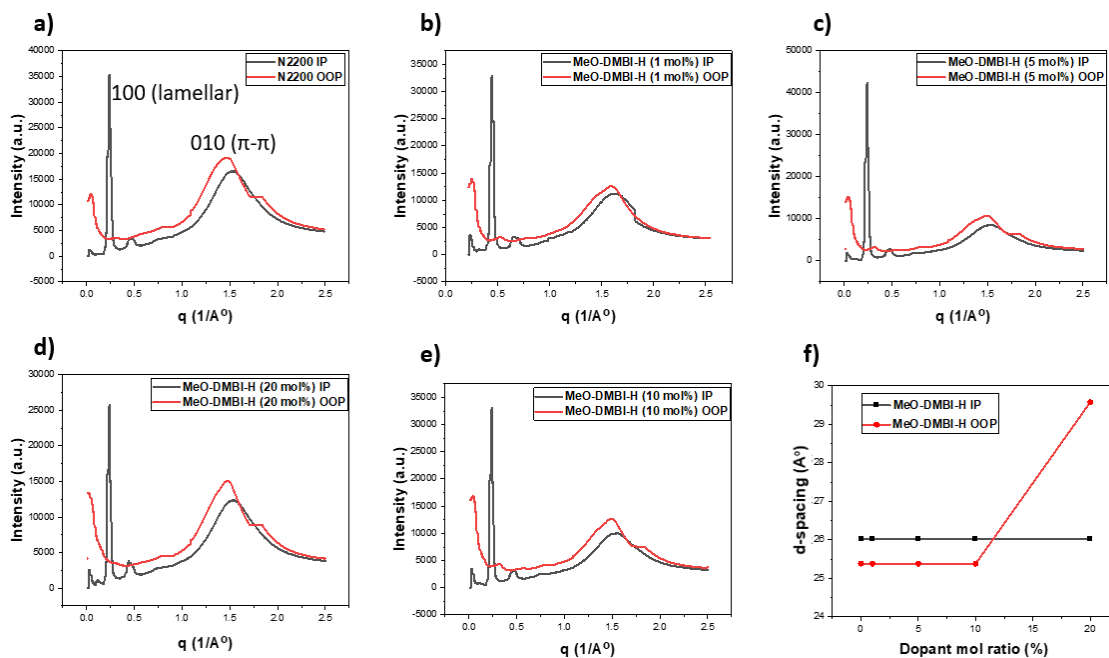


Figure 4.9 1D-GIWAXS linecuts of MeO-DMBI-H doped-N2200 at different dopant ratios, in-plane (IP) and out-of-plane (OOP) for lamellar distances.

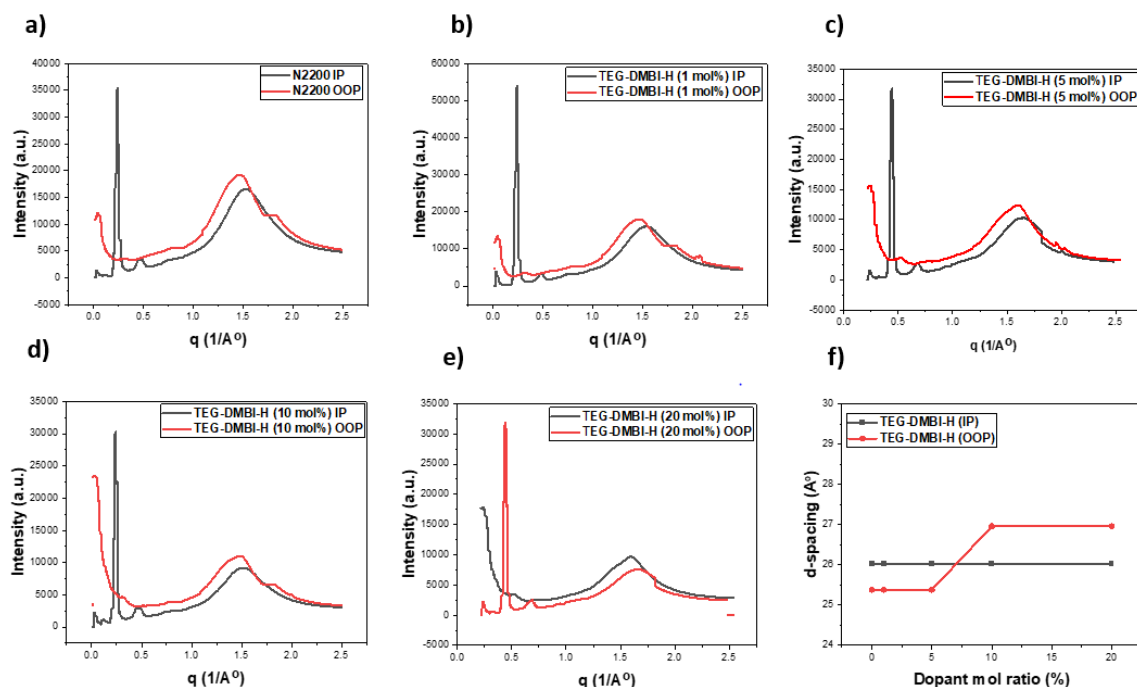


Figure 4.10 1D-GIWAXS linecuts of TEG-DMBI-H doped-N2200 at different dopant ratios, in-plane (IP) and out-of-plane (OOP) for lamellar distances.

To determine the texture orientations, the GIWAXS can be represented as a sector plot, where the scattering intensity is mapped as a function of the radial scattering vector and the polar angle (χ) (i.e. the angle between the scattering vector and the film surface).

The background corrected and normalized scattering intensities of the lamellar stacking peaks were integrated over $\chi = [0^\circ, 90^\circ]$, and total integrated areas are compared between samples of N2200 with different ratios of dopants, Figure 4.11.

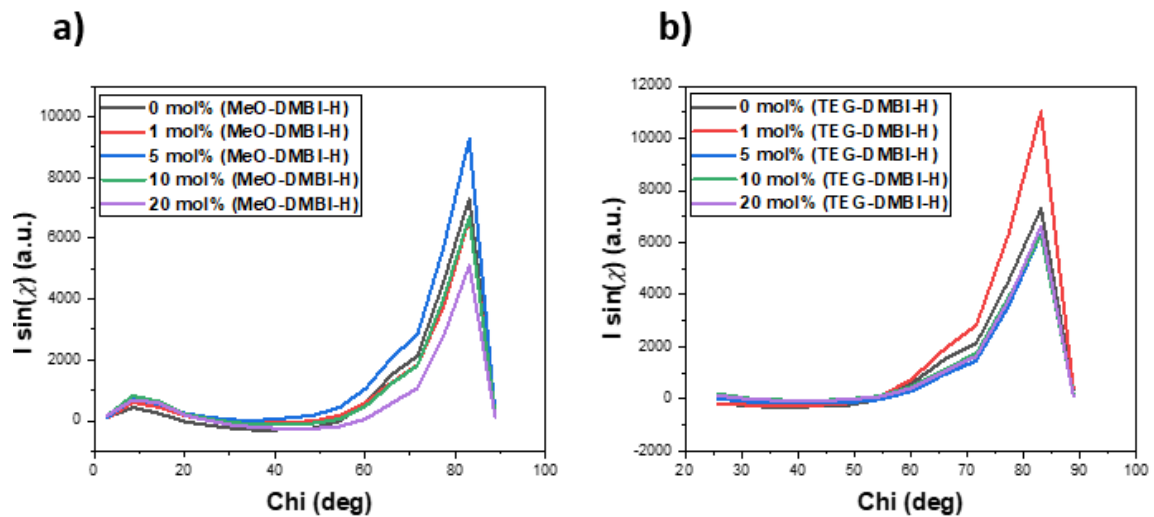


Figure 4.11 Relative degree of crystallinity (rDOC) from the integrated (lamella) pole figure.

MeO-DMBI-H doped N2200 (5 mol% doping ratio) showed a significant increase in out of plane lamellar scattering, implying more preferred face-on orientation compared with pristine N2200 and 10 mol% doped polymers. For 20 mol%, more edge-on orientation was observed.

In the case of TEG-DMBI-H, 1 mol% showed more face-on orientation compared to 5 mol%. In general, GIWAXS data suggests that in low dopant ratios (1 and 5 mol%), face-on orientation is dominant and with increasing dopant ratios, the edge-on orientation become to increase. This observation is consistent with field-effect mobility measurements, as the mobility values decreased for 1 and 5 mol% of dopants, Table 4.1, as well as with the low conductivity for N2200 doped with MeO-DMBI-H at 5 mol% ratio.

Moreover, as it can be seen from GIWAXS raw data, Figure 4.8, the π - π scattering intensity, suffers from a large background scattering (scattering from the glass substrate) and therefore, additional measurements on silicon substrate may yield higher quality data and permit a more detailed analysis.

It is also worth mentioning that morphological changes and rearrangement from face- to edge-on orientation upon doping for N-DMBI-H doped N2200 has been recently reported.¹³⁴

4.4 Summary and Conclusion

To study the effect of a polar triethylene glycol diether side chain on doping behavior of DMBI-H derivatives, two dopants, MeO-DMBI-H and TEG-DMBI-H were synthesized. Electrical conductivity measurements on MeO-DMBI-H doped N2200 at different mol ratios of dopant showed higher values while the TEG-DMBI-H doped N2200 showed higher charge carrier densities. The increased charge density for TEG-DMBI-H values may be attributable to the effect of the polar environment offered by the triethylene glycol diether side chain, as it could help to overcome the electrostatic interaction between the DMBI cation species and the NDI radical anions ($\text{NDI}^{\bullet-}$) to facilitate transport. The conductivity values decrease for both dopants (but to a greater extent for MeO-DMBI-H) at 5 mol% ratio and field-effect mobility was also found to be lower at 5 mol% as well. GIWAXS data also showed rearrangement from edge- to face-on orientation at low doping concentration that could explain the decrease in measured mobility for doped N2200. The activation energies for charge transport conductivities were extracted from the temperature

dependence of the electrical conductivity at different loading ratios of dopants, suggesting a lower activation energy when N2200 was doped using 5 mol% of each dopant.

At this stage, there is no clear explanation for drop of activation energy at 5 mol% doping ratios. The smaller activation energy at 5 mol% indicated a larger population of charge carriers filling the tail of the density of states.¹²² Further investigation is required and will be discussed in Chapter 5.

In general, in-plane conductivity measurements is potentially a complex quantity to understand as the mobility depends on many factors including the crystallinity of the polymer. The presence of dopants and dopant ions might affect the crystallinity and the order. Moreover, the mobility is anisotropic and so different orientational preferences (face or edge-on) for different dopant:polymer blends can impact electrical measurements.

4.5 Experimental Details

4.5.1 Synthesis

Chemicals were obtained from commercial sources and used as received unless stated otherwise. N2200 polymer was purchased from Polyera (Lot: CZH-XV-77-22). All operations involved in synthesis were performed under an atmosphere of nitrogen using standard Schlenk techniques or in a glove box. ¹H-NMR and ¹³C-NMR spectra were recorded in CDCl₃ or C₆D₆, spectrometers. The chemical shifts (δ) are reported in parts per million (ppm).

Synthesis of 4-(2-(2-(2-methoxyethoxy)ethoxy)ethoxy)benzaldehyde (4.1)

As per the reported procedure,¹²⁷ 1-bromo-2-(2-(2-methoxyethoxy)ethoxy)ethane (9.66 g, 42.5 mmol), K₂CO₃ (6.8 g, 49.3 mmol), KI (200 mg, 1.2 mmol) and 4-hydroxybenzaldehyde (4.0 g, 32.73 mmol) was suspended in 150 mL acetone. A reflux condenser was installed, and the mixture was bubbled with nitrogen for 10 min. The mixture was stirred and refluxed for 24 h. After the mixture was cooled to room temperature, it was filtered, concentrated under reduced pressure, and loaded onto column chromatography (1:1 hexanes/EtOAc) to yield the desired product as pale-yellow oil (8.0 g, 91%). ¹H NMR (500 MHz, CDCl₃) δ 9.87 (s, 1H), 7.84 (d, *J* = 7.5 Hz, 2H), 7.03 (d, *J* = 7.5 Hz, 2H), 4.24 – 4.17 (m, 2H), 3.90 – 3.85 (m, 2H), 3.76 – 3.72 (m, 2H), 3.70 – 3.66 (m, 2H), 3.66 – 3.61 (m, 2H), 3.56 – 3.52 (m, 2H), 3.36 (s, 3H). ¹³C{¹H} NMR (126 MHz, CDCl₃) δ 190.97, 163.96, 132.07, 130.14, 114.99, 72.02, 71.00, 70.75, 70.68, 69.58, 67.85, 59.16. HRMS (ESI) calcd for C₁₄H₂₁O₅ (M+H⁺), 269.1384; found 269.1381.

Synthesis of 2-(4-(2-(2-(2-methoxyethoxy)ethoxy)ethoxy)phenyl)-1*H*-benzo[*d*]imidazole (4.2)

To a two neck 100 ml round bottom flask with stir bar, 4-(2-(2-(2-methoxyethoxy)ethoxy)ethoxy)benzaldehyde (5.18 g, 19.3 mmol), 1,2-phenylenediamine (2.10 g, 19.41 mmol) and sodium metabisulfite (3.67 g, 19.3 mmol) were added and a reflux condenser was installed. DMF (50 mL) was added, and the solution was bubbled with nitrogen for 10 min and then heated at 100 °C overnight. Water was added and the organic phase extracted with CH₂Cl₂ (2 × 100 mL). The combined organic phase was washed with brine two times and solvent evaporated to obtain solid. The solid was

dissolved in 100 mL boiling EtOAc and precipitated by adding hexane. The product was isolated by filtration and dried under high vacuum to obtain a yellow solid (4.5 g, 52%). ^1H NMR (500 MHz, CDCl_3) δ 8.07 – 7.96 (m, 2H), 7.60 – 7.48 (m, 2H), 7.15 (m, 2H), 6.81 – 6.69 (m, 2H), 3.95 (m, 2H), 3.76 – 3.71 (m, 2H), 3.69 – 3.63 (m, 4H), 3.63 – 3.58 (m, 2H), 3.51 – 3.47 (m, 2H), 3.27 (s, 3H). $^{13}\text{C}\{^1\text{H}\}$ NMR (126 MHz, CDCl_3) δ 160.40, 139.25 – 138.59 (bro), 128.50, 122.73, 115.00, 114.92, 71.92, 70.87, 70.73, 70.62, 69.67, 67.42, 59.00. HRMS (ESI) calcd for $\text{C}_{20}\text{H}_{25}\text{N}_2\text{O}_4$ ($\text{M}+\text{H}^+$), 357.1809; found 357.1796. Anal Calcd. For $\text{C}_{20}\text{H}_{24}\text{N}_2\text{O}_4$: C, 67.40; H, 6.79; N, 7.87, Found C, 67.40; H, 6.73; N, 7.93.

Synthesis of 2-(4-(2-(2-(2-methoxyethoxy)ethoxy)ethoxy)phenyl)-1,3-dimethyl-1H-benzo[d]imidazol-3-ium hexafluorophosphate (4.3)

To a 100 mL two-neck flask with a reflux condenser under nitrogen, 2-(4-(2-(2-(2-methoxyethoxy)ethoxy)ethoxy)phenyl)-1H-benzo[d]imidazole (4.50 g, 12.3 mmol), K_2CO_3 (17.0 g, 123 mmol, 10.0 equivalent) added follow by addition of acetone (50.0 mL). The flask was capped with a septum and flushed with nitrogen gas for 5 min. Iodomethane (15.0 mL, 240.8 mmol) added by a syringe and the reaction mixture stirred at 60 °C for 12 h. After cooling down the reaction mixture to room temperature, the solid was filtered and rinsed with acetone. The solvent evaporated to yield a yellow solid (6.6 g, 12.8 mmol). The solid was dissolved in anhydrous MeOH (70.0 mL) and ammonium hexafluorophosphate (2.10, 12.8 mmol) was added. After stirring for 30 min, a white precipitate was formed, which was filtered and dried over high vacuum to yield an off-white solid (5.0 g, 76%). ^1H NMR (500 MHz, CD_3OD) δ 7.98 (m, 2H), 7.84 – 7.79 (m, 2H), 7.75-7.67 (m, 2H), 7.38 – 7.32 (m, 2H), 4.37 – 4.26 (m, 2H), 3.98 (s, 6H), 3.97 – 3.90 (m, 2H), 3.78 – 3.72 (m, 2H), 3.59 – 3.52 (m, 2H), 3.37 (s, 3H). $^{13}\text{C}\{^1\text{H}\}$ NMR (126 MHz, CD_3OD) δ 164.07, 152.26,

133.81, 133.53, 128.08, 116.95, 114.12, 113.80, 72.92, 71.75, 71.52, 71.34, 70.55, 69.27, 59.11, 33.57. HRMS (ESI) calcd for C₂₂H₂₉N₂O₄ (M-PF₆⁺), 385.2121; found 385.2107.

Synthesis of 2-(4-(2-(2-(2-methoxyethoxy)ethoxy)ethoxy)phenyl)-1,3-dimethyl-2,3-dihydro-1*H*-benzo[*d*]imidazole (TEG-DMBI-H, 4.5)

2-(4-(2-(2-(2-methoxyethoxy)ethoxy)ethoxy)phenyl)-1,3-dimethyl-1*H*-benzo[*d*]imidazol-3-ium hexafluorophosphate (2.0 g, 3.77 mmol) was dissolved in 20 mL anhydrous CH₂Cl₂ and 20 mL anhydrous methanol added. Sodium borohydride (837 mg, 22.0 mmol, 5.84 equivalent) was added in 10 portions. The reaction mixture was stirred at room temperature for 12 h. To the reaction mixture, water was added, and the mixture was extracted with CH₂Cl₂ two times. The organic phase was dried over MgSO₄, filtered, and evaporated to afford a viscous oil, which was purified using silica-gel column chromatography (5:1 CH₂Cl₂/EtOAc) to yield a pale-yellow oil (700 mg, 48%). ¹H NMR (700 MHz, C₆D₆) δ 7.41 – 7.36 (m, 2H), 6.89 – 6.85 (m, 2H), 6.85 – 6.81 (m, 2H), 6.41 – 6.38 (m, 2H), 4.59 (s, 1H), 3.77 – 3.74 (m, 2H), 3.57 – 3.52 (m, 2H), 3.49 – 3.45 (m, 6H), 3.37 – 3.32 (m, 2H), 3.12 (s, 3H), 2.30 (s, 6H). ¹³C{¹H} NMR (176 MHz, C₆D₆) δ 160.37, 142.69, 131.75, 130.50, 119.85, 114.74, 106.14, 94.11, 72.40, 71.19, 71.09, 70.95, 69.90, 67.71, 58.70, 32.98. HRMS (ESI) calcd for C₂₂H₃₀N₂O₄ (M+H⁺), 387.2278; found 387.2269. Anal Calcd. For C₂₂H₃₀N₂O₄: C, 68.37; H, 7.82; N, 7.25, Found C, 68.67; H, 7.86; N, 7.29.

Synthesis of 2-(4-methoxyphenyl)-1,3-dimethyl-2,3-dihydro-1*H*-benzo[*d*]imidazole (MeO-DMBI-H, 4.4)

As per the reported procedure,⁵⁵ two drops of acetic acid were added to a mixture of the 4-methoxybenzaldehyde (1.0 g, 7.34 mmol), *N,N'*-dimethyl-1,2-phenylenediamine (1.0 g,

7.3 mmol), and methanol (6.0 mL) and the mixture was stirred vigorously. Precipitation was observed within 1 h. The crude product was collected by filtration. The solids were then recrystallized twice from methanol to obtain white crystals (700 mg, 37%). NMR spectra were consistent with what was reported in the literature. ^1H NMR (500 MHz, CDCl_3) δ 7.58 – 7.47 (m, 2H), 7.02 – 6.92 (m, 2H), 6.76-6.73 (m, 2H), 6.48-6.46 (m, 2H), 4.86 (s, 1H), 3.87 (s, 3H), 2.58 (s, 6H). $^{13}\text{C}\{^1\text{H}\}$ NMR (126 MHz, CDCl_3) δ 160.59, 142.23, 131.14, 130.14, 119.37, 113.96, 105.80, 93.72, 55.47, 33.19.

4.5.2 Characterizations: general procedures and experimental details

All stock solutions were prepared under nitrogen atmosphere in an inert gas box using dried chlorobenzene (CB). The stock solutions were stirred overnight in order to enable complete dissolution of the materials.

The reported dopant concentration of 5 mol% is given as $c = \frac{N_D}{N_D + N_P}$, where N_D is the number of dopant molecules and N_P is the number of polymer monomer units as contained in the solutions. Thin films were prepared via spin-coating. Therefore, a standard laboratory spin-coater was used at 1000 rpm for 45 s. Thermal activation was performed by annealing the doped thin films at 120 °C for 2 h on a hot plate in the glovebox, if not otherwise stated.

Optical absorption spectroscopy was performed using a Cary 5000 UV–vis-NIR spectrometer. Undoped and doped thin films were prepared on glass substrates with thickness between 20 and 80 nm.

The conductivity measurements were conducted in LakeShore TTPX probe station using an Agilent 4155C parameter analyzer. Capacitance measurements (used to evaluate the charge density) were performed in the same LakeShore TTPX probe station using an Agilent E4980A Precision LCR Meter.

Grazing incidence wide angle X-ray scattering (GIWAXS) measurements were performed at the Stanford Synchrotron Radiation Lightsource (SSRL) beamline 11–3 with an X-ray wavelength of 0.9752 Å and sample-to-detector distance of 321 mm at an incident angle of 0.14°. Measurements were carried out using a helium-filled sample chamber to reduce air scattering background. The 2DGIWAXS patterns were collected with a 2D CCD X-ray detector (MX225, Rayonix, L.L.C) with a pixel size of 73.2 μm (3072 × 3072 pixels).

CHAPTER 5: EFFECTS OF CROSSLINKING AND DOPANT SUSBTITUENTS: CONCLUSIONS, FUTURE WORK AND CONTRIBUTIONS

5.1 Overview

This thesis focused on developing new strategies to minimize the diffusion of n-type dopants in semiconductors by modification of some of the well-studied dopants in the literature, as well as improving the charge-carrier densities obtained upon doping of organic semiconductors.

As discussed multiple times in this thesis, DMBI-H derivatives have been extensively used for the n-doping of numerous organic semiconductors for various applications.⁵⁷⁻⁶¹ However, there are few studies and investigations that address the immobilization in order to minimize their diffusion rate and migration in the device stacks.⁸²

In Chapter 2 of this thesis an oligomeric DMBI-H derivative in which 4 units of DMBI-H units are linked together via an sp^3 carbon was synthesized. This dopant (tetrakis-O-DMBI-H) was found to n-dope the electron-transporting polymers N2200 and TBDOPV-T as well as small molecule electron acceptor, PCBM. PCBM doped-tetrakis-O-DMBI-H (10 mol%) showed a conductivity value of 0.14 S cm^{-1} but exhibited low film resistance to o-DCB.

Regarding doping of polymers using (tetrakis-O-DMBI-H), although, the doped N2200 films showed very low resistance toward solvent, a heated tetrakis-O-DMBI-H-doped-TBDOPV-T film exhibited good resistance to o-DCB. The solvent resistance of the doped

TBDOPV-T film is ascribed to strong electrostatic interactions between multiply charged cations and the negatively charged polymer chains.

The electrical conductivity of 9 mol% tetrakis-O-DMBI-H-doped-TBDOPV-T was obtained to be 15 S cm^{-1} . The doped films were also characterized using UPS and a significant decrease in sample work function was observed. Furthermore, the valence band shifts to higher binding energy after doping, which is related to an increase in electron density near the Fermi level. The diffusion of dopant molecules/ions and the associated charge carriers in doped films have also been examined; no evidence was found for the diffusion from a tetrakis-O-DMBI-H-doped-TBDOPV-T film into a N2200, an observation that may be due both to the same strong dopant ion:polymer interactions responsible for increased solvent-exposure resistance and to the large size of the dopant ions.

Chapter 3 discussed thermal crosslinking as a second approach for immobilization of DMBI-H derivatives. The introduction of a butoxy group on the four membered ring of benzocyclobutane moiety is known to significantly lower the temperature at which the electrocyclic ring opening reaction responsible for cross-linking takes place (120°C). Two new derivatives of DMBI-H and a new fullerene derivative with pendant butoxybenzocyclobutene (BBCB) groups were synthesized and characterized, (BBCB-DMBI-H, BBCB-N-DMBI-H and BBCBPCB). BBCBPCB could thermally crosslink in the range of $120^\circ\text{C} - 150^\circ\text{C}$. DSC showed an exothermic peak attributed to the ring opening of cyclobutene moiety. UV-vis experiments showed high retention of thermally annealed films on exposure solvents including o-DCB.

The doping products of the DMBI-H derivatives and BBCBPCB were characterized using MALDI-TOF-MS and EPR. Mass spectrometry established the formation of heterodimer and EPR showed the signal for formation of PCB radical anion. UV-vis experiment also represented the high film retention to o-DCB for BBCB-DMBI-H doped BBCBPCB. Diffusion of dopant molecules was investigated by evaporation of 2CN-NDI on the top of BBCB-N-DMBI-H doped BBCBPCB. No evidence was found for the diffusion from a thermally treated BBCB-N-DMBI-H-doped-BBCBPCB film into 2CN-NDI layer – in contrast to what is seen in a non-crosslinked film, an observation that may be due to the covalent crosslinking of dopant to the host (in this case PCB) that prevents movement and diffusion of the dopants and dopant ions.

Chapter 4 investigated modification of DMBI-H derivatives and the impact of the polar side chain attached to the dopant rather than to the polymer on doping behavior in molecular level. For that purpose, TEG-DMBI-H and a non-TEG compound MeO-DMBI-H were identified and synthesized. Both dopants were expected to be electronically similar while differing in the polarity of their side chain.

In-plane electrical conductivity measurements on N2200 doped films at different mol ratios of each dopants showed that MeO-DMBI-H affords slightly higher conductivity values than TEG-DMBI-H. Interestingly, the conductivity values with incorporation of 5 mol% dopant (for both dopants) were recorded to be lower compared to 1 and 10 mol% of the dopant ratios. Moreover, field-effect mobility measurements represented lower mobility values for 5 mol% of each dopant.

Temperature dependence of the electrical conductivity demonstrated lower activation energy when N2200 was doped using 5 mol% dopant. Taking this data into account and the fact that the electrical conductivity values were established to be lower at this ratio (for both dopants), weak electrical coupling for in-plane charge transport, perhaps due to changes in the orientation, could potentially explain this observed behavior. To investigate this hypothesis, GIWAXS measurements established morphological changes to face-on orientations at low doping ratios that are consistent with the observation of a low mobility obtained for TEG-DMBI-H-doped-N2200 at 5 mol% ratio. However, it is unclear why the activation energy is decreasing for 5 mol% of dopant ratios.

5.2 Future Work

Chapter 2 suggests a possible means of fabricating multilayer structures from solution and to restrict diffusion of dopants ions from intentionally doped regions of devices to other portions where doping is not needed. More dopant:polymer combinations should be investigated to establish the generality and limitations of the approach.

This approach, on the other hand, has failed for insolubilization of doped films of small molecule acceptors such as PCBM without impeding the charge transport behavior.

One approach that can be taken in future, is studying the diffusion behavior of tetrakis-O-DMBI-H doped thermo-crosslinkable BBCBPCB; this combination might take advantages of both electrostatic interactions and crosslinking and formation of a dense matrix that prevents the diffusion of dopant and dopant ions into small molecule acceptors. This approach might offer insolubilization of dopant with acceptable charge-transport behavior

(even at lower mole ratio of dopants (less than 10 mol%)), as large and 3D size of dopant had shown to negatively impact the film morphology.

Furthermore, the concept of electrostatic crosslinking may not be favored for OSCs with high crystallinity as a large multiple cation species might lead to more structural disruption. In fact, these heavily charged species may serve as deeper traps for carrier densities.

Chapter 3 also suggests another approach (using thermo-crosslinkable units on DMBI-H and PCB derivatives) for the purpose of fabricating multilayer structures from solution and to restrict diffusion of both dopants and dopant ions.

Currently, there is no information available regarding the impact of crosslinking on charge transport behavior of doped systems. Conductivity measurement on BBCBPCB and BBCB-N-DMBI-H could offer valuable information to compare it with values already reported for N-DMBI-H doped- PCBM. The crosslinking might interfere with the intermolecular packing and thus negatively affect the charge carrier transport.¹³⁵

Moreover, the diffusion of dopant and dopant ions can be studied under applied field as there are literature reports on diffusion of dopants under applied field.^{34, 82} In fact, upon application of sufficiently high electric fields, the dopant positive ions start to drift toward the negative electrode, in opposite direction to the polaron current. Consequently, a dedoped region is generated, which exhibits a much larger resistivity compared to the doped region. Hence, the voltage drop no longer occurs linearly over the whole channel, but mostly over the dedoped region and at the dedoped electrode contact. If the diffusion of dopant ions is minimized by thermal crosslinking, then for the crosslinked doped film, the I-V curve is linear (or close to linear), compared to non-crosslinked doped films.

It also worth mentioning that the BBCB functional group that is capable of crosslinking at 120 °C, requires multi-step synthesis procedures with moderate yields¹¹⁸ that will increase the cost of modified dopant for practical applications. More synthetic investigation could be done to access the BBCB in fewer steps and higher yields.

To compare the approaches presented in Chapter 2 and 3, the immobilization via electrostatic interactions just limits the diffusion of dopant ions while the immobilization via covalent interactions, immobilize both the dopants and dopant ions that could potentially be more beneficial to increase the device stability.

Chapter 4 was intended to get some insight into charge transport behavior by application of a triethylene glycol type side chain on a DMBI-H derivative. Doping of N2200 with these two dopants provided some new insights into charge transport behavior, orientations and morphology of doped films. As it was mentioned, 5 mol% dopant ratios, offered low activation energy, low conductivity value, and low mobility.

The temperature dependence of the charge carrier density and mobility could offer some more insights into doping process and how the activation energy of charge hopping differ in different doping levels.^{123, 125} Moreover, a closer look into morphological changes including the changes in π - π stacking and aggregation could be helpful, using AFM.

5.3 Broader Impact of the Work Discussed in This Thesis

Based on the data presented in this thesis, it appears that both crosslinking using covalent bond formations and electrostatic interactions seems to be promising strategies to minimize the diffusion of DMBI-H derivatives in solid state films. These materials can be applied in

solar cell devices to investigate their impacts on stability and durability of solar cells. Furthermore, solution fabrication of multilayer devices is often challenging, in that deposition of a second layer can lead to partial dissolution of the first layer. Combinations of BBBCBPCB and BBBCB-N-DMBI-H can potentially be used as electron transport layers for efficient charge extraction in perovskite solar cells (PSCs). Insolubilization of the electron transport layer subsequent to deposition is an effective approach that have been used to increase the mechanical and thermal stability of the material, and to permit solution deposition of additional layers in perovskite solar cells.¹³⁶ However, the insolubilization processed required high temperature (200 °C and higher) that is not optimal for stability of solar cells.

Moreover, the concept of the crosslinking using BBBCB functional groups can be applied to hole transport materials in perovskite solar cells to decrease the diffusion rate of p-dopants and insolubilization for solution fabrication of multilayer devices.¹³⁷

REFERENCES

1. Reineke, S., Complementary LED technologies. *Nat. Mater.* **2015**, *14* (5), 459-462.
2. Wu, X. H.; Mao, S.; Chen, J. H.; Huang, J., Strategies for Improving the Performance of Sensors Based on Organic Field-Effect Transistors. *Adv. Mater.* **2018**, 1705642.
3. Myny, K.; Steudel, S.; Smout, S.; Vicca, P.; Furthner, F.; van der Putten, B.; Tripathi, A. K.; Gelinck, G. H.; Genoe, J.; Dehaene, W.; Heremans, P., Organic RFID transponder chip with data rate compatible with electronic product coding. *Org. Electron.* **2010**, *11* (7), 1176-1179.
4. Wang, Y.; Zhang, J.; Zhang, S.; Huang, J., OFET chemical sensors: Chemical sensors based on ultrathin organic field-effect transistors. *Polym. Int.* **2021**, *70* (4), 414-425.
5. Malinkiewicz, O.; Yella, A.; Lee, Y. H.; Espallargas, G. M.; Graetzel, M.; Nazeeruddin, M. K.; Bolink, H. J., Perovskite solar cells employing organic charge-transport layers. *Nat Photonics.* **2014**, *8* (2), 128-132.
6. Jeong, J.; Kim, M.; Seo, J.; Lu, H.; Ahlawat, P.; Mishra, A.; Yang, Y.; Hope, M. A.; Eickemeyer, F. T.; Kim, M.; Yoon, Y. J.; Choi, I. W.; Darwich, B. P.; Choi, S. J.; Jo, Y.; Lee, J. H.; Walker, B.; Zakeeruddin, S. M.; Emsley, L.; Rothlisberger, U.; Hagfeldt, A.; Kim, D. S.; Grätzel, M.; Kim, J. Y., Pseudo-halide anion engineering for α -FAPbI₃ perovskite solar cells. *Nature* **2021**, *592* (7854), 381-385.
7. Bubnova, O.; Crispin, X., Towards polymer-based organic thermoelectric generators. *Energy Environ. Sci.* **2012**, *5* (11), 9345-9362.
8. Beretta, D.; Neophytou, N.; Hodges, J. M.; Kanatzidis, M. G.; Narducci, D.; Martin-Gonzalez, M.; Beekman, M.; Balke, B.; Cerretti, G.; Tremel, W.; Zevalkink, A.; Hofmann, A. I.; Muller, C.; Dorling, B.; Campoy-Quiles, M.; Caironi, M., Thermoelectrics: From history, a window to the future. *Mater. Sci. Eng. R Rep.* **2019**, *138*, 210-255.

9. Du, Y.; Xu, J. Y.; Paul, B.; Eklund, P., Flexible thermoelectric materials and devices. *Appl. Mater. Today*. **2018**, *12*, 366-388.
10. Petsagkourakis, I.; Tybrandt, K.; Crispin, X.; Ohkubo, I.; Satoh, N.; Mori, T., Thermoelectric materials and applications for energy harvesting power generation. *Sci. Technol. Adv. Mater.* **2018**, *19* (1), 836-862.
11. Heo, J. S.; Eom, J.; Kim, Y. H.; Park, S. K., Recent Progress of Textile-Based Wearable Electronics: A Comprehensive Review of Materials, Devices, and Applications. *Small* **2018**, *14* (3), 1703034.
12. Onorato, J.; Pakhnyuk, V.; Luscombe, C. K., Structure and design of polymers for durable, stretchable organic electronics. *Polym. J.* **2017**, *49* (1), 41-60.
13. Li, Y.; Xu, G.; Cui, C.; Li, Y., Flexible and Semitransparent Organic Solar Cells. *Adv. Energy Mater.* **2018**, *8* (7), 1701791.
14. Koch, N., Organic electronic devices and their functional interfaces. *Chemphyschem* **2007**, *8* (10), 1438-55.
15. Coropceanu, V.; Cornil, J.; da Silva Filho, D. A.; Olivier, Y.; Silbey, R.; Brédas, J.-L., Charge Transport in Organic Semiconductors. *Chem. Rev.* **2007**, *107* (4), 926-952.
16. Cahen, D.; Kahn, A., Electron Energetics at Surfaces and Interfaces: Concepts and Experiments. *Adv. Mater.* **2003**, *15* (4), 271-277.
17. Kahn, A., Fermi level, work function and vacuum level. *Mater. Horiz.* **2016**, *3* (1), 7-10.
18. Pfeiffer, M.; Beyer, A.; Fritz, T.; Leo, K., Controlled doping of phthalocyanine layers by cosublimation with acceptor molecules: A systematic Seebeck and conductivity study. *Appl. Phys. Lett.* **1998**, *73* (22), 3202-3204.
19. Zhang, Y.; de Boer, B.; Blom, P. W. M., Controllable Molecular Doping and Charge Transport in Solution-Processed Polymer Semiconducting Layers. *Adv. Funct. Mater.* **2009**, *19* (12), 1901-1905.

20. Nevin, W. A.; Chamberlain, G. A., Photovoltaic properties of iodine-doped magnesium tetraphenylporphyrin sandwich cells. Optimization of doping, and dark electrical properties. *J. Appl. Phys.* **1990**, 68 (10), 5247-5255.
21. Walzer, K.; Maennig, B.; Pfeiffer, M.; Leo, K., Highly efficient organic devices based on electrically doped transport layers. *Chem. Rev.* **2007**, 107 (4), 1233-1271.
22. Arkhipov, V. I.; Heremans, P.; Emelianova, E. V.; Adriaenssens, G. J.; Bassler, H., Charge carrier mobility in doped semiconducting polymers. *Appl. Phys. Lett.* **2003**, 82 (19), 3245-3247.
23. Pingel, P.; Neher, D., Comprehensive picture of p-type doping of P3HT with the molecular acceptor F(4)TCNQ. *Phys. Rev. B* **2013**, 87 (11), 115209.
24. Jacobs, I. E.; Cendra, C.; Harrelson, T. F.; Bedolla Valdez, Z. I.; Faller, R.; Salleo, A.; Moulé, A. J., Polymorphism controls the degree of charge transfer in a molecularly doped semiconducting polymer. *Mater. Horiz.* **2018**, 5 (4), 655-660.
25. Salzmann, I.; Heimel, G.; Oehzelt, M.; Winkler, S.; Koch, N., Molecular Electrical Doping of Organic Semiconductors: Fundamental Mechanisms and Emerging Dopant Design Rules. *Acc. Chem. Res.* **2016**, 49 (3), 370-378.
26. Wegner, B.; Grubert, L.; Dennis, C.; Opitz, A.; Röttger, A.; Zhang, Y.; Barlow, S.; Marder, S. R.; Hecht, S.; Müllen, K.; Koch, N., Predicting the yield of ion pair formation in molecular electrical doping: redox-potentials versus ionization energy/electron affinity. *J. Mater. Chem. C* **2019**, 7 (44), 13839-13848.
27. Jakabovič, J.; Vincze, A.; Kováč, J.; Srnánek, R.; Kováč Jr, J.; Dobročka, E.; Donoval, D.; Heinemeyer, U.; Schreiber, F.; Machovič, V.; Uherek, F., Surface and interface analysis of iodine-doped pentacene structures for OTFTs. *Surf. Interface Anal.* **2011**, 43 (1-2), 518-521.
28. Varghese, A. C.; Menon, C. S., Influence of iodine on the electrical properties of magnesium phthalocyanines thin film devices. *Cent. Eur. J. Phys.* **2006**, 4 (1), 20-29.
29. Jérôme, D., Organic Conductors: From Charge Density Wave TTF-TCNQ to Superconducting (TMTSF)2PF6. *Chem. Rev.* **2004**, 104 (11), 5565-5592.

30. Torrance, J. B., The difference between metallic and insulating salts of tetracyanoquinodimethone (TCNQ): how to design an organic metal. *Acc. Chem. Res.* **1979**, *12* (3), 79-86.
31. Kanai, K.; Akaike, K.; Koyasu, K.; Sakai, K.; Nishi, T.; Kamizuru, Y.; Nishi, T.; Ouchi, Y.; Seki, K., Determination of electron affinity of electron accepting molecules. *Appl. Phys. A* **2009**, *95* (1), 309-313.
32. Gao, W. Y.; Kahn, A., Controlled p-doping of zinc phthalocyanine by coevaporation with tetrafluorotetracyanoquinodimethane: A direct and inverse photoemission study. *Appl. Phys. Lett.* **2001**, *79* (24), 4040-4042.
33. Crawford, J.; Lee, H. O.; Sun, S.-S., Optoelectronic and Electronic Properties of Tetracyanoindane for Chemical Doping of Organic Semiconductors. *MRS Advances* **2019**, *4* (31), 1811-1819.
34. Muller, L.; Rhim, S. Y.; Sivanesan, V.; Wang, D. X.; Hietzschold, S.; Reiser, P.; Mankel, E.; Beck, S.; Barlow, S.; Marder, S. R.; Pucci, A.; Kowalsky, W.; Lovrincic, R., Electric-Field-Controlled Dopant Distribution in Organic Semiconductors. *Adv. Mater.* **2017**, *29* (30), 1701466.
35. Reiser, P.; Müller, L.; Sivanesan, V.; Lovrincic, R.; Barlow, S.; Marder, S. R.; Pucci, A.; Jaegermann, W.; Mankel, E.; Beck, S., Dopant Diffusion in Sequentially Doped Poly(3-hexylthiophene) Studied by Infrared and Photoelectron Spectroscopy. *J. Phys. Chem. C* **2018**, *122* (26), 14518-14527.
36. Zhang, F. Y.; Kahn, A., Investigation of the High Electron Affinity Molecular Dopant F6-TCNNQ for Hole-Transport Materials. *Adv. Funct. Mater.* **2018**, *28* (1), 1703780.
37. Meerheim, R.; Olthof, S.; Hermenau, M.; Scholz, S.; Petrich, A.; Tessler, N.; Solomeshch, O.; Lussem, B.; Riede, M.; Leo, K., Investigation of C(60)F(36) as low-volatility p-dopant in organic optoelectronic devices. *J. Appl. Phys.* **2011**, *109* (10), 103102.
38. Li, J.; Rochester, C. W.; Jacobs, I. E.; Friedrich, S.; Stroeve, P.; Riede, M.; Moule, A. J., Measurement of Small Molecular Dopant F4TCNQ and C60F36 Diffusion in Organic Bilayer Architectures. *ACS Appl. Mater. Interfaces* **2015**, *7* (51), 28420-28428.

39. Qi, Y.; Sajoto, T.; Barlow, S.; Kim, E.-G.; Brédas, J.-L.; Marder, S. R.; Kahn, A., Use of a High Electron-Affinity Molybdenum Dithiolene Complex to p-Dope Hole-Transport Layers. *J. Am. Chem. Soc.* **2009**, *131* (35), 12530-12531.
40. Karpov, Y.; Erdmann, T.; Raguzin, I.; Al-Hussein, M.; Binner, M.; Lappan, U.; Stamm, M.; Gerasimov, K. L.; Beryozkina, T.; Bakulev, V.; Anokhin, D. V.; Ivanov, D. A.; Günther, F.; Gemming, S.; Seifert, G.; Voit, B.; Di Pietro, R.; Kiriy, A., High Conductivity in Molecularly p-Doped Diketopyrrolopyrrole-Based Polymer: The Impact of a High Dopant Strength and Good Structural Order. *Adv. Mater.* **2016**, *28* (28), 6003-10.
41. Hannah L. Smith, J. T. D., Swagat Mohapatra, Stephen Barlow, Seth R. Marder, Barry P. Rand, and Antoine Kahn, Large-gap, blue light-emitting organic homojunction diode enabled by strongly oxidizing and reducing (metal-)organic molecules. 2021.
42. Saska, J.; Gonel, G.; Bedolla-Valdez, Z. I.; Aronow, S. D.; Shevchenko, N. E.; Dudnik, A. S.; Moulé, A. J.; Mascal, M., A Freely Soluble, High Electron Affinity Molecular Dopant for Solution Processing of Organic Semiconductors. *Chem. Mater.* **2019**, *31* (5), 1500-1506.
43. Lüssem, B.; Keum, C.-M.; Kasemann, D.; Naab, B.; Bao, Z.; Leo, K., Doped Organic Transistors. *Chem. Rev.* **2016**, *116* (22), 13714-13751.
44. Yurash, B.; Cao, D. X.; Brus, V. V.; Leifert, D.; Wang, M.; Dixon, A.; Seifrid, M.; Mansour, A. E.; Lungwitz, D.; Liu, T.; Santiago, P. J.; Graham, K. R.; Koch, N.; Bazan, G. C.; Nguyen, T. Q., Towards understanding the doping mechanism of organic semiconductors by Lewis acids. *Nat. Mater.* **2019**, *18* (12), 1327-1335.
45. Shacklette, L. W.; Chance, R. R.; Ivory, D. M.; Miller, G. G.; Baughman, R. H., Electrical and optical properties of highly conducting charge-transfer complexes of poly(p-phenylene). *Synth. Met.* **1980**, *1* (3), 307-320.
46. Parthasarathy, G.; Shen, C.; Kahn, A.; Forrest, S. R., Lithium doping of semiconducting organic charge transport materials. *J. Appl. Phys.* **2001**, *89* (9), 4986-4992.
47. Choudhury, K. R.; Yoon, J.-h.; So, F., LiF as an n-Dopant in Tris(8-hydroxyquinoline) Aluminum Thin Films. *Adv. Mater.* **2008**, *20* (8), 1456-1461.
48. Haddon, R. C.; Hebard, A. F.; Rosseinsky, M. J.; Murphy, D. W.; Duclos, S. J.; Lyons, K. B.; Miller, B.; Rosamilia, J. M.; Fleming, R. M.; Kortan, A. R.; Glarum, S.

H.; Makhija, A. V.; Muller, A. J.; Eick, R. H.; Zahurak, S. M.; Tycko, R.; Dabbagh, G.; Thiel, F. A., Conducting films of C60 and C70 by alkali-metal doping. *Nature* **1991**, 350 (6316), 320-322.

49. Chan, C. K.; Amy, F.; Zhang, Q.; Barlow, S.; Marder, S.; Kahn, A., N-type doping of an electron-transport material by controlled gas-phase incorporation of cobaltocene. *Chem. Phys. Lett.* **2006**, 431 (1-3), 67-71.

50. Chan, C. K.; Zhao, W.; Barlow, S.; Marder, S.; Kahn, A., Decamethylcobaltocene as an efficient n-dopant in organic electronic materials and devices. *Org. Electron.* **2008**, 9 (5), 575-581.

51. Chan, C. K.; Kahn, A., N-doping of pentacene by decamethylcobaltocene. *Applied Physics a-Materials Science & Processing* **2009**, 95 (1), 7-13.

52. Menke, T.; Ray, D.; Meiss, J.; Leo, K.; Riede, M., In-situ conductivity and Seebeck measurements of highly efficient n-dopants in fullerene C60. *Appl. Phys. Lett.* **2012**, 100 (9), 93304.

53. Werner, A. G.; Li, F.; Harada, K.; Pfeiffer, M.; Fritz, T.; Leo, K., Pyronin B as a donor for n-type doping of organic thin films. *Appl. Phys. Lett.* **2003**, 82 (25), 4495-4497.

54. Wei, P.; Menke, T.; Naab, B. D.; Leo, K.; Riede, M.; Bao, Z., 2-(2-Methoxyphenyl)-1,3-dimethyl-1H-benzimidazol-3-ium Iodide as a New Air-Stable n-Type Dopant for Vacuum-Processed Organic Semiconductor Thin Films. *J. Am. Chem. Soc.* **2012**, 134 (9), 3999-4002.

55. Zhu, X.-Q.; Zhang, M.-T.; Yu, A.; Wang, C.-H.; Cheng, J.-P., Hydride, Hydrogen Atom, Proton, and Electron Transfer Driving Forces of Various Five-Membered Heterocyclic Organic Hydrides and Their Reaction Intermediates in Acetonitrile. *J. Am. Chem. Soc.* **2008**, 130 (8), 2501-2516.

56. Lu, M. T.; Nicolai, H. T.; Wetzelaer, G.; Blom, P. W. M., N-type doping of poly(p-phenylene vinylene) with air-stable dopants. *Appl. Phys. Lett.* **2011**, 99 (17), 173302.

57. Naab, B. D.; Himmelberger, S.; Diao, Y.; Vandewal, K.; Wei, P.; Lussem, B.; Salleo, A.; Bao, Z. N., High Mobility N-Type Transistors Based on Solution-Sheared Doped 6,13-Bis(triisopropylsilylethynyl)pentacene Thin Films. *Adv. Mater.* **2013**, 25 (33), 4663-4667.

58. Shi, K.; Zhang, F.; Di, C.-A.; Yan, T.-W.; Zou, Y.; Zhou, X.; Zhu, D.; Wang, J.-Y.; Pei, J., Toward High Performance n-Type Thermoelectric Materials by Rational Modification of BDPPV Backbones. *J. Am. Chem. Soc.* **2015**, *137* (22), 6979-6982.
59. Guo, Y. L.; Sato, W.; Inoue, K.; Zhang, W. F.; Yu, G.; Nakamura, E., n-Type doping for efficient polymeric electron-transporting layers in perovskite solar cells. *J. Mater. Chem. A* **2016**, *4* (48), 18852-18856.
60. Un, H. I.; Gregory, S. A.; Mohapatra, S. K.; Xiong, M.; Longhi, E.; Lu, Y.; Rigin, S.; Jhulki, S.; Yang, C. Y.; Timofeeva, T. V.; Wang, J. Y.; Yee, S. K.; Barlow, S.; Marder, S. R.; Pei, J., Understanding the Effects of Molecular Dopant on n-Type Organic Thermoelectric Properties. *Adv. Energy Mater.* **2019**, *9* (24).
61. Yan, X.; Xiong, M.; Li, J.-T.; Zhang, S.; Ahmad, Z.; Lu, Y.; Wang, Z.-Y.; Yao, Z.-F.; Wang, J.-Y.; Gu, X.; Lei, T., Pyrazine-Flanked Diketopyrrolopyrrole (DPP): A New Polymer Building Block for High-Performance n-Type Organic Thermoelectrics. *J. Am. Chem. Soc.* **2019**, *141* (51), 20215-20221.
62. Naab, B. D.; Guo, S.; Olthof, S.; Evans, E. G. B.; Wei, P.; Millhauser, G. L.; Kahn, A.; Barlow, S.; Marder, S. R.; Bao, Z. A., Mechanistic Study on the Solution-Phase n-Doping of 1,3-Dimethyl-2-aryl-2,3-dihydro-1H-benzoimidazole Derivatives. *J. Am. Chem. Soc.* **2013**, *135* (40), 15018-15025.
63. Jhulki, S.; Un, H. I.; Ding, Y. F.; Risko, C.; Mohapatra, S. K.; Pei, J.; Barlow, S.; Marder, S. R., Reactivity of an air-stable dihydrobenzoimidazole n-dopant with organic semiconductor molecules. *Chem* **2021**, *7* (4), 1050-1065.
64. Yang, C.-Y.; Ding, Y.-F.; Huang, D.; Wang, J.; Yao, Z.-F.; Huang, C.-X.; Lu, Y.; Un, H.-I.; Zhuang, F.-D.; Dou, J.-H.; Di, C.-a.; Zhu, D.; Wang, J.-Y.; Lei, T.; Pei, J., A thermally activated and highly miscible dopant for n-type organic thermoelectrics. *Nat. Commun* **2020**, *11* (1), 3292.
65. Guo, S.; Kim, S. B.; Mohapatra, S. K.; Qi, Y. B.; Sajoto, T.; Kahn, A.; Marder, S. R.; Barlow, S., n-Doping of Organic Electronic Materials using Air-Stable Organometallics. *Adv. Mater.* **2012**, *24* (5), 699-703.
66. Qi, Y. B.; Mohapatra, S. K.; Kim, S. B.; Barlow, S.; Marder, S. R.; Kahn, A., Solution doping of organic semiconductors using air-stable n-dopants. *Appl. Phys. Lett.* **2012**, *100* (8), 83305.

67. Naab, B. D.; Zhang, S. Y.; Vandewal, K.; Salleo, A.; Barlow, S.; Marder, S. R.; Bao, Z. A., Effective Solution- and Vacuum-Processed n-Doping by Dimers of Benzimidazoline Radicals. *Adv. Mater.* **2014**, *26* (25), 4268-4272.
68. Mohapatra, S. K.; Fonari, A.; Risko, C.; Yesudas, K.; Moudgil, K.; Delcamp, J. H.; Timofeeva, T. V.; Brédas, J. L.; Marder, S. R.; Barlow, S., Dimers of nineteen-electron sandwich compounds: crystal and electronic structures, and comparison of reducing strengths. *Chemistry* **2014**, *20* (47), 15385-94.
69. Zhang, S.; Naab, B. D.; Jucov, E. V.; Parkin, S.; Evans, E. G.; Millhauser, G. L.; Timofeeva, T. V.; Risko, C.; Brédas, J. L.; Bao, Z.; Barlow, S.; Marder, S. R., n-Dopants Based on Dimers of Benzimidazoline Radicals: Structures and Mechanism of Redox Reactions. *Chemistry* **2015**, *21* (30), 10878.
70. Kroon, R.; Ryan, J. D.; Kiefer, D.; Yu, L. Y.; Hynynen, J.; Olsson, E.; Muller, C., Bulk Doping of Millimeter-Thick Conjugated Polymer Foams for Plastic Thermoelectrics. *Adv. Funct. Mater.* **2017**, *27* (47), 1704183
71. D'Andrade, B. W.; Forrest, S. R.; Chwang, A. B., Operational stability of electrophosphorescent devices containing p and n doped transport layers. *Appl. Phys. Lett.* **2003**, *83* (19), 3858-3860.
72. Tyagi, P.; Tuli, S.; Srivastava, R., Study of fluorescence quenching due to 2, 3, 5, 6-tetrafluoro-7, 7', 8, 8'-tetracyano quinodimethane and its solid state diffusion analysis using photoluminescence spectroscopy. *J. Chem. Phys.* **2015**, *142* (5), 54707.
73. Dai, A.; Zhou, Y.; Shu, A. L.; Mohapatra, S. K.; Wang, H.; Fuentes-Hernandez, C.; Zhang, Y.; Barlow, S.; Loo, Y.-L.; Marder, S. R.; Kippelen, B.; Kahn, A., Enhanced Charge-Carrier Injection and Collection Via Lamination of Doped Polymer Layers p-Doped with a Solution-Processible Molybdenum Complex. *Adv. Funct. Mater.* **2014**, *24* (15), 2197-2204.
74. Dai, A.; Wan, A.; Magee, C.; Zhang, Y. D.; Barlow, S.; Marder, S. R.; Kahn, A., Investigation of p-dopant diffusion in polymer films and bulk heterojunctions: Stable spatially-confined doping for all-solution processed solar cells. *Org. Electron.* **2015**, *23*, 151-157.
75. Lin, X.; Wegner, B.; Lee, K. M.; Fusella, M. A.; Zhang, F.; Moudgil, K.; Rand, B. P.; Barlow, S.; Marder, S. R.; Koch, N.; Kahn, A., Beating the thermodynamic limit with photo-activation of n-doping in organic semiconductors. *Nat. Mater.* **2017**, *16* (12), 1209-1215.

76. Mor, G. K.; Jones, D.; Le, T. P.; Shang, Z. R.; Weathers, P. J.; Woltermann, M. K. B.; Vakhshouri, K.; Williams, B. P.; Tohran, S. A.; Saito, T.; Verduzco, R.; Salleo, A.; Hickner, M. A.; Gomez, E. D., Contact Doping with Sub-Monolayers of Strong Polyelectrolytes for Organic Photovoltaics. *Adv. Energy Mater.* **2014**, *4* (13), 1400439.
77. Kim, Y.; Broch, K.; Lee, W.; Ahn, H.; Lee, J.; Yoo, D.; Kim, J.; Chung, S.; Sirringhaus, H.; Kang, K.; Lee, T., Highly Stable Contact Doping in Organic Field Effect Transistors by Dopant-Blockade Method. *Adv. Funct. Mater.* **2020**, *30* (28), 2000058.
78. Li, J.; Rochester, C. W.; Jacobs, I. E.; Aasen, E. W.; Friedrich, S.; Stroeve, P.; Moule, A. J., The effect of thermal annealing on dopant site choice in conjugated polymers. *Org. Electron.* **2016**, *33*, 23-31.
79. Aizawa, N.; Pu, Y. J.; Chiba, T.; Kawata, S.; Sasabe, H.; Kido, J., Instant Low-Temperature Cross-Linking of Poly(N-vinylcarbazole) for Solution-Processed Multilayer Blue Phosphorescent Organic Light-Emitting Devices. *Adv. Mater.* **2014**, *26* (45), 7543-7546.
80. Aizawa, N.; Fuentes-Hernandez, C.; Kolesov, V. A.; Khan, T. M.; Kido, J.; Kippelen, B., Simultaneous cross-linking and p-doping of a polymeric semiconductor film by immersion into a phosphomolybdic acid solution for use in organic solar cells. *Chem. Commun.* **2016**, *52* (19), 3825-3827.
81. Kolesov, V. A.; Fuentes-Hernandez, C.; Chou, W.-F.; Aizawa, N.; Larrain, F. A.; Wang, M.; Perrotta, A.; Choi, S.; Graham, S.; Bazan, G. C.; Nguyen, T.-Q.; Marder, S. R.; Kippelen, B., Solution-based electrical doping of semiconducting polymer films over a limited depth. *Nat. Mater.* **2017**, *16* (4), 474-480.
82. Reiser, P.; Benneckendorf, F. S.; Barf, M. M.; Muller, L.; Bauerle, R.; Hillebrandt, S.; Beck, S.; Lovrincic, R.; Mankel, E.; Freudenberg, J.; Jansch, D.; Kowalsky, W.; Pucci, A.; Jaegermann, W.; Bunz, U. H. F.; Mullen, K., n-Type Doping of Organic Semiconductors: Immobilization via Covalent Anchoring. *Chem. Mater.* **2019**, *31* (11), 4213-4221.
83. Bräse, S.; Gil, C.; Knepper, K.; Zimmermann, V., Organic azides: an exploding diversity of a unique class of compounds. *Angew. Chem. Int. Ed. Engl.* **2005**, *44* (33), 5188-240.
84. Schlitz, R. A.; Brunetti, F. G.; Glaudell, A. M.; Miller, P. L.; Brady, M. A.; Takacs, C. J.; Hawker, C. J.; Chabynyc, M. L., Solubility-Limited Extrinsic n-Type Doping

of a High Electron Mobility Polymer for Thermoelectric Applications. *Adv. Mater.* **2014**, *26* (18), 2825-2830.

85. Lu, Y.; Yu, Z.-D.; Zhang, R.-Z.; Yao, Z.-F.; You, H.-Y.; Jiang, L.; Un, H.-I.; Dong, B.-W.; Xiong, M.; Wang, J.-Y.; Pei, J., Rigid Coplanar Polymers for Stable n-Type Polymer Thermoelectrics. *Angew. Chem. Int. Ed.* **2019**, *58* (33), 11390-11394.

86. Bin, Z.; Li, J.; Wang, L.; Duan, L., Efficient n-type dopants with extremely low doping ratios for high performance inverted perovskite solar cells. *Energy Environ. Sci.* **2016**, *9* (11), 3424-3428.

87. Riera-Galindo, S.; Orbelli Biroli, A.; Forni, A.; Puttisong, Y.; Tessore, F.; Pizzotti, M.; Pavlopoulou, E.; Solano, E.; Wang, S.; Wang, G.; Ruoko, T.-P.; Chen, W. M.; Kemerink, M.; Berggren, M.; di Carlo, G.; Fabiano, S., Impact of Singly Occupied Molecular Orbital Energy on the n-Doping Efficiency of Benzimidazole Derivatives. *ACS Appl. Mater. Interfaces* **2019**, *11* (41), 37981-37990.

88. Uebe, M.; Yoshihashi, Y.; Noda, K.; Matsubara, M.; Ito, A., A dendritic oligoarylamine-substituted benzimidazole derivative as a useful n-type dopant. *J. Mater. Chem. C.* **2018**, *6* (24), 6429-6439.

89. Shin, Y.; Massetti, M.; Komber, H.; Biskup, T.; Nava, D.; Lanzani, G.; Caironi, M.; Sommer, M., Improving Miscibility of a Naphthalene Diimide-Bithiophene Copolymer with n-Type Dopants through the Incorporation of “Kinked” Monomers. *Adv. Electron. Mater.* **2018**, *4* (10), 1700581.

90. Qiu, L.; Liu, J.; Alessandri, R.; Qiu, X.; Koopmans, M.; Havenith, Remco W. A.; Marrink, S. J.; Chiechi, R. C.; Anton Koster, L. J.; Hummelen, J. C., Enhancing doping efficiency by improving host-dopant miscibility for fullerene-based n-type thermoelectrics. *J. Mater. Chem. A.* **2017**, *5* (40), 21234-21241.

91. Lu, Q.; Ma, Y.; Li, H.; Guan, X.; Yusran, Y.; Xue, M.; Fang, Q.; Yan, Y.; Qiu, S.; Valtchev, V., Postsynthetic Functionalization of Three-Dimensional Covalent Organic Frameworks for Selective Extraction of Lanthanide Ions. *Angew. Chem. Int. Ed.* **2018**, *57* (21), 6042-6048.

92. Kim, S. S.; Bae, S.; Jo, W. H., Performance enhancement of planar heterojunction perovskite solar cells by n-doping of the electron transporting layer. *Chem. Commun.* **2015**, *51* (98), 17413-17416.

93. Yan, H.; Chen, Z. H.; Zheng, Y.; Newman, C.; Quinn, J. R.; Dotz, F.; Kastler, M.; Facchetti, A., A high-mobility electron-transporting polymer for printed transistors. *Nature* **2009**, *457* (7230), 679-686.
94. Lu, Y.; Yu, Z. D.; Un, H. I.; Yao, Z. F.; You, H. Y.; Jin, W. L.; Li, L.; Wang, Z. Y.; Dong, B. W.; Barlow, S.; Longhi, E.; Di, C. A.; Zhu, D. B.; Wang, J. Y.; Silva, C.; Marder, S. R.; Pei, J., Persistent Conjugated Backbone and Disordered Lamellar Packing Impart Polymers with Efficient n-Doping and High Conductivities. *Adv. Mater.* **2021**, *33* (2), 2005946.
95. Heimel, G., The Optical Signature of Charges in Conjugated Polymers. *ACS Cent. Sci.* **2016**, *2* (5), 309-315.
96. Guo, X.; Watson, M. D., Conjugated Polymers from Naphthalene Bisimide. *Org. Lett.* **2008**, *10* (23), 5333-5336.
97. Wei, P.; Oh, J. H.; Dong, G. F.; Bao, Z. N., Use of a 1H-Benzoimidazole Derivative as an n-Type Dopant and To Enable Air-Stable Solution-Processed n-Channel Organic Thin-Film Transistors. *J. Am. Chem. Soc.* **2010**, *132* (26), 8852-8853.
98. Duong, D. T.; Wang, C. C.; Antono, E.; Toney, M. F.; Salleo, A., The chemical and structural origin of efficient p-type doping in P3HT. *Org. Electron.* **2013**, *14* (5), 1330-1336.
99. Wu, Y.; Schneider, S.; Walter, C.; Chowdhury, A. H.; Bahrami, B.; Wu, H.-C.; Qiao, Q.; Toney, M. F.; Bao, Z., Fine-Tuning Semiconducting Polymer Self-Aggregation and Crystallinity Enables Optimal Morphology and High-Performance Printed All-Polymer Solar Cells. *J. Am. Chem. Soc.* **2020**, *142* (1), 392-406.
100. Zhu, L.; Sheng, D.; Xu, C.; Dai, X.; Silver, M. A.; Li, J.; Li, P.; Wang, Y.; Wang, Y.; Chen, L.; Xiao, C.; Chen, J.; Zhou, R.; Zhang, C.; Farha, O. K.; Chai, Z.; Albrecht-Schmitt, T. E.; Wang, S., Identifying the Recognition Site for Selective Trapping of $^{99}\text{TcO}_4^-$ in a Hydrolytically Stable and Radiation Resistant Cationic Metal–Organic Framework. *J. Am. Chem. Soc.* **2017**, *139* (42), 14873-14876.
101. Kungurtsev, V.; Laakkonen, J.; Molina, A. G.; Virta, P., Solution-Phase Synthesis of Short Oligo-2'-deoxyribonucleotides by Using Clustered Nucleosides as a Soluble Support. *Eur. J. Org. Chem.* **2013**, *2013* (29), 6687-6693.

102. Kahle, F.-J.; Saller, C.; Köhler, A.; Strohrriegl, P., Crosslinked Semiconductor Polymers for Photovoltaic Applications. *Adv. Energy Mater.* **2017**, 7 (16), 1700306.
103. Shieh, Y.-T.; Hsiao, K.-I., Thermal properties of silane-grafted water-crosslinked polyethylene. *J. Appl. Polym. Sci.* **1998**, 70 (6), 1075-1082.
104. Bacher, A.; Erdelen, C. H.; Paulus, W.; Ringsdorf, H.; Schmidt, H.-W.; Schuhmacher, P., Photo-Cross-Linked Triphenylenes as Novel Insoluble Hole Transport Materials in Organic LEDs. *Macromolecules* **1999**, 32 (14), 4551-4557.
105. Cava, M. P.; Deana, A. A.; Muth, K., Condensed Cyclobutane Aromatic Compounds. VIII. The Mechanism of Formation of 1,2-Dibromobenzocyclobutene; A New Diels-Alder Synthesis. *J. Am. Chem. Soc.* **1959**, 81 (24), 6458-6460.
106. Marks, M. J.; Erskine, J. S.; McCrery, D. A., Products and Mechanism of the Thermal Crosslinking of Benzocyclobutene-Terminated Bisphenol A Polycarbonates. *Macromolecules* **1994**, 27 (15), 4114-4126.
107. Walker, K. A.; Markoski, L. J.; Deeter, G. A.; Spilman, G. E.; Martin, D. C.; Moore, J. S., Crosslinking chemistry for high-performance polymer networks. *Polymer* **1994**, 35 (23), 5012-5017.
108. Thummel, R. P., Benzocyclobutene and related compounds. *Acc. Chem. Res.* **1980**, 13 (3), 70-76.
109. Farona, M. F., Benzocyclobutenes in polymer chemistry. *Prog. Polym. Sci.* **1996**, 21 (3), 505-555.
110. Burdeaux, D.; Townsend, P.; Carr, J.; Garrou, P., Benzocyclobutene (BCB) dielectrics for the fabrication of high density, thin film multichip modules. *J. Electron. Mater.* **1990**, 19 (12), 1357-1366.
111. Pugh, C.; Baker, J. S.; Storms, W. K., Synthesis of a Polymerizable Benzocyclobutene that Undergoes Ring-Opening Isomerization at Reduced Temperature. *Synlett* **2014**, 25 (1), 148-152.
112. Zardetto, V.; Brown, T. M.; Reale, A.; Di Carlo, A., Substrates for flexible electronics: A practical investigation on the electrical, film flexibility, optical, temperature,

and solvent resistance properties. *J. Polym. Sci., Part B: Polym. Phys.* **2011**, *49* (9), 638-648.

113. Hayes, C. O.; Chen, P. H.; Thedford, R. P.; Ellison, C. J.; Dong, G. B.; Willson, C. G., Effect of Ring Functionalization on the Reaction Temperature of Benzocyclobutene Thermoset Polymers. *Macromolecules* **2016**, *49* (10), 3706-3715.

114. Dobish, J. N.; Hamilton, S. K.; Harth, E., Synthesis of low-temperature benzocyclobutene cross-linker and utilization. *Polym. Chem.* **2012**, *3* (4), 857-860.

115. Bubb, W.; Sternhell, S., Proton N.M.R. spectra of 1-substituted benzocyclobutenes (Bicyclo[4,2,0]octa-1,3,5-trienes). *Aust. J. Chem.* **1976**, *29* (8), 1685-1697.

116. Ghosh, R.; Kushwaha, A.; Das, D., Conformational Control of Ultrafast Molecular Rotor Property: Tuning Viscosity Sensing Efficiency by Twist Angle Variation. *J. Phys. Chem. B.* **2017**, *121* (37), 8786-8794.

117. Gies, A. P.; Spencer, L.; Rau, N. J.; Boopalachandran, P.; Rickard, M. A.; Kearns, K. L.; McDougal, N. T., Thermally Induced Cross-Linking and Degradation Reactions of Benzocyclobutene-Based Polymers. *Macromolecules* **2017**, *50* (6), 2304-2319.

118. Hallani, R. K.; Moser, M.; Bristow, H.; Jenart, M. V. C.; Faber, H.; Neophytou, M.; Yarali, E.; Paterson, A. F.; Anthopoulos, T. D.; McCulloch, I., Low-Temperature Cross-Linking Benzocyclobutene Based Polymer Dielectric for Organic Thin Film Transistors on Plastic Substrates. *J. Org. Chem.* **2020**, *85* (1), 277-283.

119. Deb, N.; Dasari, R. R.; Moudgil, K.; Hernandez, J. L.; Marder, S. R.; Sun, Y.; Karim, A.; Bucknall, D. G., Thermo-cross-linkable fullerene for long-term stability of photovoltaic devices. *J. Mater. Chem. A.* **2015**, *3* (43), 21856-21863.

120. Fukuzumi, S.; Mori, H.; Suenobu, T.; Imahori, H.; Gao, X.; Kadish, K. M., Effects of Lowering Symmetry on the ESR Spectra of Radical Anions of Fullerene Derivatives and the Reduction Potentials. *J. Phys. Chem. A.* **2000**, *104* (46), 10688-10694.

121. Malinauskas, T.; Tomkute-Luksiene, D.; Sens, R.; Daskeviciene, M.; Send, R.; Wonneberger, H.; Jankauskas, V.; Bruder, I.; Getautis, V., Enhancing Thermal Stability and Lifetime of Solid-State Dye-Sensitized Solar Cells via Molecular Engineering of the Hole-Transporting Material Spiro-OMeTAD. *ACS Appl. Mater. Interfaces* **2015**, *7* (21), 11107-11116.

122. Liu, J.; Qiu, L.; Portale, G.; Koopmans, M.; ten Brink, G.; Hummelen, J. C.; Koster, L. J. A., N-Type Organic Thermoelectrics: Improved Power Factor by Tailoring Host–Dopant Miscibility. *Adv. Mater.* **2017**, *29* (36), 1701641.
123. Liu, J.; Qiu, L.; Alessandri, R.; Qiu, X.; Portale, G.; Dong, J.; Talsma, W.; Ye, G.; Sengrian, A. A.; Souza, P. C. T.; Loi, M. A.; Chiechi, R. C.; Marrink, S. J.; Hummelen, J. C.; Koster, L. J. A., Enhancing Molecular n-Type Doping of Donor–Acceptor Copolymers by Tailoring Side Chains. *Adv. Mater.* **2018**, *30* (7), 1704630.
124. Saglio, B.; Mura, M.; Massetti, M.; Scuratti, F.; Beretta, D.; Jiao, X.; McNeill, C. R.; Sommer, M.; Famulari, A.; Lanzani, G.; Caironi, M.; Bertarelli, C., N-Alkyl substituted 1H-benzimidazoles as improved n-type dopants for a naphthalene-diimide based copolymer. *J. Mater. Chem. A* **2018**, *6* (31), 15294-15302.
125. Liu, J.; Maity, S.; Roosloot, N.; Qiu, X. K.; Qiu, L.; Chiechi, R. C.; Hummelen, J. C.; von Hauff, E.; Koster, L. J. A., The Effect of Electrostatic Interaction on n-Type Doping Efficiency of Fullerene Derivatives. *Adv. Electron. Mater.* **2019**, *5* (11), 1800959-1800967.
126. Sami, S.; Alessandri, R.; Broer, R.; Havenith, R. W. A., How Ethylene Glycol Chains Enhance the Dielectric Constant of Organic Semiconductors: Molecular Origin and Frequency Dependence. *ACS Appl. Mater. Interfaces* **2020**, *12* (15), 17783-17789.
127. Liu, C.-L.; Chen, Y.; Shelar, D. P.; Li, C.; Cheng, G.; Fu, W.-F., Bodipy dyes bearing oligo(ethylene glycol) groups on the meso-phenyl ring: tuneable solid-state photoluminescence and highly efficient OLEDs. *J. Mater. Chem. C* **2014**, *2* (28), 5471-5478.
128. Seidel, K. F.; Lungwitz, D.; Opitz, A.; Krüger, T.; Behrends, J.; Marder, S. R.; Koch, N., Single-Step Formation of a Low Work Function Cathode Interlayer and n-type Bulk Doping from Semiconducting Polymer/Polyethylenimine Blend Solution. *ACS Applied Materials & Interfaces* **2020**, *12* (25), 28801-28807.
129. Hughes, M. P.; Rosenthal, K. D.; Ran, N. A.; Seifrid, M.; Bazan, G. C.; Nguyen, T.-Q., Determining the Dielectric Constants of Organic Photovoltaic Materials Using Impedance Spectroscopy. *Adv. Funct. Mater.* **2018**, *28* (32), 1801542-1801549.
130. Menke, T.; Ray, D.; Kleemann, H.; Leo, K.; Riede, M., Determining doping efficiency and mobility from conductivity and Seebeck data of n-doped C60 layers. *physica status solidi (b)* **2015**, *252* (8), 1877-1883.

131. Liu, J.; Qiu, L.; Portale, G.; Torabi, S.; Stuart, M. C. A.; Qiu, X. K.; Koopmans, M.; Chiechi, R. C.; Hummelen, J. C.; Koster, L. J. A., Side-chain effects on N-type organic thermoelectrics: A case study of fullerene derivatives. *Nano Energy* **2018**, *52*, 183-191.
132. Higgins, A.; Mohapatra, S. K.; Barlow, S.; Marder, S. R.; Kahn, A., Dopant controlled trap-filling and conductivity enhancement in an electron-transport polymer. *Appl. Phys. Lett.* **2015**, *106* (16), 163301-163304.
133. Olthof, S.; Mehraeen, S.; Mohapatra, S. K.; Barlow, S.; Coropceanu, V.; Bredas, J. L.; Marder, S. R.; Kahn, A., Ultralow Doping in Organic Semiconductors: Evidence of Trap Filling. *Phys. Rev. Lett.* **2012**, *109* (17), 176601-176603.
134. Kluge, R. M.; Saxena, N.; Chen, W.; Körstgens, V.; Schwartzkopf, M.; Zhong, Q.; Roth, S. V.; Müller-Buschbaum, P., Doping Dependent In-Plane and Cross-Plane Thermoelectric Performance of Thin n-Type Polymer P(NDI2OD-T2) Films. *Adv. Funct. Mater.* **2020**, *30* (28), 2003092.
135. Zhang, Y.-D.; Hreha, R. D.; Jabbour, G. E.; Kippelen, B.; Peyghambarian, N.; Marder, S. R., Photo-crosslinkable polymers as hole-transport materials for organic light-emitting diodes. *J. Mater. Chem.* **2002**, *12* (6), 1703-1708.
136. Tremblay, M.-H.; Schutt, K.; Pulvirenti, F.; Schultz, T.; Wegner, B.; Jia, X.; Zhang, Y.; Longhi, E.; Dasari, R. R.; Fuentes-Hernandez, C.; Kippelen, B.; Koch, N.; Snaith, H. J.; Barlow, S.; Marder, S. R., Benzocyclobutene polymer as an additive for a benzocyclobutene-fullerene: application in stable p-i-n perovskite solar cells. *J. Mater. Chem. A* **2021**, *9* (14), 9347-9353.
137. Tremblay, M.-H.; Schutt, K.; Zhang, Y.; Lim, J.; Lin, Y.-H.; Warby, J. H.; Barlow, S.; Snaith, H. J.; Marder, S. R., A photo-crosslinkable bis-triarylamine side-chain polymer as a hole-transport material for stable perovskite solar cells. *Sustain. Energy Fuels* **2020**, *4* (1), 190-198.